

NOTE TO USERS

This reproduction is the best copy available.

UMI

A Transient Numerical Algorithm to Predict Temperature and Liquid Content of Carryover in Kraft Recovery Boilers

By

Shermineh Vafa

**A thesis submitted in conformity with the requirements
for the degree of Master of Applied Science
Graduate Department of Chemical Engineering and Applied Chemistry
University of Toronto**

© Copyright by Shermineh Vafa 2001



**National Library
of Canada**

**Acquisitions and
Bibliographic Services**

**395 Wellington Street
Ottawa ON K1A 0N4
Canada**

**Bibliothèque nationale
du Canada**

**Acquisitions et
services bibliographiques**

**395, rue Wellington
Ottawa ON K1A 0N4
Canada**

Your file Votre référence

Our file Notre référence

The author has granted a non-exclusive licence allowing the National Library of Canada to reproduce, loan, distribute or sell copies of this thesis in microform, paper or electronic formats.

The author retains ownership of the copyright in this thesis. Neither the thesis nor substantial extracts from it may be printed or otherwise reproduced without the author's permission.

L'auteur a accordé une licence non exclusive permettant à la Bibliothèque nationale du Canada de reproduire, prêter, distribuer ou vendre des copies de cette thèse sous la forme de microfiche/film, de reproduction sur papier ou sur format électronique.

L'auteur conserve la propriété du droit d'auteur qui protège cette thèse. Ni la thèse ni des extraits substantiels de celle-ci ne doivent être imprimés ou autrement reproduits sans son autorisation.

0-612-62927-9

Canada

Master of Applied Science 2001

Shermineh Vafa

Graduate Department of Chemical Engineering and Applied Chemistry

University of Toronto

Abstract

Deposition of carryover, the molten or partially molten smelt particles, in kraft recovery boilers is primarily a function of velocity, temperature, and liquid content of the carryover upon impact on heat transfer surfaces. In this study, an algorithm to track the velocity, temperature, and liquid content of carryover was developed and integrated within a commercially available computational fluid dynamics (CFD) package. The algorithm was used to track Na_2SO_4 - NaCl - K_2SO_4 containing particles numerically seeded within CFD simulations of the gas flow through an EFR and a simplified model of the upper furnace of a kraft recovery boiler. The predicted particle velocity, temperature, and liquid content results agreed well with the EFR impact and deposition experimental data. The upper furnace particle temperature and liquid content results predict, under the simplified conditions considered, that deposits will form primary on the first and second platens of a clean boiler while in a fouled boiler deposits stop growing on the first platen but continue to grow on the second platen. In both boiler cases, smaller particles deposit uniformly across the height of the tubes in superheater section while larger particles preferentially deposit on the upper part of the tubes and the top wall. These results are in agreement with literature and other numerical studies.

To my dear parents

Acknowledgments

My very special thanks are due to Professors David C.S. Kuhn and Honghi Tran for their excellent supervision, professional guidance, and encouragement during this work.

I would like to thank Mojghan Naseri for all her support, help, and wise comments, but mostly I am thankful to her for being a great friend. Many thanks are due to all my friends for making these two years memorable.

I am very thankful to the faculty and staff of the Pulp & Paper Centre for providing a fantastic and simulating environment.

I am grateful to the members of the research consortium on Improving Recovery Boiler Performance, Emissions and Safety, and NSERC for their financial support of this project.

A million thanks to my parents and my brother for their unconditional love, encouragement, and unfailing support.

Table of Contents

Abstract	ii
Acknowledgments	iii
Table of Contents	iv
List of Figures	vi
Nomenclature	ix
1. Introduction	1
2. Literature Review	5
2.1 Fireside Deposits	5
2.1.1 Thermal and Radiative Properties of Fireside Deposits	9
2.1.2 The Effect of Chloride and Potassium on Deposit Stickiness	11
2.1.3 The Role of Particle Liquid Content in Carryover Deposition	14
2.1.4 Particle Transport Mechanisms	15
2.1.5 Curvilinear Motion of Particles	17
2.2 Plugging in Kraft Recovery Boiler	18
2.3 Numerical Modeling of Dilute Gas-Particle Flows	20
2.3.1 Particle Velocity in Dilute Two-Phase Flow Systems	21
2.3.2 Turbulent Dispersion of Particles	23
2.3.3 Particle Temperature Estimation	24
2.4 Numerical Modeling of kraft Recovery Boiler	26
2.5 Summary	27
3. The Entrained Flow Reactor	28
3.1 Entrained Flow Reactor Components	28
3.2 Entrained Flow Reactor Operating Conditions	30
3.3 Pressure Measurement	31

4.	Numerical Method	34
4.1	The Finite Volume Method	35
4.1.1	Discretization of Governing Equations	36
4.1.2	Iterative Solution and the SIMPLE Algorithm	39
4.2	Particle Velocity and Temperature Estimation	42
4.2.1	Velocity Estimation and Turbulent Dispersion of the Particles	42
4.2.2	Particle Temperature and Liquid Content Estimation	45
4.3	Numerical Model of the Entrained Flow Reactor	49
4.3.1	EFR Geometric Model and Boundary Conditions	50
4.3.2	Particle Velocity and Temperature Estimations in the EFR	54
4.4	Numerical Model of a Simplified Upper Furnace	54
4.4.1	Flue Gas Velocity and Temperature Fields Simulation	54
4.4.2	Particle Trajectory and Temperature Estimations in the Upper Furnace	59
5.	Results and Discussion	60
5.1	Validation of the Entrained Flow Reactor Model	60
5.1.1	Sensitivity of the Results to Numerical Parameters	60
5.1.2	Flue Gas Velocity and Temperature	62
5.1.3	Particle Impact Velocity	68
5.1.4	Particle Temperature and Liquid Content	71
5.1.5	Summary	80
5.2	Validation of the Recovery Boiler Upper Furnace Model	81
5.2.1	Sensitivity of the Results to Numerical Parameters	81
5.2.2	Flue Gas Velocity and Temperature	82
5.2.3	Particle Temperature and Liquid Content	85
5.2.4	Summary	96
6.	Implications	98
7.	Conclusions	100
8.	Recommendations	103
	References	104
	Appendix	111

List of Figures

- Figure 1.1 Schematic diagram of a kraft recovery boiler
- Figure 2.1 Composition of oxidized smelt (a) and carryover deposition (b)
- Figure 2.2 Fume composition in lower furnace and (a) upper furnace (b)
- Figure 2.3 Absorption and scattering efficiencies of recovery boiler ash
- Figure 2.4 Emissivity for black liquor, dried solids, char, molten smelt and fume
- Figure 2.5 Effect of chloride on the sticky temperature zone
- Figure 2.6 Effect of chloride and potassium on sticky temperature
- Figure 2.7 Phase diagram of the system $\text{Na}_2\text{SO}_4\text{-NaCl}$
- Figure 2.8 Particle trajectories around a circular cylinder
- Figure 2.9 Deposit accumulation pattern in superheater region
- Figure 3.1 Schematic diagram of the EFR, internal diameter 18.1 *cm*, heated section height 6 *m*
- Figure 3.2 Schematic diagram of the calibration setup
- Figure 3.3 Schematic diagram of the experimental setup
- Figure 3.4 Measured static pressures at the inlet of the fan in the exhaust section
- Figure 4.1 A typical CV for a Cartesian 2D and 3D grid
- Figure 4.2 SIMPLE algorithm
- Figure 4.3 Uncoupled discrete phase calculation
- Figure 4.4 Computational grid shown on the surface of the EFR geometry in non-heated section of the EFR
- Figure 4.5 CFD boundary conditions of the EFR model
- Figure 4.6 (a) The recovery boiler geometry, (b) Computational grid generated for the boiler geometry

- Figure 4.7** CFD velocity boundary conditions for the boiler model
- Figure 5.1** Comparison of the influence of mesh density on gas velocity along the centre of the EFR, MS1-309,000, MS2-390,000, and MS3-600,000 cells
- Figure 5.2** Entrained air and gas velocity vectors (m/s) in the non-heated section
- Figure 5.3** Gas velocity vectors (m/s) over the probe
- Figure 5.4** Predicted and measured velocity profiles 2 cm above the probe
- Figure 5.5** Gas temperature contours in the non-heated section without considering radiation
- Figure 5.6** Gas temperature contours in the non-heated section considering a P-1 radiation model
- Figure 5.7** Predicted (P-1 model) and experimented gas temperature profiles at the exit of the reactor
- Figure 5.8** Predicted particle impact velocity on EFR probe versus experimental data, 10 mole% Cl/(Na+K) and 0 mole% K/(Na+K), shape factor=1.0
- Figure 5.9** Predicted particle impact velocity on EFR probe versus experimental data, 2 mole% Cl/(Na+K) and 0 mole% K/(Na+K), shape factor=0.8
- Figure 5.10** Estimated temperature for particles containing 10 mole% Cl/(Na+K) and 0 mole% K/(Na+K)
- Figure 5.11** Estimated liquid content for particles containing 10 mole% Cl/(Na+K) and 0 mole% K/(Na+K)
- Figure 5.12** Estimated particle temperature using the lever rule and thermodynamic data, 10 mole% Cl/(Na+K) and 0 mole% K/(Na+K), 430 μm particle size
- Figure 5.13** Estimated temperature for particles containing different chloride contents, 260 μm particle size
- Figure 5.14** Estimated liquid content for particles containing different chloride contents, 260 μm particle size
- Figure 5.15** Estimated temperature for particles containing different chloride contents, 590 μm particle size
- Figure 5.16** Estimated liquid content for particles containing different chloride contents, 590 μm particle size
- Figure 5.17** Estimated temperature for particles containing 10 mole% Cl/(Na+K) and 5 mole% K/(Na+K)

- Figure 5.18 Estimated liquid content for particles containing 10 mole% Cl/(Na+K) and 5 mole% K/(Na+K)
- Figure 5.19 Influence of the mesh density on the gas velocity at the centre of the upper furnace MS1-71,517, MS2-98,311, and MS3-114,334
- Figure 5.20 Gas velocity vectors on the central vertical plane (m/s)
- Figure 5.21 Gas temperature contours on the central plane (°C)
- Figure 5.22 Particle trajectories in the upper furnace
- Figure 5.23 Particle trajectories for different sizes of 150 and 590 μm
- Figure 5.24 Distribution of 150, 300, and 590 μm particles on the first platen
- Figure 5.25 Particle temperature at the first platen, clean boiler case 10 mole% Cl/(Na+K) and 0 mole% K/(Na+K) and 150 μm particle size
- Figure 5.26 Particle temperature at the first platen, clean boiler case 10 mole% Cl/(Na+K) and 0 mole% K/(Na+K) and 300 μm particle size
- Figure 5.27 Particle temperature at the first platen, clean boiler case 10 mole% Cl/(Na+K) and 0 mole% K/(Na+K) and 590 μm particle size
- Figure 5.28 Particle liquid content at the first platen, clean boiler case 10 mole% Cl/(Na+K) and 0 mole% K/(Na+K) and 150 μm particle size
- Figure 5.29 Particle liquid content at the first platen, clean boiler case 10 mole% Cl/(Na+K) and 0 mole% K/(Na+K) and 300 μm particle size
- Figure 5.30 Particle liquid content at the first platen, clean boiler case 10 mole% Cl/(Na+K) and 0 mole% K/(Na+K) and 590 μm particle size
- Figure 5.31 Particle temperature at the second platen, clean boiler case 10 mole% Cl/(Na+K) and 0 mole% K/(Na+K) and 150 μm particle size
- Figure 5.32 Particle temperature at the second platen, clean boiler case 10 mole% Cl/(Na+K) and 0 mole% K/(Na+K) and 300 μm particle size
- Figure 5.33 Particle temperature at the second platen, clean boiler case 10 mole% Cl/(Na+K) and 0 mole% K/(Na+K) and 590 μm particle size
- Figure 5.34 Gas temperature contours on central plane in a fouled boiler case (°C)
- Figure 5.35 Particle temperature at the first platen, fouled boiler case 10 mole% Cl/(Na+K) and 0 mole% K/(Na+K) and 150 μm particle size
- Figure 5.36 Particle temperature at the first platen, fouled boiler case 10 mole% Cl/(Na+K) and 0 mole% K/(Na+K) and 300 μm particle size

Nomenclature

A_p	Particle Surface Area (m^2)
Bi	Biot Number ($=\frac{hL_c}{k_p}$)
C_D	Coefficient of Drag
c_p	Specific Heat ($J/kg.K$)
D_p	Particle Diameter (m)
D_t	Tube Diameter (m)
F_x	Forces Acting on a Particle (N)
g	Gravitational Acceleration (m/s^2)
h	Convective Heat Transfer Coefficient ($W/m^2.K$)
I	Radiation Intensity (W/m^2)
k_D	Deposit Thermal Conductivity ($W/m^2.K$)
k_g	Gas Thermal Conductivity ($W/m^2.K$)
k_p	Particle Thermal Conductivity ($W/m K$)
L	Particle Liquid Content
L_c	Particle Characteristic Length (m)
L_{FM}	Particle Liquid Content at the First Melting Temperature
L_s	Length Scale (m)
M_{NaCl}	Mole% $NaCl/(NaCl+Na_2SO_4)$.
m_p	Particle mass (kg)
Nu	Nusselt Number ($=hD_p/k_g$)

p'_p	Pressure Correction (Pa)
p_p°	Guessed Pressure (Pa)
Pr	Prandtl Number
q_\bullet	Source Term
Q_p	Particle Enthalpy per Mass (J/kg)
Re_p	Particle Reynolds Number ($\frac{\rho_g D_p U_p}{\mu_g}$)
S_f	CV Face Area (m ²)
Stk	Stokes Number ($= \frac{\rho_p D_p^2 U}{9\mu_g D_i}$)
Stk_{eff}	Effective Stokes Number (=Stk * ψ)
T_{CM}	Complete Melting Temperature (°C)
T_{FM}	First Melting Temperature (°C)
T_g	Gas Temperature (°C)
T_p	Particle Temperatures (°C)
$u_{i,p}^\circ$	Calculated Velocity (m/s)
u'	Fluctuating Velocities (m/s)
U	Free Gas Velocity (m/s)
\bar{U}	Mean Velocity (m/s)
U_p	Particle Velocity (m/s)
V_p	Particle Volume (m ³)
V_{ST}	Particle Terminal Velocity (m/s)

Greek Symbols

Γ	Diffusion Coefficient
Δt	Time Increment
ϵ	Particle Emissivity
θ_r	Radiation Temperature $(= (I/4\sigma)^{1/4})$
λ	Latent Heat of Fusion (J/Kg)
μ_g	Gas Viscosity (Ns/m ²)
ρ_g	Gas Density (Kg/m ³)
ρ_p	Particle Density (Kg/m ³)
σ	Stefan-Boltzman Constant
ϕ	Dependent Variable in General Descretized Equation
Φ	Particle Shape Factor
ψ	Non-Stokesian Drag Correction Factor
Ω	CV Volume (m ³)

1. Introduction

Kraft recovery boilers are used in pulp and paper mills to burn black liquor, a by-product of chemical pulping, to recycle the pulping chemicals and to generate power [18]. A schematic diagram of a kraft recovery boiler is shown in Figure 1.1. The accumulation of fireside deposits on heat transfer surfaces may cause problems such as plugging of flue gas passages and decreasing the boiler heat transfer performances. It is important to have a fundamental understanding of the particle deposition mechanism due to importance to the operation of a recovery boiler [18,47,45].

Deposits in the upper furnace are formed by three types of particles: fume, intermediate size particles, and carryover. Fume is sub-micron sized solid particle which is generated as a result of condensation of alkali vapors in the flue gas. Fume particles form deposits mainly in the generating bank and the economizer [47,44]. Intermediate-sized particles are in the size range of 1-100 μm and they are formed as a result of physical ejection of materials and/or fragmentation of black liquor char particles [50]. Carryover particles range in size between 100 μm and 3 mm and form hard and tenacious deposits on heat transfer surfaces. Carryover which is partially oxidized smelt and/or unburned black liquor is entrained in the flue gas and is carried to the upper furnace [47].



Figure 1.1 Schematic diagram of a kraft recovery boiler

Deposits on heat transfer surfaces in the upper furnace are mainly formed by carryover particles. Carryover particles may strike and adhere to the tube surfaces depending on the flue gas temperature, boiler operating conditions, and the concentration and composition of carryover particles in the flue gas [47].

The conditions in a kraft recovery boiler are complex due to the high gas temperature and it is not feasible to conduct experiments in the boiler. Therefore, an entrained flow reactor (EFR) was constructed at the University of Toronto to study the dynamics of carryover deposition and parameters affecting the deposition process. These parameters include particle size, composition (chloride, potassium and carbonate) and velocity, EFR temperature, gas velocity, and the surface temperature of the deposit-collecting probe.

Previous studies [41] clearly indicate that the dynamic deposition of carryover on the probe is primarily a function of the liquid content of the carryover upon impact. Secondary parameters that affect deposition are carryover impact velocity and temperature.

Synthetic carryover composition, size and residence time and EFR operating conditions determine the liquid content, temperature and velocity of the synthetic carryover [42].

A quantitative measure of the deposit growth rate requires knowledge of carryover liquid content, temperature and velocity at the time of impact with the heat transfer surface. Therefore, the objective of this thesis is the development of a Computational Fluid Dynamics (CFD)-based algorithm to predict carryover temperature and liquid content as a function of particle size and composition. Direct development and substantiation of such an algorithm would be difficult for the convection section of the boiler, however the wealth of experimental data from the EFR under well-controlled conditions provides an excellent database and will be used to develop the algorithm. The particle-tracking algorithm will then be used to describe the path, temperature, and liquid content history of individual particle through a simplified upper furnace model of a kraft recovery boiler.

The relevant literature related to the objective of the present study is reviewed in Chapter 2. Chapter 3 describes the EFR, its components, and operating conditions. The numerical methods are described in Chapter 4 including a general description of the finite volume method used to predict velocity and temperature fields, a detailed description of the particle temperature and liquid content tracking algorithm and finally the details of the EFR and the simplified upper furnace models. The results of the EFR and upper furnace simulations are given in Chapter 5. In Chapter 6, practical implications to this study are presented followed by the conclusions and recommendations in Chapters 7 and 8, respectively.

2. Literature Review

2.1 Fireside Deposits

In the kraft pulping process a caustic solution of sodium hydroxide (NaOH) and sodium sulfide (Na₂S), called white liquor, is used to dissolve the lignin content of the wood and separate the wood fibres [18]. The spent pulping liquor, called black liquor, contains pulping chemicals and dissolved substances. The pulping chemicals are recovered by concentrating the black liquor and burning it in a kraft recovery boiler. The recovery boiler has two main functions: to recover and recycle the inorganic pulping chemicals, and to generate power and steam from the combustion of organic materials in black liquor [1].

Black liquor, on a dry basis, contains 40 to 50 % inorganic material, making it one of the highest ash containing industrial fuels. As black liquor is burned in the furnace, the high ash content and the low melting temperature of the ash cause problems associated with fly-ash deposition on heat transfer surfaces in the convective section. The growth of deposits reduces the heat transfer efficiency of the boiler and results in a lower superheater steam production rate [47]. Massive deposits may restrict the flue gas flow in the upper furnace and lead to costly unscheduled boiler shut downs.

There are three basic types of fly ash particles laden in recovery boiler flue gases [47]: carryover, fume, and intermediate-sized particles.

Carryover:

Carryover deposits are formed by the inertial impaction of molten or partially molten smelt particles, or entrained black liquor droplets on the heat transfer surfaces. As black liquor is sprayed into the boiler, droplets over the size range of 0.5 to 5 mm form and undergo four stages of physical change: drying, devolatilization, char burning, and smelt reaction. During drying, the black liquor swells to roughly 3-4 times the initial volume. The black liquor solids continue to swell during the devolatilization or pyrolysis process, and the maximum swollen volume is reached at the end of this stage [54]. During this stage the organic material of the particles are degraded into tar and pyrolysis gases [17]. Some entrainment of particles in the flue gas concurrently occurs as particles increase in size and density decreases [2]. Carryover has a composition similar to partially or fully oxidized smelt as shown in Figure 2.1(a). Carryover particles mainly contain 60-70% sodium carbonate, 20-30% sodium sulphide and a small fraction of unburned organic materials [47]. However, the composition of carryover changes as it travels to the upper furnace, where most of sodium sulphide is oxidized to sodium sulphate. Also, carbonates and some alkali compounds form sulphates after reacting with the sulphur compounds in the flue gas. A typical carryover deposit has a composition shown in Figure 2.1(b).

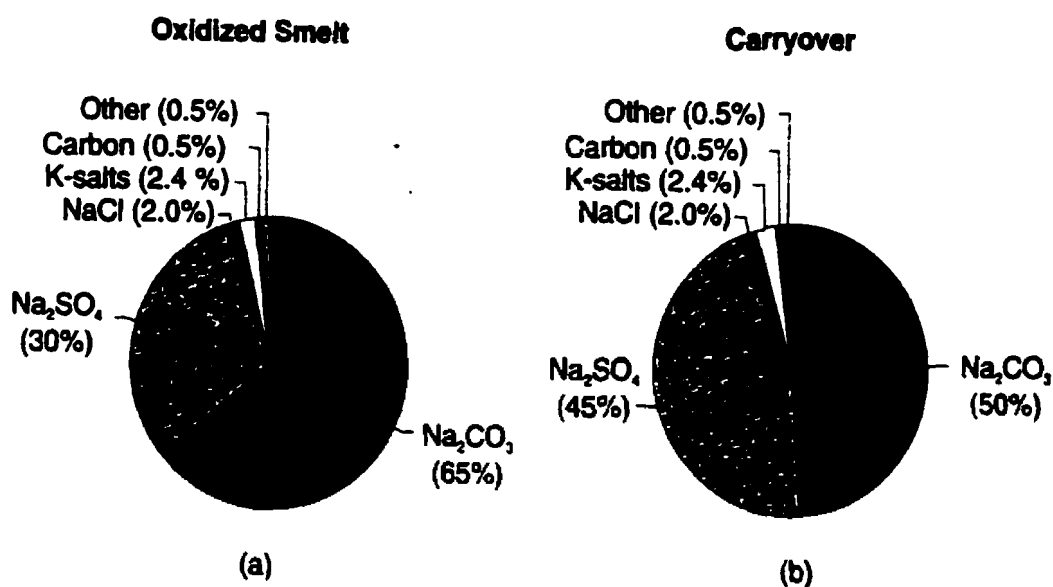


Figure 2.1 Composition of oxidized smelt (a) and carryover deposition (b) [47]

Fume:

Fume formation is a result of condensation of sodium and potassium vapour in the flue gas. Fume particles are in the size range of 0.1 to 1 μm and they form white and usually soft deposits [45]. Due to the reduction condition in the lower furnace, the sulphur in the flue gas is in the form of reduced sulphur gases such as H_2S . The H_2S in the flue gas is converted to SO_2 due to the oxidizing environment in the upper furnace. The SO_2 then reacts with hydroxides and produce sulphates [45]. As illustrated in Figure 2.2 fume mainly contains sodium sulphate and a small amount of sodium carbonate. It has higher contents of chloride and potassium compared to carryover. Fume composition is greatly influenced by the bed temperature in the lower furnace; more fume is produced in boilers operating at high bed temperatures.

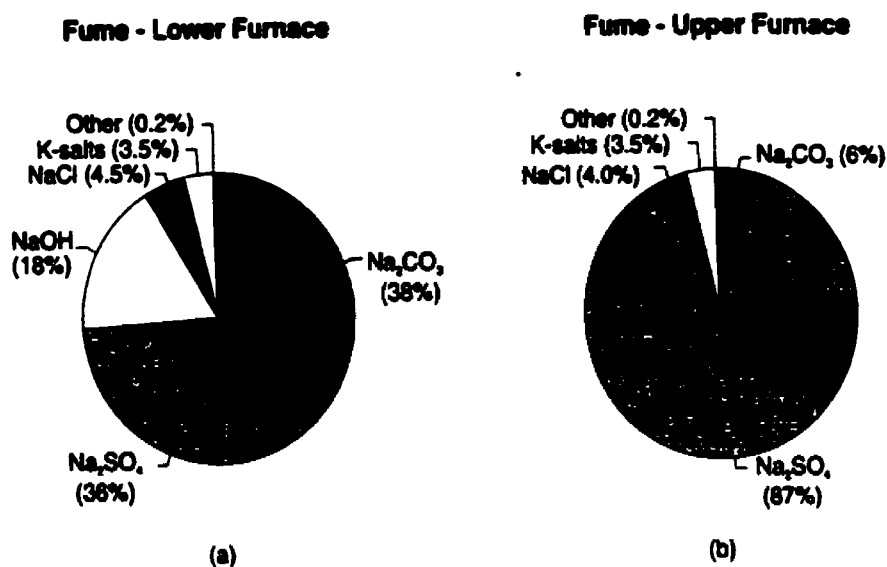


Figure 2.2 Composition of fume deposits in lower furnace (a) and upper furnace (b)

Intermediate-sized particles:

Intermediate-sized particles are formed during the devolatilization stages of black liquor combustion. The eruption of water and pyrolysis gases from the surface of the liquor drops during combustion results in the ejection of liquor droplets, in the size range of 1-100 μm , into the flue gas. Also, impaction of large molten particles on a tube surface can result in the ejection of tiny droplets, forming intermediate-sized particles. The chemical composition of the intermediate particles is close to that of an oxidized smelt [41].

Since deposits are a mixture of carryover, fume particles, and intermediate-sized particles, their composition lies among that of these three, with varying sulfate and carbonate composition in different locations in the boiler.

2.1.1 Thermal and Radiative Properties of Fireside Deposits

Since deposit composition varies with location in the boiler, thermal and radiative properties also vary. Like most mixtures of chemical compounds, recovery boiler deposits have two distinct melting temperatures. The first melting temperature and the complete melting temperature. The first melting temperature is the temperature at which the deposit begins to melt and the first liquid phase appears in the deposit. The complete melting temperature is the temperature above which the deposit is completely molten. There are two other important temperatures between the first melting and complete melting temperatures: The sticky temperature, T_{STK} , at which the deposit contains enough liquid content (~ 15 to 20 %) to become sticky, and the radical deformation temperature, T_{RD} , defined to be the temperature at which the liquid content of the deposit is so high (~ 70 %) that the deposit runs off the surface [45]. The sticky temperature and radical deformation temperature are important parameters in determining the rate of deposition in the superheater and boiler bank regions [17,44,47].

The radiative properties of particles and deposits on heat transfer surfaces have a large impact on the heat transfer rate in a kraft recovery furnace [53]. Understanding the thermal properties of deposits, and deposit formation may improve strategies for cleaning the heat transfer surfaces and increasing runtime between boiler shutdowns [53].

Radiation properties of black liquor char, smelt and ash can be approximated by the large particle limit since these particles are typically greater than 100 μm in diameter, which is larger than the wavelength of infrared radiation in the furnace [53]. The emission or absorption by the inorganic materials entrained by combustion gases in recovery furnaces are not significant compared to those from H_2O and CO_2 gases. However, fume has a

large effect on radiative scattering, especially if the fume particles are formed by condensation of inorganic vapors in the upper furnace and convection section [53].

Figure 2.3 shows the scattering and absorption efficiencies of ash particles as a function of temperature and particle diameter.

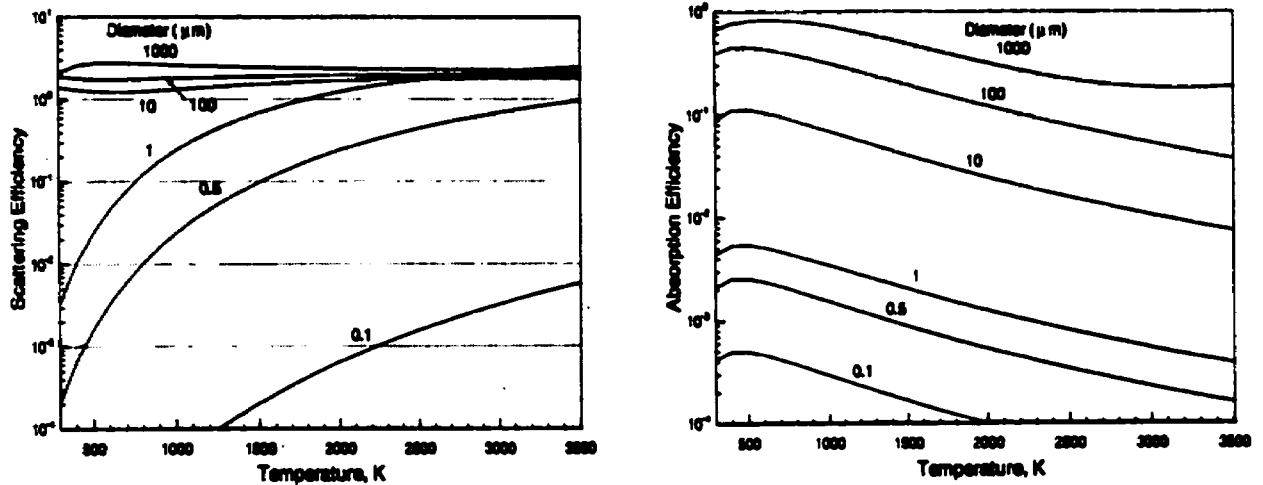


Figure 2.3 Absorption and scattering efficiencies for spherical particles of recovery boiler ash [53]

Black liquor, char and molten smelt deposits have high emissivities that decrease with temperature. However, fume deposits have a low emissivity that decreases with temperature of the radiation source as shown in Figure 2.4. The fume deposits appear white in the visible range of the radiative spectrum since they have a low emissivity.

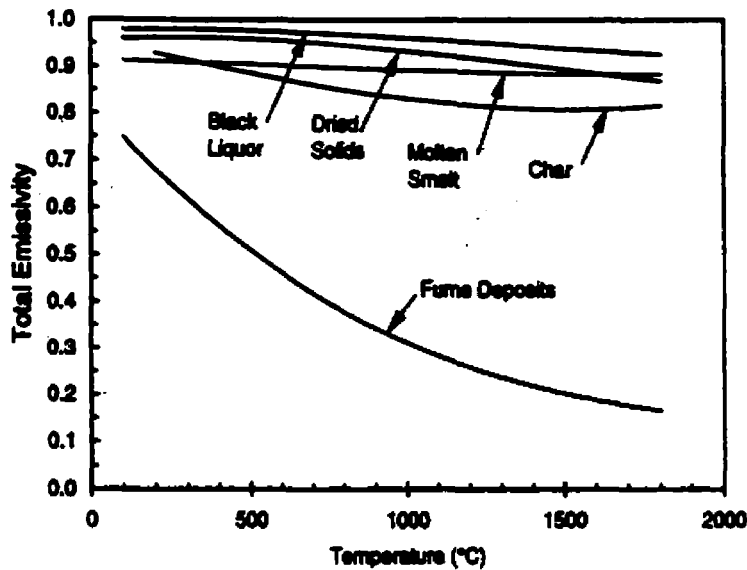


Figure 2.4 Emissivity correlations for black liquor, dried solids, char, molten smelt and fume deposits [53]

In the lower furnace, values of surface absorptivity and emissivity are high (~ 0.9) since char and molten smelt form deposits on the furnace walls. In the upper furnace, fume deposits on the walls are the cause for much lower emissivity (~ 0.4) [53].

2.1.2 The Effect of Chloride and Potassium on Deposit Stickiness

Both chloride and potassium lower deposit melting temperatures, however, their impact on deposit thermal properties is different [47]. Chloride with a concentration higher than 1 mole % $Cl/(Na+K)$ does not lower the deposit's first melting temperature. However, an increase in deposit chloride content at temperatures higher than the first melting temperature, increases the deposit liquid content. Figure 2.5 shows the sticky temperature zone as a function of chloride content for a typical carryover deposit containing 5 mole % $K/(Na+K)$. As the chloride content increases from 1.5 mole% to 9 mole% $Cl/(Na+K)$, the sticky temperature decreases from 700°C to 560°C.

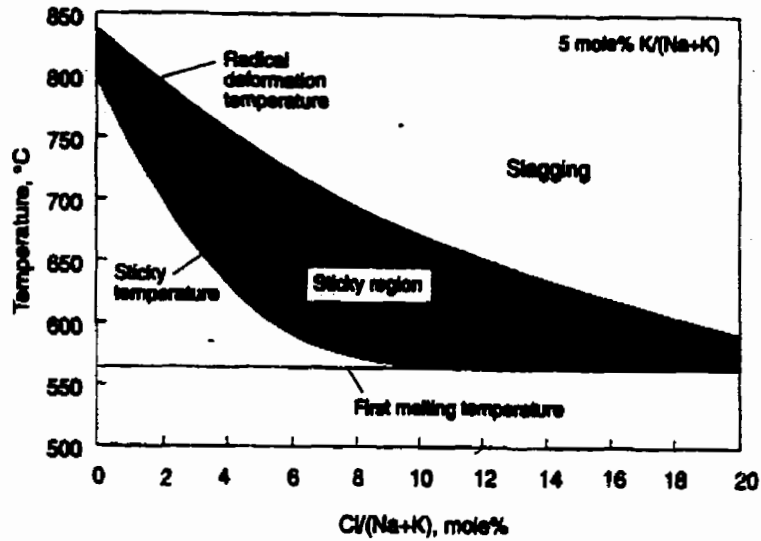


Figure 2.5 The effect of chloride on the sticky temperature zone [47]

Potassium lowers the first melting temperature as its concentration increases. However, potassium concentration has almost no impact on deposit liquid content. Figure 2.6 shows the sticky temperature of carryover deposits as a function of chloride and potassium content.

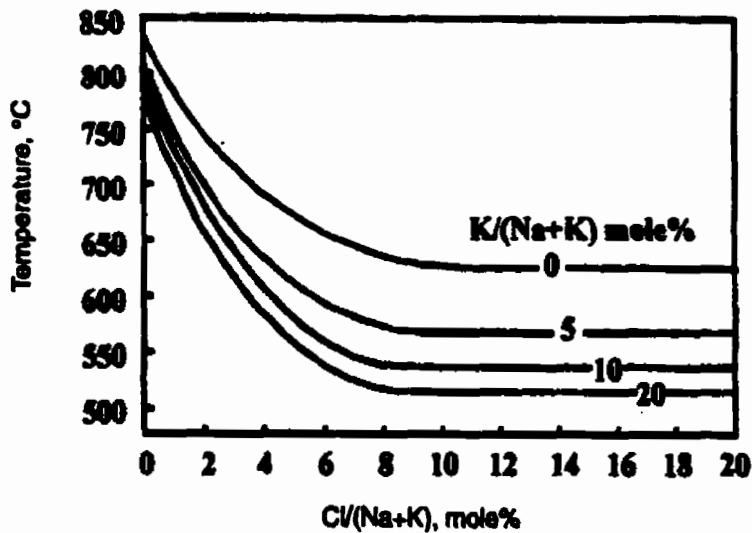


Figure 2.6 The effect of chloride and potassium on sticky temperature [46]

The difference between the effect of chloride and potassium content implies that the sticky temperature and radical deformation temperature are primarily a function of chloride content in the deposits and not potassium.

Since at a given temperature the liquid content is a function of composition, understanding of phase equilibrium and the effect of ionic materials on the first melting temperature is of great importance [48]. As discussed before, carryover deposits mainly contain Na_2SO_4 , Na_2CO_3 , Na_2S , NaCl and potassium salts. The phase equilibrium involving multicomponent ionic compounds, such as carryover deposits, is very complex and therefore the system is simplified into binary systems.

The binary system of Na_2SO_4 - NaCl , shown in Figure 2.7, forms a eutectic mixture.

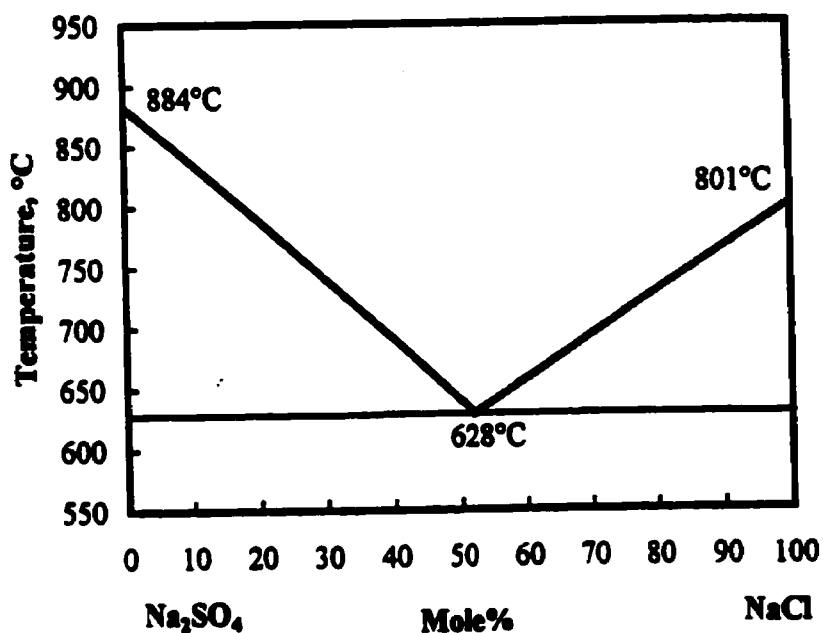


Figure 2.7 Phase diagram of the system Na_2SO_4 - NaCl [11]

In a eutectic mixture, the two compounds have different crystal structures and stay in their individual crystal forms at temperatures below the eutectic temperature. Above the eutectic temperature and in the liquid phase region of the diagram, the compounds dissolve in each other and form a melt that contains individual ions. The ionic melt solidifies and becomes a mixture of original compounds, when it is cooled to a temperature below the eutectic temperature. Examples of binary systems that form a eutectic mixture are $\text{Na}_2\text{SO}_4\text{-Na}_2\text{CO}_3$, $\text{Na}_2\text{SO}_4\text{-K}_2\text{SO}_4$ and NaCl-KCl [48].

2.1.3 The Role of Particle Liquid Content in Carryover Deposition

Deposit stickiness is an important parameter to determine the deposition rate of carryover particles on heat transfer surfaces. Previous studies by Isaak *et al.* showed that deposit stickiness under static conditions is a function of liquid phase [25,26]. Since Isaak's experiments were based on stagnant conditions, the effect of particle size, composition, and velocity were not taken into account. Therefore, Shenassa [41] conducted further studies on the effect of liquid content on carryover deposition using an Entrained Flow Reactor (EFR). The EFR was designed to simulate the conditions particles experience during their passage through the superheater section of the boiler. Studies [41] showed that temperature, chloride content and particle size have a significant effect on the deposition of synthetic $\text{Na}_2\text{SO}_4\text{-NaCl}$ particles. When the gas temperature in the EFR was about 800 °C, there was little deposit formed on the deposit-collecting probe until the chloride content exceeded 3 mole% $\text{Cl}/(\text{Na}+\text{K})$. However, when the EFR gas temperature was increased to 880 °C, a lower amount of chloride content, about 1 mole% $\text{Cl}/(\text{Na}+\text{K})$, was required for deposition to occur [42]. It was concluded that a higher gas

temperature results in a higher particle temperature and liquid content, therefore lower chloride content is required for particles to deposit [42]. Further, it was suggested that since large particles ($\sim 590 \mu\text{m}$) can not be cooled as fast as small particles they will contain higher liquid content in the superheater region [42].

For a deposit to be sticky, it must contain sufficient amount of liquid phase, which increases with temperature and chloride content at the temperature above the first melting temperature [47]. Massive deposit accumulation occurs only when the deposit is in the temperature range between the sticky and radical deformation temperature. The region bounded by these two temperatures is called the sticky zone. Deposits with temperatures outside the sticky zone, either do not have enough liquid phase to be sticky or their liquid content is so great that they slag and do not build up [45].

2.1.4 Particle Transport Mechanisms

Deposition of carryover particles on heat transfer surfaces is affected by particle size, gas flow characteristics, heat transfer surface conditions and tube geometry [47]. Particles can be transported to heat transfer surfaces by several mechanisms such as: molecular diffusion, brownian motion, thermophoresis, turbulent eddy impaction and inertial impaction [24].

Molecular diffusion is most significant for particles smaller than $0.1 \mu\text{m}$ [47]. These particles obey the gas law based on kinetic theory and they follow the flue gas streamlines with velocities close to those of gas molecules. Particles' collision rate and their mean free path depend on their concentration in the gas stream.

Brownian motion applies to particles in the size range of $0.1\ \mu\text{m}$ to $1\ \mu\text{m}$. These particles collide with gas molecules thus they move randomly in the gas stream. External forces such as inertial or magnetic forces can also affect the motion of these particles [23].

The motion of particles toward a colder region in a gas with a temperature gradient is due to a force called thermophoresis. This force is more significant for particles in the size range of $0.1\ \mu\text{m}$ to $10\ \mu\text{m}$. The magnitude of the thermal force depends on gas and particle properties, as well as the temperature gradient. This thermal force is due to the uneven collision of gas molecules on the warm side causing particle transport towards the colder side, which can result in particle deposition on a cold surface [23].

The turbulent eddy impaction mechanism applies to particles larger than $1\ \mu\text{m}$. Particles deposit on the surfaces because of the fluctuating velocity components of gas eddies in the turbulent boundary layer. The gas eddies in the turbulent boundary layer give enough momentum to particles to transport them across the laminar sub-layer and deposit them on the heat transfer surfaces.

For larger particles, inertial impaction is the dominant transport mechanism. These particles have a much greater mass and therefore much greater inertia within the carrier gas. As a result they have sufficient momentum to move independently of local variations in the gas flow pattern and impact on the heat transfer tubes [24].

2.1.5 Curvilinear Motion of Particles

A particle laden flue gas flowing across a tube will have curvilinear streamlines. Depending on particle size, tube geometry, gas velocity and gas properties, the particles may contain sufficient inertia to deviate from the flue gas streamlines and hit the tube surface. A dimensionless number called the Stokes number (Stk) is introduced to characterize the curvilinear motion of particles. It is defined as the ratio of the stopping distance of a particle to a characteristic dimension of the obstacle [24]. The Stokes number for a flow perpendicular to a cylinder of diameter D_t can be expressed as [23]:

$$Stk = \frac{\rho_p D_p^2 U}{9\mu_g D_t} \quad [2-1]$$

where, ρ_p , D_p , U , and μ_g , are respectively particle density, particle diameter, free gas velocity, and gas viscosity. Figure 2.8 shows the gas flow and particle trajectories around a circular tube.

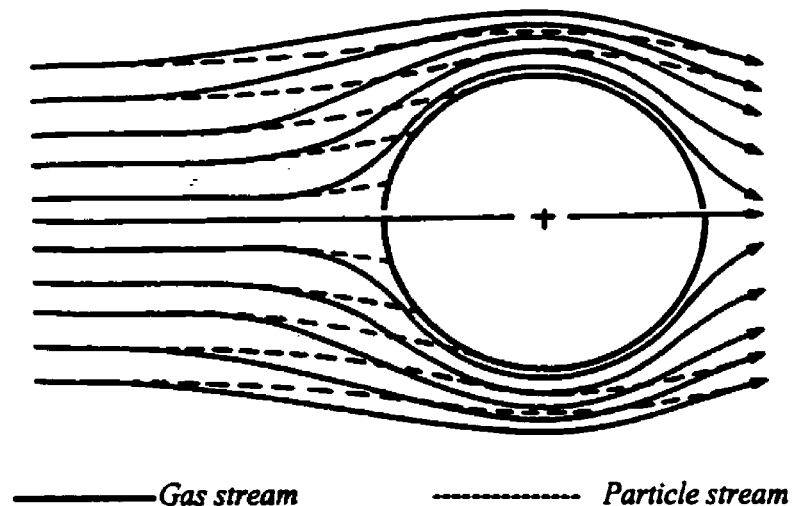


Figure 2.8 Particle trajectories around a circular cylinder [55]

When $Stk \gg 1$, particles continue moving in a straight line when the gas turns; when $Stk \ll 1$, particles follow the gas streamlines. As the Stokes number approaches zero, particles follow the flue gas streamlines perfectly. Equation [2-1] is valid for particles with $Re_p < 1$, where particle Re number is expressed as:

$$Re_p = \frac{\rho_g D_p U_p}{\mu_g} \quad [2-2]$$

Israel and Ronsner defined a generalized Stokes number [27], called effective Stokes number Stk_{eff} , to account for the non-Stokesian drag on the particles. The effective Stokes number is defined as:

$$Stk_{eff} = Stk * \psi (Re_p) \quad [2-3]$$

where the non-stokes drag correction factor ψ is defined as [38,55]:

$$\psi(Re_p) = 18.99 Re_p^{-2/3} - 47.77 \tan^{-1}(0.3975 Re_p^{1/3}) / Re_p \quad [2-4]$$

2.2 Plugging in Kraft Recovery Boiler

Plugging patterns differ throughout the boiler since the deposit chemistry, deposit formation mechanism and flue gas flow vary significantly with location in the boiler. In the lower superheater, deposits are mostly formed by carryover particles since the gas temperature is too high, about 800 °C, for vapors to condense. Molten carryover particles hit the tubes and form a hard deposit on the tube surfaces. However, as the deposit grows thicker, the outer surface temperature reaches the radical deformation temperature thus the deposit slags and stops growing. As a result plugging does not occur in this region [47].

In the upper superheater, the flue gas temperature ranges from 700 °C to 800 °C which is the sticky temperature zone for typical deposits. In this region, carryover particles are always sticky and they form deposits that continue to grow. Also, condensation takes place on cooled tube surfaces since the flue gas temperature is low. Therefore, massive deposit accumulation and plugging occurs in this section. Figure 2.9 shows the deposit accumulation pattern in a typical recovery boiler [47].

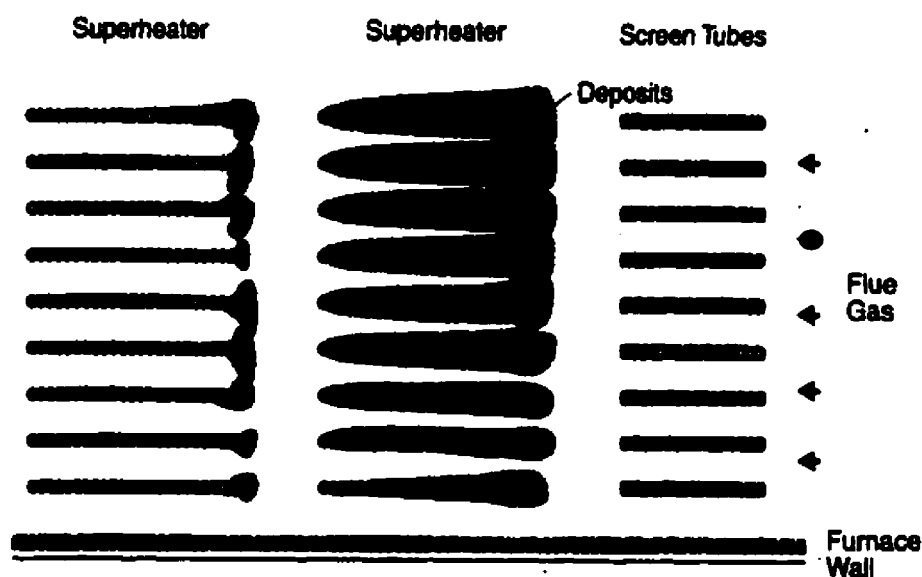


Figure 2.9 Deposit accumulation pattern in superheater region [47]

At the boiler bank inlet, the flue gas temperature ranges from 550 °C to 700 °C which is close to the minimum sticky temperature. Therefore, carryover particles may or may not form deposits depending on their composition. At the centre of the boiler bank and economizer regions, fume is the dominant deposit since the flue gas temperature is too low for carryover particle to be sticky. Fume deposits are usually easy to remove unless a suitable condition exists that makes them resistant to sootblowing and that causes plugging in the generating bank [47].

2.3 Numerical Modeling of Dilute Gas-Particle Flows

A dilute gas-particle flow is a flow in which the local aerodynamic forces govern the particle motion. In a dense gas-particle flow, the particle motion is controlled by particle-particle collision [12].

The dilute or dense nature of a flow depends on loading, and increasing the loading leads to a dense flow. The relative volume of particles in a gas flow is quantified by the volume fraction. Specifically, the volume fraction is the volume of a phase (discrete phase, for example) per unit volume of mixture [12]. If the particle concentration is low enough such that the presence of the particles does not affect the gas flow, each particle can be treated individually [39].

There are two approaches used to model particulate two-phase flows [4], a Lagrangian or 'tracking' method and an Eulerian or 'two-fluid' method.

In the Lagrangian approach particles are treated as a discrete phase in the carrier fluid and their trajectories are calculated. Using a Lagrangian reference frame, a particle source term is estimated for each computational cell visited by the particle to account for the coupling between the fluid and the particles [4]. Particle position, temperature, composition and velocity can all be obtained by integrating ordinary differential equations representing conservation of motion and energy [7].

In the Eulerian method, the cloud of particles is treated as a continuum and appropriate governing equations are solved for both phases. The source terms in the continuum equations for both phases accounts for the mutual coupling. Eulerian models have found applications mainly in two-phase flows, where the knowledge of the exact position and velocity of every particle in the flow is not necessary [7].

2.3.1 Particle Velocity in Dilute Two-Phase Flow Systems

When a particle, or a cloud of particles of low concentration, is introduced into a fluid the response of the particle depends on the relative velocity of the particle and the fluid. In this thesis work it is assumed that particle-particle interaction is negligible and the presence of the particle does not have a significant effect on the flow pattern. If the particle velocity is different from the gas velocity a force, called drag force, is exerted by the gas on the particle and it depends on the relative velocity [31,39]. The equation of motion of a single particle is

$$m_p \frac{dU_p}{dt} = m_p g + \frac{1}{8} \pi C_D \rho_g D_p^2 (U_g - U_p) |U_g - U_p| + F_x \quad [2-6]$$

where m_p , U_p , C_D , and F_x are respectively particle mass, particle velocity, drag coefficient, and other forces such as buoyancy. At very small Reynolds numbers ($Re \sim 0.1$), the flow is called Stokes flow and the drag coefficient is defined as

$$C_D = \frac{24}{Re_p} \quad [2-7]$$

and at high Reynolds number ($Re_p \sim 10^3$) the drag coefficient becomes approximately constant at about 0.4 [31]. However, in the intermediate range of Reynolds number, which is the range of current practical interest, the drag coefficient value becomes a complicated function of Re . There are several equations in the literature for calculating the drag coefficient of spherical particles moving in a fluid. Morsi and Alexander proposed the following three-parameter general correlation [31]

$$C_D = a_1 + \frac{a_2}{Re_p} + \frac{a_3}{Re_p^2} \quad [2-8]$$

where a_1 , a_2 and a_3 are constants that apply for smooth particles for several ranges of Reynolds number. Table 2-1 shows the constant values at different Re_p ranges [31].

Table 2-1 The value of the constants over several Re number ranges [31]

a_1	a_2	a_3	Re_p
3.69	22.73	0.0903	0.1-1.0
1.222	29.1667	-3.8889	1.0-10.0
0.6167	46.5	-116.67	10.0-100.0

The drag coefficient calculated using this correlation is within 1-2% of experimental data [31].

For non-spherical particles, the following correlation is proposed by Haider and Levenspiel [20]:

$$C_D = \frac{24}{Re} (1 + A Re_p^B) + \frac{C}{1 + \frac{D}{Re_p}} \quad [2-9]$$

where

$$A = \exp(2.3288 - 6.4581\Phi + 2.4486\Phi^2)$$

$$B = 0.0964 + 0.5565\Phi$$

$$C = \exp(4.905 - 13.8944\Phi + 18.4222\Phi^2 - 10.2599\Phi^3)$$

$$D = \exp(1.4681 + 12.2584\Phi - 20.7322\Phi^2 + 15.8855\Phi^3)$$

and Φ is the particle shape factor which is defined as the ratio of the surface of a sphere having the same volume as the non-sphere particle to the actual surface area of the non-sphere particle [20].

Particles may reach their terminal velocity, V_{ST} , as they travel through the EFR.

The terminal velocity is reached when the drag force acting on the particle is balanced by gravity force and can be determined from the equation

$$V_{ST} = \left[\frac{4\rho_p D_p g}{3C_D \rho_g} \right]^{0.5} \quad [2-10]$$

A trial and error approach is needed to solve for V_{ST} since to calculate the terminal velocity the value of C_D is required, however, to obtain C_D the particle Reynolds number is needed, which can be calculated if V_{ST} is known [20].

2.3.2 Turbulent Dispersion of Particles

Turbulence plays a dominant role in determining particle dynamics in the kraft recovery boilers and any realistic model should account for the turbulent dispersion of particles [4]. There are two methods to model the turbulent dispersion of particles; the cloud tracking method, and the stochastic method [4,6].

In the Particle Cloud Tracking approach statistical methods are used to find the turbulent dispersion of particles about a mean trajectory. The mean trajectory is calculated from an ensemble average of the equations of motion for the particles represented by the cloud. The ensemble average is computed by introducing particles with many different release times and averaging the results as a function of residence time [8]. If the flow is at steady state, the ensemble average is independent of residence time. The cloud enters the domain either as a point source or with an initial diameter and expands due to turbulent dispersion as it is transported through the domain until it exits. The particle distribution in the cloud is defined by a probability density function (PDF) based on the position in the cloud relative to the cloud center [7,16,29].

The Stochastic method is a Lagrangian model that accounts for the effect of turbulent fluctuation on a particle trajectory using a random-walk approach. Each Particle is assumed to become entrained in large eddies as it moves through the flow [28]. In each eddy the properties are assumed to be constant but the properties change randomly from one eddy to the other. The particle is assumed to interact with eddies if the particle displacement in the eddy is smaller than a characteristic eddy size and particle interaction time is smaller than an eddy lifetime. This method is based on a statistical approach and a large number of particles should be tracked to obtain reliable statistical information [8,16].

The stochastic method accounts for local variations in the flow such as temperature, velocity, and species concentration and since it is recommended for complex geometries it is applied in the present boiler study.

2.3.3 Particle Temperature Estimation

To determine the temperature of a particle moving in a fluid; mass, energy and momentum equations should be solved for both phases. Different approaches have been used to accomplish this task. Han [21] proposed a two-fluid model approach leading to a system of equations for both phases. Conversely, Michaelides [30] simulated the two-phase flow as one fluid with variable density and heat capacity [9]. There are some simplified models proposed based on the solution of the heat transfer to the particles without considering the dynamical coupling. Some of the basic assumptions made in these simplified models are:

i) each particle has a uniform temperature, ii) the loading ratio is relatively small,

iii) particles have no effect on the fluid dynamic characteristics and iv) particle relative velocity is usually assumed to be zero [9]. Some of these assumptions, especially assumption iv), are too restrictive. Velocity measurements of the particles in a vertical tube by Tsuji [49] indicate that there are significant difference between the velocities of the flue gas and those of the 200- μm particles. Therefore, to yield better numerical results Avila and Cervantes [5] proposed an Eulerian-Lagrangian approach. They modeled the turbulent gas flow by a standard k- ϵ model and the particle flow by Lagrangian simulation. This model is more realistic in terms of considering the dynamics of gas-particle flows [9].

A particle moving through a fluid is heated by convection and radiation heat transfer if its temperature is cooler than the carrier gas and surroundings. Also, energy transfer occurs by conduction from the particle surface to its interior and temperatures at interior positions increase until the particle reaches steady-state [13]. Heisler [22] developed charts for determining complete temperature histories in spheres, cylinders, and plates based on the Biot number, Bi. Biot number is defined as particle internal resistance to heat conduction to resistance to convection across the fluid boundary layer and is estimated

by:

$$Bi = \frac{hL_C}{k_p} \quad [2-11]$$

where L_C is particle characteristic length and k_p is particle thermal conductivity. L_C is defined as the ratio of the particle's volume to surface area. For spheres it is equal to $d_p/6$. If $Bi \ll 1$, it can be assumed that the temperature distribution across the particle is uniform since the resistance to conduction is small, compare to the resistance to

convection [13]. In this study, the particle temperature estimation is based on a *lumped capacitance model* since the Biot number is small [41].

2.4 Numerical Modeling of Kraft Recovery Boilers

Obtaining a quantitative measure of the deposit growth rate is difficult in a boiler due to the high gas temperature and hostile environment. An alternative is to use numerical models to predict carryover deposition in the superheater section. Although a number of numerical models of kraft recovery boilers have been developed, very little has been done to predict deposit formation in the boiler. This is mostly due to the complexity of the deposition mechanism and lack of an algorithm that predicts the particle liquid content which has a significant role in deposition. Most numerical works are focused on solving the flue gas flow in the boiler and modeling the black liquor combustion. Flue gas flow through the upper furnace of the boiler was simulated by Shen *et al* [40] to examine the sensitivity of the velocity and temperature fields to some modeling assumptions. A mathematical model of the recovery boiler char bed and black liquor combustion was developed by Grace *et al.* [19]. Modeling studies have recently focused on aerosol dynamics and fume deposits in recovery boilers. Wessel *et al.* studied the effect of scattering by fume particles on radiative heat transfer in kraft recovery boiler [53]. Concurrent to the present study, Wessel *et al.* [52] developed an algorithm for deposit growth and properties that was implemented in a three-dimensional model of a recovery boiler.

2.5 Summary

Deposition of carryover particles on heat transfer surfaces of kraft recovery boiler causes problems such as plugging of flue gas passages and decreasing heat transfer performances. In previous studies it was found that the tendency for carryover particles, the predominant component of deposits in the superheater section, to stick to a surface is primarily a function of particle liquid content. Fundamental studies have been performed on deposition of carryover particles on cooled surfaces. However, there is limited work on particle temperature and liquid content measurement and estimation. Therefore, the present work focuses on: i) the development of a transient numerical model to predict carryover temperature and liquid content, ii) prediction of temperature and liquid content of particles in the EFR, and iii) prediction of carryover temperature and liquid content in the upper furnace of a kraft recovery boiler.

3. The Entrained Flow Reactor

In order to study the dynamics of deposition of carryover particles on superheater tube surfaces in kraft recovery boilers, a large laboratory-scale Entrained Flow Reactor (EFR) was built at the University of Toronto by Shenassa [41]. The EFR, shown schematically in Figure 3.1 simulates the conditions carryover particles experience during their passage through a kraft recovery boiler convection section.

3.1 Entrained Flow Reactor Components

The EFR is a down-flow laminar unit which consists of a gas combustion section, a heated section, and a non-heated section. The gas combustion section is located at the top of the heated section and it burns natural gas to produce flue gas with a temperature up to 1200°C. The generated flue gas passes through a honeycomb flow straightener prior to entering the heated section. Therefore, a uniform gas flow is provided in the reactor. The heated section is made up of five tubular furnaces that each can be controlled up to a maximum temperature of 1350°C. The deposit-collecting probe is positioned in the non-heated section. This section which is located below the last furnace of the heated section, makes deposit collection and optical measurement easier. An insulated chamber is used to cover this section to minimize the heat lost by convection heat transfer.

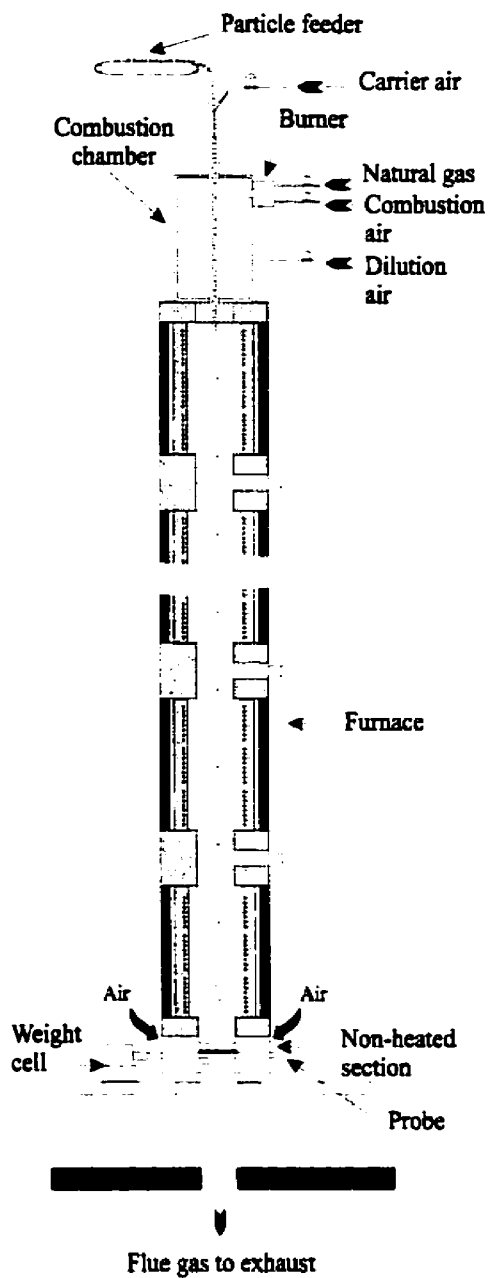


Figure 3.1 Schematic diagram of the EFR, internal diameter 18.1 cm, heated section height 6 m [41]

3.2 Entrained Flow Reactor Operating Conditions

In the gas combustion section natural gas is burned at a flow rate of 1 to 2.5 m³/h producing hot flue gas at a maximum velocity of 2.8-3 m/s. In this numerical study the gas velocity was set to 1.8 m/s since most of the previous experiments were performed at this velocity. The combustion gases generated in the combustion chamber are mixed with dilution air to produce gas with a desired temperature. To simulate the conditions in the upper part of the kraft recovery boiler, the temperature of the combustion gas entering the heated section and the EFR wall temperature were controlled at 800°C. However, when the gas enters the non-heated section its temperature decreases significantly.

The gas has a uniform flow at the entrance of the heated section due to the presence of the honeycomb flow straightener. The experimental results show that the design of EFR makes it almost impossible to have a fully developed flow inside the reactor. The reason is, the five tubes that form the heated section of the EFR are not aligned perfectly. Therefore, as the flue gas flow starts developing, its boundary layer gets disrupted by the joints between the tubes.

The temperature of the deposit-collecting probe, located in the non-heated section, is controlled at 500°C by cooled air. The probe is connected to an electromagnetic force compensation weight cell to measure the weight of particles depositing on the probe.

3.3 Pressure Measurement

The flue gas inside the reactor is exhausted to atmosphere via an induced draft fan. The inlet of the fan is located below the non-heated section. The static pressure of the flue gas at the inlet of the fan is required for defining a pressure boundary condition at the flow outlet in the EFR model. To measure the static pressure of the gas a pitot tube was used. The pitot tube was connected to a P3061 pressure transducer (Schaevitz Pressure Sensors, Durham Instruments) in the range of 0-2 in H₂O. First, the pressure transducer was calibrated using a digital manometer with a pressure range of 0-20 in H₂O. Figure 3.2 shows a schematic diagram of the pressure transducer calibration setup.

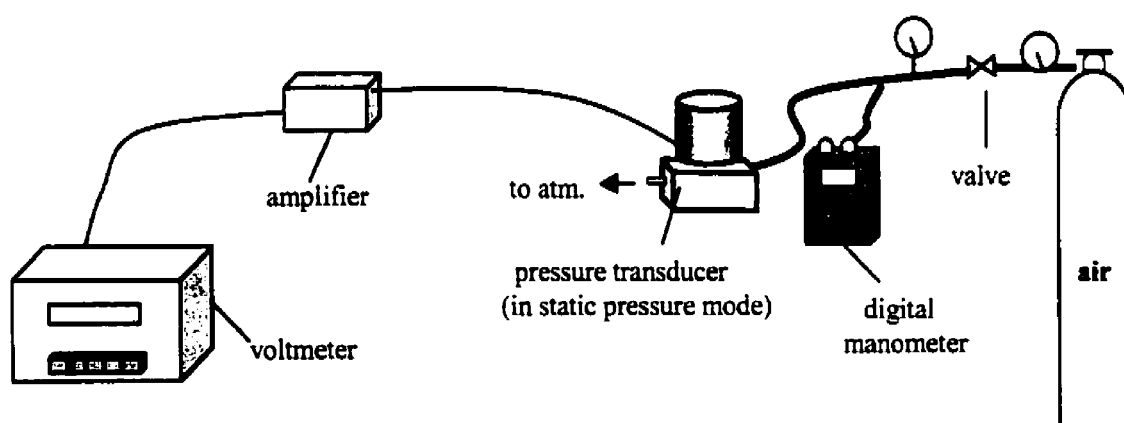


Figure 3.2 Schematic diagram of the calibration setup

The pressure of the airflow was changed from 0 to 2 in H₂O by adjusting the valve to determine a linear relationship between the output voltage and the static pressure.

After calibration, the pitot tube was placed at the inlet of the fan to monitor the static pressure. Pitot tubes are usually used to measure gas velocity. However, in this study the tube connected to the centre hole of the pitot tube, which shows the total pressure of the

gas, was open to the atmosphere. Therefore, the measured values show the gauge static pressure. Figure 3.3 shows the experimental setup for pressure measurements.

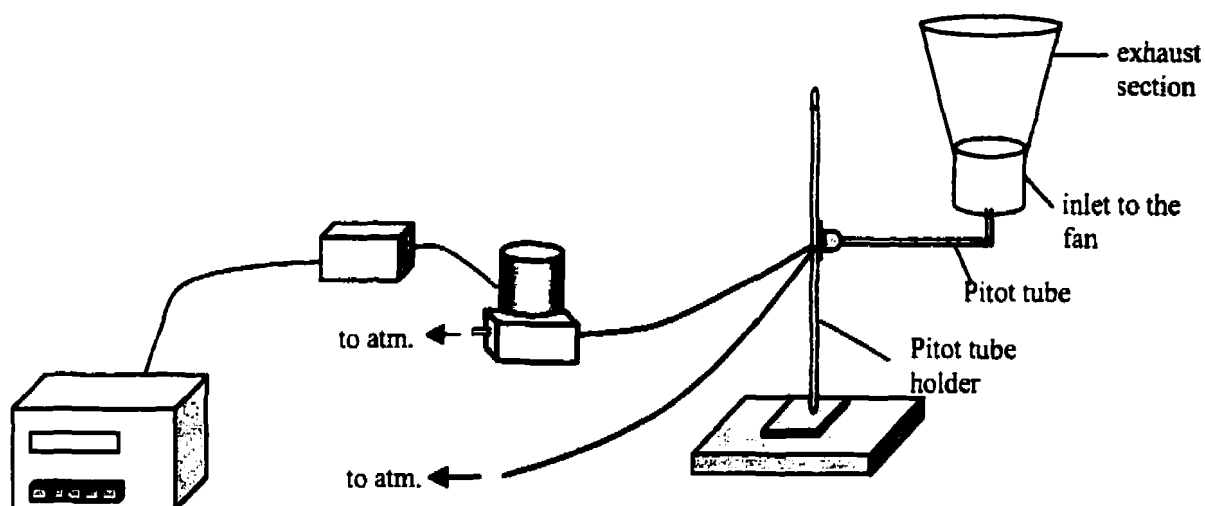


Figure 3.3 Schematic diagram of the experimental setup for measuring the static pressure at the inlet of the fan

Figure 3.4 shows the measured gauge static pressure results. From these measured static pressure values the outlet boundary condition can be determined at the exit of the exhaust section in the EFR model. The experimental errors in pressure measurements are associated with several factors such as; pitot tube vibration, pitot tube alignment in the flow, accuracy of the pressure transducer, and errors in calibrating the pressure transducer.

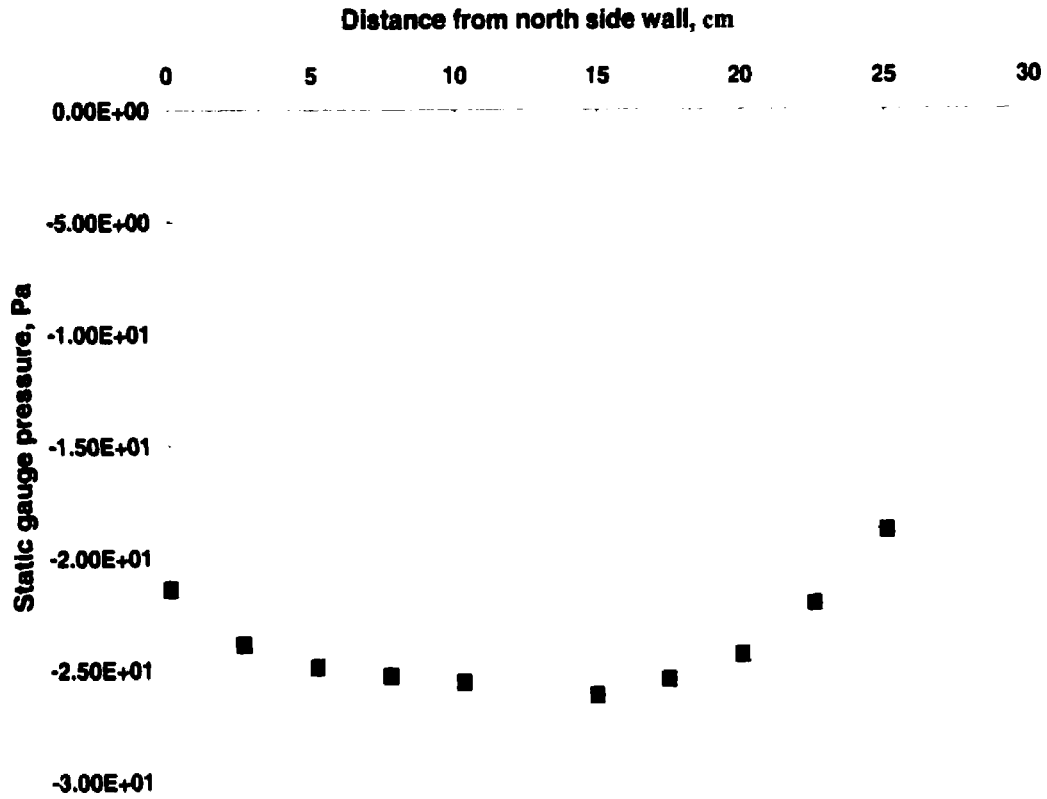


Figure 3.4 Measured static pressures at the inlet of the fan in the exhaust section

4. Numerical Method

As discussed earlier, carryover deposition is primarily determined by velocity, temperature, and liquid content of the carryover particles upon impact on heat transfer surfaces. In this chapter an algorithm to track the velocity, temperature, and liquid content of carryover that can be integrated within a commercially available computational fluid dynamics (CFD) package is described. As part of the simulation procedure the Navier-Stokes and energy equations are solved over the region of interest using the Finite Volume method to predict the velocity and temperature fields. Particle velocity and temperature are then predicted as they travel through the simulation region.

A summary of the Finite Volume method is presented in the first section. In the section that follows, section 4.2, the particle velocity and temperature-tracking algorithm is presented. The details of the EFR and simplified model of the upper furnace kraft recovery boiler are given in sections 4.3 and 4.4 respectively.

4.1 The Finite Volume Method

There are several methods which may be used to solve partial differential equations (PDE) that are approximated by a system of algebraic equations these include Finite Difference, Finite Element, Boundary Element, and Finite Volume. In this study the Finite Volume method was used since it is the most widely used method.

A general conservation equation can be formulated to describe the transport of mass, momentum, energy, turbulent kinetic energy, and dissipation rate of turbulent kinetic energy. If the dependent variable is denoted by ϕ , the general equation for steady flow in Cartesian tensor notation is

$$\frac{\partial(\rho u_j \phi)}{\partial x_j} = \frac{\partial}{\partial x_j} \left(\Gamma \frac{\partial \phi}{\partial x_j} \right) + q_\phi \quad [4-1]$$

where Γ is the diffusion coefficient, and q_ϕ is the source term. The quantities of Γ and q_ϕ depend on the particular meaning of ϕ . In the Finite Volume method, the integral form of the conservation equation is used:

$$\int_V \rho \phi v \cdot n dS = \int_V \Gamma \text{grad} \phi \cdot n dS + \int_\Omega q_\phi d\Omega \quad [4-2]$$

The first step in this method is to divide the computational domain into non-overlapping small control volumes (CVs) such that each CV surrounds a grid point. The integral conservation equations are then applied to each CV in the computational domain to solve for all ϕ defined at nodes. One of the main advantages of Finite Volume method is that the method is conservative, i.e., mass and momentum are conserved [33].

In Figure 4.1 typical two-dimensional (2D) and three-dimensional (3D) control volumes are shown.

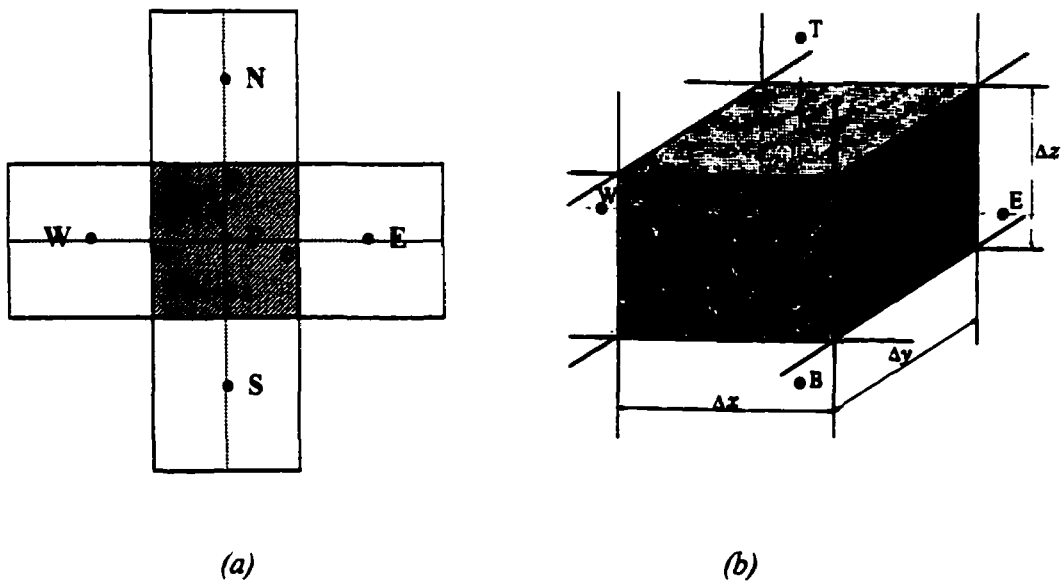


Figure 4.1 A typical CV for a Cartesian a) 2D grid and b) 3D grid [14].

They are quadrilateral and hexahedral. Other shapes of CVs, e.g. triangular and tetrahedral, can be used for complex geometries. For ease of development, the numerical method is developed in 2D; the extension to 3D is straightforward.

4.1.1 Discretization of Governing Equations

Each term of the conservation equation is approximated over a CV. The source term, e.g. the gravitational body force in the momentum equation, requires integration over the volume of a CV, while for convective and diffusive terms, the surface integral is evaluated on each surface of the CV. To approximate the source term, the average value of the source term in the cell is applied over the entire control volume. Therefore, the volume integral in equation 4-1 is replaced by the product of the cell-averaged term and the CV volume.

$$\int_V \rho \phi v \cdot n dS = \int_V \Gamma \text{grad} \phi \cdot n dS + \bar{q}_s V \quad [4-3]$$

If q_θ is constant or varies linearly within the CV, this approximation becomes exact; otherwise, it contains a second order error [14]. Higher order approximations require the values of q_θ at locations other than the cell centre.

For the convective and diffusive terms, the sum of integrals over each surface of the CV gives the total surface integral. To calculate the surface integral, the values of dependent variables need to be known along each surface. Since this information is not available, an approximation is introduced to calculate the values at the centre of the cell face (nodal values), i.e., e, w, n, s in Figure 4.1. A second order accurate approximation is used. Therefore, the surface integral is replaced by the product of the integrand at the cell face centre and the cell face area [14].

$$\sum_f^{N \text{ faces}} (\rho \phi v \cdot n)_f S_f = \sum_f^{N \text{ faces}} (\Gamma \text{grad} \phi \cdot n)_f S_f + \bar{q}_\theta V \quad [4-4]$$

where f is the index for each face of the CV and S_f is the face area. The values of dependent variable ϕ , the gradient of ϕ , and velocity are required in equation 4-4. These values are not known and they must be interpolated from the cell centre values, i.e., at P, N, S, W, and E in Figure 4.1. In this study, different discretization schemes are used to approximate the diffusive and the convective terms. The second order accurate central differencing scheme (CDS) is used to approximate the diffusive term where a linear interpolation between the two nearest nodes is assumed. Therefore, the diffusive flux through face “e” is given by:

$$\left[\Gamma \frac{\partial \phi}{\partial x} \right]_e \approx \Gamma_e \frac{\phi_E - \phi_P}{x_E - x_P} \quad [4-5]$$

when “e” is located midway between P and E. On a uniform grid, the truncation error is proportional to $(\Delta x)^2$. For non-uniform grids, the error term is proportional to the product of Δx and the grid expansion factor.

The convective term is approximated using an upwind differencing scheme (UDS) since the central differencing scheme can result in non-physical oscillatory solutions [14,33]. In this method, the face values are derived from quantities in the cells upstream, relative to the direction of the flow. Referring to Figure 4.1, if the flow is from left to right, ϕ_e is approximated as $\phi_e = \phi_p$. This approximation will never yield oscillatory solutions. However, it is only first order accurate which causes an artificial or false diffusion [14]. There are several other upwind schemes including second order upwind, power law, and QUICK (Quadratic Upwind Interpolation for Convective Kinematics).

In second order upwind, the cell face value is computed using the following expression:

$$\phi_f = \phi + \nabla\phi \cdot \Delta\vec{s} \quad [4-6]$$

where,

ϕ = cell centred value in the upstream cell,

$\nabla\phi$ = gradient of ϕ in the upstream cell,

$\Delta\vec{s}$ = displacement vector from the upstream cell centroid to the face centroid.

From the divergence theorem $\nabla\phi$ is determined as:

$$\nabla\phi = \frac{1}{V} \sum_f^{N_{faces}} \tilde{\phi}_f \vec{A} \quad [4-7]$$

Here the face values $\tilde{\phi}_f$ are computed by averaging ϕ from the two cells adjacent to the face [6]. In this study a second order upwind scheme was used for all the momentum equations.

Now that we have each term of the conservation equation approximated over a CV, the discretization schemes are incorporated into equation 4-4. The discretized transport equation, in general, is a nonlinear algebraic equation and it is constructed at the centre of each CV:

$$a_p \phi = \sum_{nb} a_{nb} \phi_{nb} + b \quad [4-8]$$

where the subscript nb refers to neighbour cells, and a_p and a_{nb} are the linearized coefficients for ϕ and ϕ_{nb} , and b contains all discretized source terms. To solve equation 4-8 an iterative process is required.

4.1.2 Iterative Solution and the SIMPLE Algorithm

The velocity components are governed by the momentum equations, which are particular cases of the general conservation equation for ϕ (where $\phi = u$ and $\Gamma = \mu$). To solve the flow field, there are four equations, three momentum equations and one continuity equation, and four unknowns. However, in the source term of the momentum equation a pressure gradient term appears. There lies the real difficulty in the calculation of the velocity field since there is no obvious equation for obtaining pressure [33]. The three most commonly used pressure –velocity coupling algorithms are: Semi-Implicit Method for Pressure linked Equations (SIMPLE), SIMPLE Consistent (SIMPLEC), and Pressure-Implicit with Splitting of Operators (PISO). The SIMPLE algorithm is the most popular method and was first suggested by Patankar and Spalding [34]. The SIMPLE algorithm is shown schematically in Figure 4.2 and begins with an initial guessed value for pressure at all grid points. The guessed pressure field is then used to solve the momentum equations. Since the pressure field was guessed the resulting velocity field will not

satisfy the continuity equation. To improve the guessed pressure, a pressure correction term based on the residual produced in the continuity equation is introduced:

$$a_p p'_p = \sum a_{nb} p'_{nb} + b_m \quad [4-9]$$

where p' is the pressure correction and b_m is the residual from the solution of the continuity equation.

In the SIMPLE algorithm, once the pressure correction has been solved, the pressures and velocities at point "P" in Figure 4.1 are updated using equation (4-10) and (4-11):

$$p_p = p_p^* + p'_p \quad [4-10]$$

$$u_{i,p} = u_{i,p}^* + A_p \left[\frac{\delta p'}{\delta x_i} \right]_p \quad [4-11]$$

where p'_p , p_p^* , and $u_{i,p}^*$ are respectively the pressure correction, guessed pressure, and calculated velocity. The pressure term in equation 4-11 is a discretized spatial derivative. Once the flow field is calculated, other discretization equations such as turbulent quantities can be solved. The procedure is repeated until the solution is converged. A point implicit (Gauss-Seidel) linear equation solver is used in conjunction with an algebraic multigrid (AMG) method to solve the resulting scalar system of equations for the dependent variable in each cell [14]. An under-relaxation scheme is used to approach convergence.

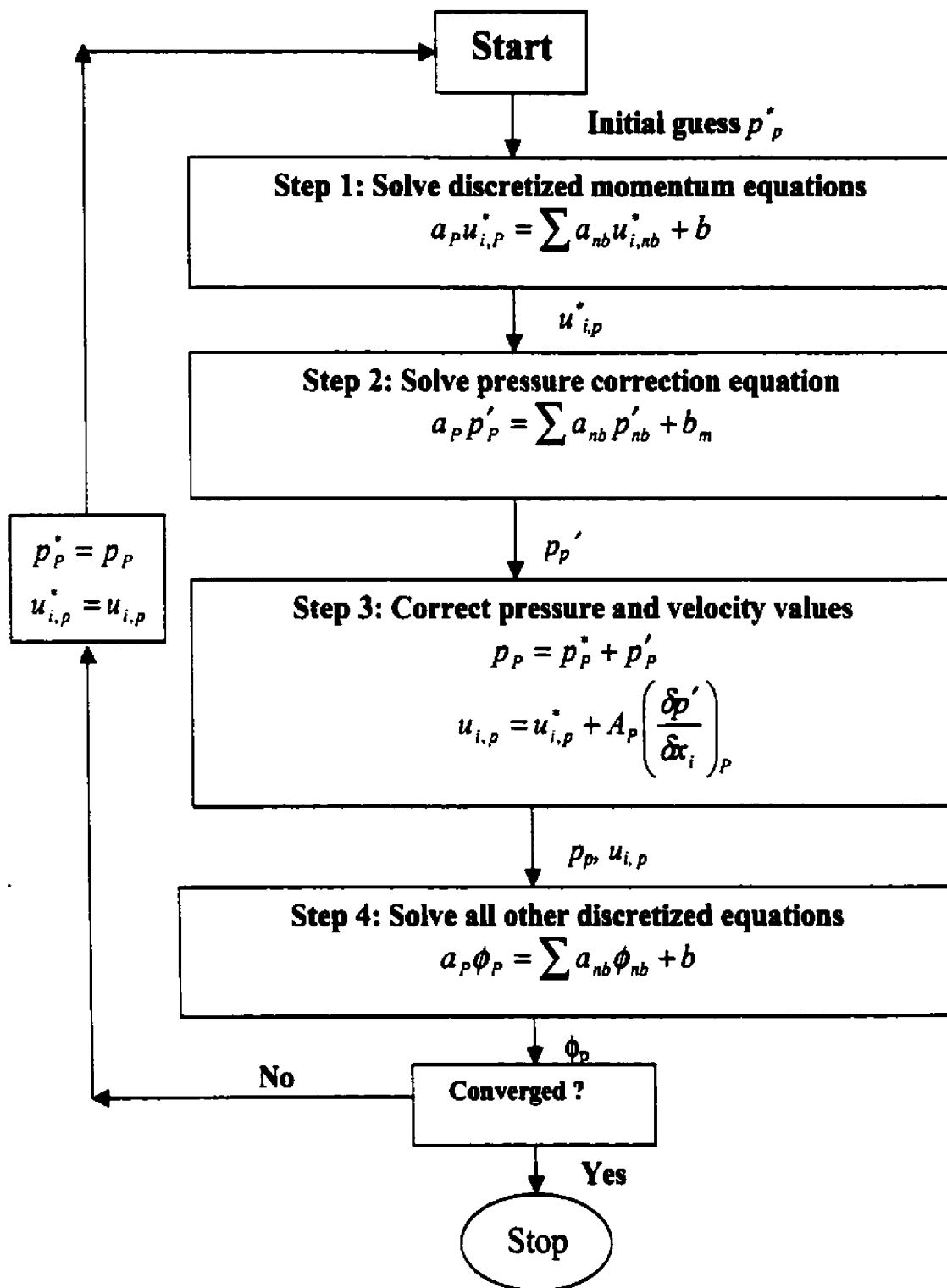


Figure 4.2 SIMPLE algorithm [35]

4.2 Particle Velocity and Temperature Estimation

In this section an algorithm is introduced to predict particle velocity, temperature, and liquid content. The algorithm is applied to regions of known velocity and temperature distribution as determined by a CFD simulation.

Particles are simulated in a Lagrangian frame using the discrete phase modeling option in Fluent™. The initial conditions that must be provided for discrete phase calculation are particle starting position, velocity, temperature, and diameter. Particles with different sizes and composition such as NaCl-Na₂SO₄-K₂SO₄ are introduced to the model. The physical properties of the particles are the same as those of previously studied molten synthetic carryover materials. A linear correlation was used to determine the particle latent heat of fusion, λ , based on the mass fraction of each component in the mixture and its latent heat of fusion.

4.2.1 Velocity Estimation and Turbulent Dispersion of the Particles

The trajectory of a discrete phase particle is predicted by integrating the force balance on the particle, which is written in a Lagrangian reference frame. This force balance equates the particle inertia with the forces acting on the particle, and can be written as:

$$m_p \frac{dU_p}{dt} = m_p g + \frac{1}{8} \pi C_D \rho_g D_p^2 (U_g - U_p) |U_g - U_p| + F_x \quad [4-12]$$

where m_p , U_p , C_D , and F_x are respectively particle mass, particle velocity, drag coefficient, and other forces such as buoyancy. The drag coefficient was calculated using the Morsi and Alexander's correlation [31]:

$$C_D = a_1 + \frac{a_2}{\text{Re}_p} + \frac{a_3}{\text{Re}_p^2} \quad [4-13]$$

where the a's are constants that apply for smooth spherical particles over several ranges of Reynolds number.

The trajectory equations are integrated stepwise over discrete time steps. Integrating equation 4-12 in time steps yields the particle velocity at each point of the trajectory. The particle time step is calculated using the following equation:

$$\Delta t = \frac{L_s}{U_p + U_g} \quad [4-14]$$

where L_s is the length scale and is equivalent to the distance that the particle travels between two time steps. Smaller values of length scale make the trajectory calculation more accurate.

Since the particle loading to both models was very low, it was assumed that particles have no effect on the continuous phase and an uncoupled approach was used. In the uncoupled approach, this two-step procedure completes the modeling effort, as illustrated in Figure 4.3.

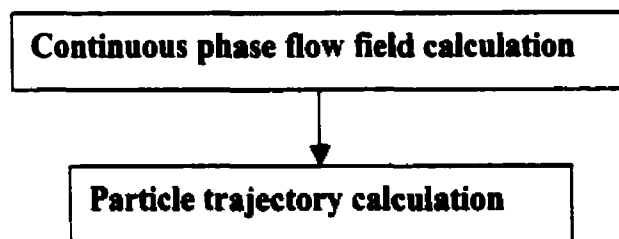


Figure 4.3 *Uncoupled discrete phase calculation*

To account for the effects of turbulent fluctuations on the motion of the particles, a stochastic discrete-particle approach can be used. In the stochastic tracking approach, the turbulent dispersion of particles is predicted by integrating the trajectory equations for individual particles, using the instantaneous fluid velocity, $U+u(t)$, along the particle path. The instantaneous characteristics of the gas are computed by adding random fluctuations to the mean flow solution from the $\kappa-\varepsilon$ simulation.

Thus,

$$U = \bar{U} + \gamma u' \quad [4-15]$$

where,

$$u' = \left(\frac{2}{3} \kappa \right)^{\frac{1}{2}} \quad [4-16]$$

where γ is a random number between -1 and 1 sampled from a normal distribution [16].

By tracking a sufficient number of representative particles, termed "number of tries", the random effects of turbulence on the particle dispersion may be accounted for. The more particle trajectories tracked, the more accurate the results. However, more computer CPU time will be required for tracking a large number of particles.

When a particle reaches a physical boundary (e.g. wall or inlet boundary) in the model, the fate of the trajectory will be different depending on the defined discrete phase boundary condition. The "reflect" boundary condition rebounds the particle off the boundary while "trap" boundary condition terminates the trajectory calculation. A "reflect" boundary condition was used for the EFR wall although the chance of a particle hitting the wall is very low. For the EFR deposit-collecting probe, the heat exchanger

tubes, and the walls in the upper furnace model, it was assumed that if a particle hits the probe or tube it would stick to it no matter the liquid content of the particle or tube thus a “trap” boundary condition was used.

4.2.2 Particle Temperature and Liquid Content Estimation

Particle temperature and liquid content was estimated based on the particle trajectory predictions and a lumped capacitance analysis. The analysis is presented for the case of a heated particle but the resulting algorithm applies equal to the case of a cooled particle. The algorithm was implemented as a user-defined function (UDF) in Fluent™.

Carryover has two melting temperatures since it is a mixture of at least two chemical compounds. Therefore carryover may undergo three different phases as it travels through the upper furnace or down the EFR prior to its impact on a heat transfer surface or the EFR probe. The temperature and the liquid content of the particles are estimated based on a lumped capacitance algorithm that accounts for the transition between phases using particle enthalpy. The three phases are as follows:

i) When the particle temperature is less than the first melting temperature (FMT) or more than the complete melting temperature (CMT), the heat absorbed by particle is used to increase the temperature. The particle temperature can be estimated using the following equation:

$$hA_p(T_g - T_p) + \varepsilon\sigma A_p(T_R^4 - T_p^4) = \frac{\partial(\rho_p V_p c_p T_p)}{\partial t} \quad [4-17]$$

where h is the convection heat transfer coefficient; A_p is the particle surface area; T_g and T_p respectively are gas and particle temperatures; σ is Stefan-Boltzman constant; ε , ρ_p ,

V_p and c_p are respectively particle emissivity, density, volume, and specific heat; λ is the particle latent heat of fusion; θ_R is the radiation temperature, $(I/4\sigma)^{1/4}$, where I is the radiation intensity (W/m^2) based on the P-1 radiation model [10,43]. The convection heat transfer coefficient, h , is estimated using the following correlation [36]:

$$Nu = hD_p/k_g = 2.0 + 0.6 Re^{1/2} Pr^{1/3} \quad [4-23]$$

where k_g , Re and Pr are gas thermal conductivity, Reynolds and Prandtl numbers respectively.

The energy equation was integrated in time and discretized using a first order Euler method. Equation 4-17 was approximated as:

$$T_p(t + \Delta t) = T_p(t) + \frac{(hA_p(T_g - T_p(t)) + \epsilon\sigma A_p(\theta_R^4 - T_p^4(t)))\Delta t}{m_p c_p} \quad [4-18]$$

where Δt is the integration time step.

ii) The second phase begins when the particle reaches its first melting temperature. In this case, the particle enthalpy increases while the temperature remains constant. The governing equation for this case is:

$$hA_p(T_g - T_p) + \epsilon\sigma A_p(\theta_R^4 - T_p^4) = \rho_p V_p \lambda \frac{\partial L}{\partial t} \quad [4-19]$$

Equation 4-19 is approximated as:

$$L(t + \Delta t) = L(t) + \frac{(hA_p(T_g - T_p(t)) + \epsilon\sigma A_p(\theta_R^4 - T_p^4(t)))\Delta t}{\rho V \lambda} \quad [4-20]$$

where, L is the particle liquid content and λ is the particle latent heat of fusion. At this point since the particle temperature is constant, the particle enthalpy was calculated to determine the transition to the next phase. The particle liquid content required in

equation 4-20, can be estimated using the lever rule for binary eutectic systems [41]. For example the lever rule correlation for particles with the composition of $\text{Na}_2\text{SO}_4\text{-NaCl}$ is:

$$L = \frac{M_{\text{NaCl}}}{(884 - T_p) / 4.8214} \quad [4-21]$$

where M_{NaCl} is the mole% $\text{NaCl}/(\text{NaCl} + \text{Na}_2\text{SO}_4)$. For ternary systems such as $\text{Na}_2\text{SO}_4\text{-NaCl-K}_2\text{SO}_4$, the lever rule is not applicable. Therefore, liquid content was interpolated from data obtained from Åbo Akademi University (ÅAU), Finland. The advanced multi-component phase equilibrium model developed in ÅAU was used to calculate the liquid content of the particles as a function of particle temperature and composition [46]. The data are in the form of lookup table which can be accessed by the code.

iii) Finally, when the temperature of the particle is between the first melting temperature and the complete melting temperature, its temperature and the liquid content change simultaneously. In this case the governing equation used to estimate the particle temperature is given by:

$$hA_p(T_g - T_p) + \varepsilon\sigma A_p(\theta_R^4 - T_p^4) = \rho_p V_p \left(\lambda \frac{\partial L}{\partial T} + c_p \right) \frac{\partial T_p}{\partial t} \quad [4-22].$$

Using the lever rule correlation to estimate the liquid content, equation 4-22 is discretized to:

$$T_p(t + \Delta t) = T_p(t) + \frac{(hA_p(T_g - T_p(t)) + \varepsilon\sigma A_p(\theta_R^4 - T_p^4(t)))\Delta t}{\rho_p V_p \left(\lambda \frac{L}{(884 - T_p(t))} + c_p \right)} \quad [4-24].$$

To estimate the liquid content in equation 4-22 using the thermodynamic data, the slope of the temperature-liquid content curve, $\frac{\partial L}{\partial T}$, at each point is required. Since the

equation of the curve is not known, a linear interpolation was used to calculate this term:

$$T_p(t + \Delta t) = T_p(t) + \frac{(hA_p(T_g - T_p(t)) + \epsilon\sigma A_p(\theta_R^4 - T_p^4(t)))\Delta t}{\rho_p V_p (\lambda \frac{L_2 - L_1}{T_2 - T_1} + c_p)} \quad [4-25]$$

The procedure given below was developed to solve the appropriate energy equation to estimate the particle temperature and liquid content. An enthalpy of the particle related to the enthalpy of the particle at 27°C is defined and introduced as:

Q_p = particle enthalpy – particle enthalpy at $T_p^o = 27^\circ\text{C}$;

1. set initial conditions: particle temperature $T_p^o = 27^\circ\text{C}$, particle liquid content = 0, and

$$Q_p = 0;$$

2. solve for the energy transferred by convection and radiation to the particle over Δt per unit mass, i.e. the sum of the left hand of equation 4-17, 4-19 or 4-22 times Δt divided by mass. The energy transferred equals the change in enthalpy of the particle, defined here as ΔQ_p ;

3. Q_p is accumulated at each time step to determine the status of the particle,

$$Q_p^{new} = Q_p^{old} + \Delta Q_p;$$

- i) if the particle is solid, i.e. $Q_p < c_p(T_{FMT} - T_p^o)$, then equation 4-18 is used;
- ii) if the particle is at the first melting temperature, i.e. $c_p(T_{FMT} - T_p^o) < Q_p < (c_p(T_{FMT} - T_p^o) + L_{FM}\lambda)$, the particle temperature is constant and first liquid content, L_{FM} , is estimated by substituting T_{FMT} in equation 4-21 or using the thermodynamic data. Particle liquid content during the first melting temperature is estimated using equation 4-20;
- iii) if the particle is melting and increasing in temperature, i.e. $(c_p(T_{FMT} - T_p^o) + L_{FM}\lambda) < Q_p$ and $L < 1$, equation 4-24 or 4-25 is used;

iv) if the particle temperature is more than the complete melting temperature, i.e.

$L=1$ and $T_p > T_{CMT}$, equation 4-18 is used.

4. Repeat steps 2 to 4 until particle hits the probe.

A user-defined function (UDF) was written in the C programming language to implement the above particle temperature algorithm. The FluentTM DEFINE_DPM_LAW macro and the user-defined functions were executed in FluentTM in a compiled form. After compiling the UDF, the particles were tracked again this time considering the above heat transfer calculation for particles.

The user-defined functions are given in the appendix.

4.3 Numerical Model of the Entrained Flow Reactor

To model the gas velocity and temperature fields in the reactor and in the non-heated section the governing Navier-Stokes and energy equations subject to the boundary conditions were solved. Based on the predicted gas velocity and temperature distribution in the EFR, particle velocity and temperature were estimated as it traveled down the reactor and upon its impact on the probe using the developed algorithm discussed in section 4.2.

4.3.1 EFR Geometric Model and Boundary Conditions

As discussed in the first sections, the first step in a modeling process is to divide the computational domain into small control volumes (CVs) or grids. Fitting a high quality structured mesh to the geometry of the EFR is difficult due to the complexity of the

As discussed in the first sections, the first step in a modeling process is to divide the computational domain into small control volumes (CVs) or grids. Fitting a high quality structured mesh to the geometry of the EFR is difficult due to the complexity of the geometry. Therefore, an unstructured grid with tetrahedral and hexahedral cells was applied to the calculation domain. A high mesh density was made around the probe due to the importance of the flow close to the probe. The mesh has 390,000 cells and it was generated in FluentTM's processor, GambitTM. Figure 4.4 shows a view of the mesh on the surface of the geometry in the non-heated section which will be extended throughout the volume.

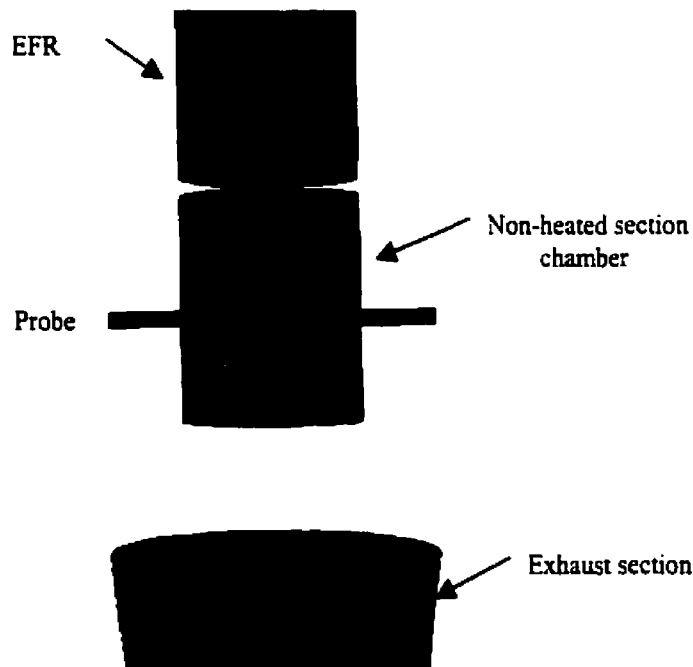


Figure 4.4 Computational grid shown on the surface of the geometry in non-heated section of the EFR

The governing fully three dimensional Navier-Stokes and energy equations were solved using a control volume approach as implemented by FluentTM over the computational

misalignments between the furnaces in the EFR. This feature of the reactor was taken into account in the model by adding uneven alignments between the tubes in the geometry as shown in Figure 4.5. At the flow inlet, the flue gas flow was assumed uniform with a velocity of 1.8 m/s since the flue gas exits the combustion chamber into the reactor through a honeycomb flow straightener.

Other modeling assumptions are listed below:

- To account for air entrained into the non-heated section from the surroundings, a zero gauge pressure boundary condition was used around this section.
- As described in Chapter 3, the flue gas pressure at the exit of the exhaust section was measured experimentally. In the model, the pressure of the gas at the exit of this section was set to the measured pressure.

The flue gas enters the heated section at a temperature of 800°C and it stays at this temperature in the heated section. However, in the non-heated section the gas cools down very rapidly due to the entrainment of the surrounding cooler air and radiation heat transfer from the surroundings. In this model, the P-1 radiation model accounts for the effect of radiation heat transfer on cooling the flue gas in the non-heated section. The P-1 radiation model is based on the expansion of the radiation intensity into an orthogonal series of spherical harmonics [16]. Some limitations of this model are; i) all surfaces are diffusive, ii) loss of accuracy for complex geometries, iii) model assumes gray radiation.

- The temperature of the chamber in the non-heated section is unknown. Using a conjugate heat transfer model, the conduction of heat through chamber coupled with

convective heat transfer in gas was computed considering the thermal conductivity of the chamber.

- The no-slip boundary condition was used at all wall surfaces.
- The flue gas properties were assumed to be those of air and the gas was assumed ideal. Specific heat capacity was assumed to be constant at 1007 J/kg-K, thermal conductivity was defined as a function of temperature using a piecewise-linear function, and viscosity was defined using the Sutherland's law.

The governing equations were solved using the segregated implicit steady solver in FluentTM 5.3. The SIMPLE algorithm was used for pressure-velocity coupling and the 2nd order accurate implicit scheme was used for the convection terms. To reach convergence faster, the following sequence of steps was followed. First, only the momentum equations were solved and calculations were done for isothermal flow. When the isothermal flow was well converged, the coupled energy and momentum equations were solved. The residuals were set to less than 10^{-6} and convergence was obtained after 16,000 iterations. All the simulations were run on a Pentium II 450 MHz processor with 512 Mb RAM and using the Windows NT operating system.

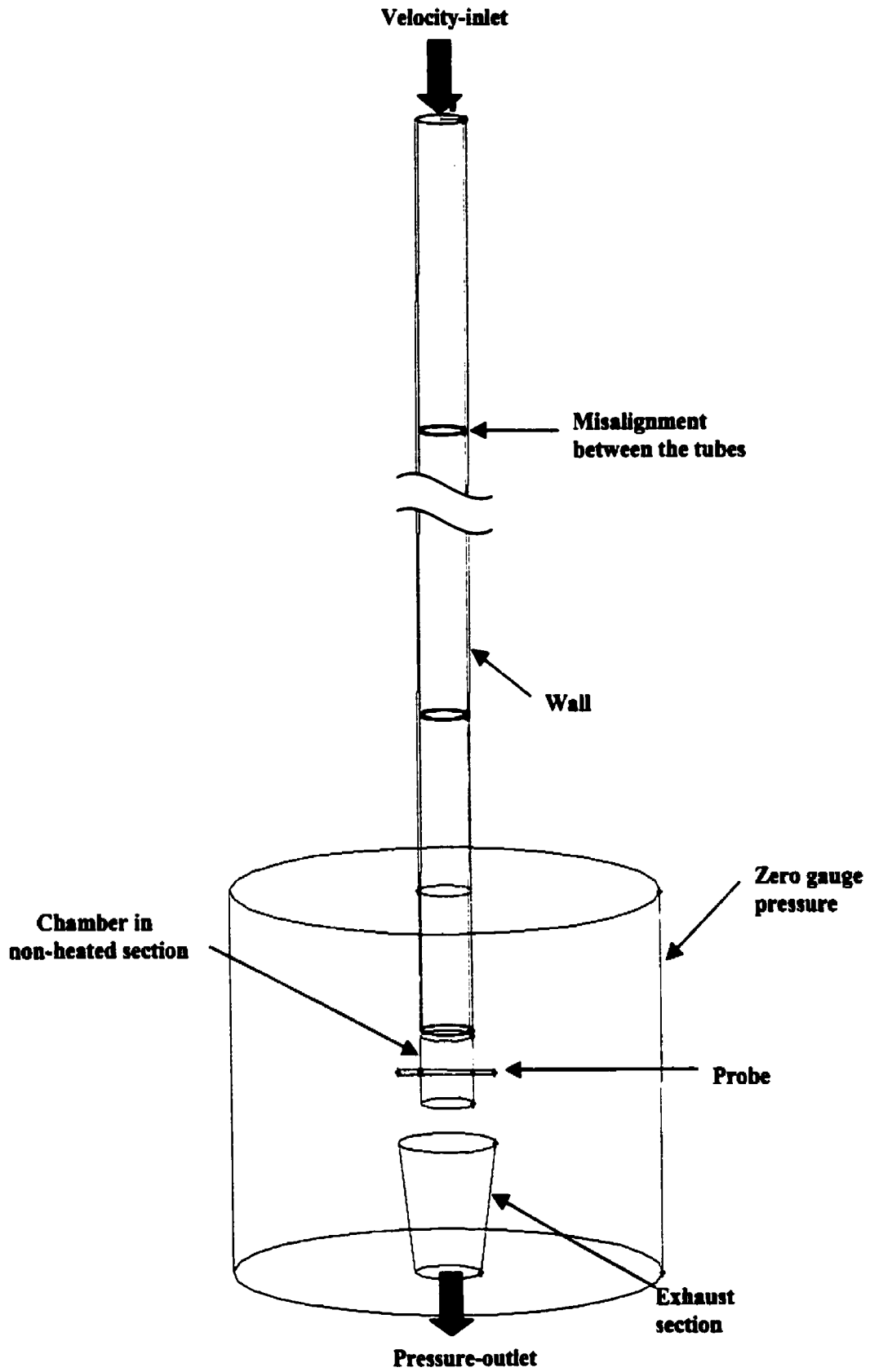


Figure 4.5 CFD boundary conditions of the EFR model

4.3.2 Particle Velocity and Temperature Estimations in the EFR

After solving the flow and temperature fields of the gas in the EFR, particles with different sizes of 90, 150, 260, 430, and 590 μm and composition of NaCl-Na₂SO₄ or NaCl-Na₂SO₄-K₂SO₄ were introduced to the model the length scale was set to $L_s = 0.001$ m. The initial conditions provided for the discrete phase calculation are particle starting position, velocity, temperature, and diameter. Particle trajectories, temperature, and liquid content were estimated using the algorithms described in section 4.2.1 and 4.2.2, respectively.

4.4 Numerical Model of a Simplified Upper Furnace

A simplified three-dimensional CFD model of recovery boiler upper furnace was developed to simulate particle temperature and liquid content in the superheater section of the boiler. The algorithms developed in sections 4.2.1 and 4.2.2 were used to estimate the trajectories and thermal condition of the particles in this model.

4.4.1 Flue Gas Velocity and Temperature Fields Simulation

The geometry of the boiler was created in GambitTM and it is shown in Figure 4.6a. The upper furnace of the boiler consists of three groups of parallel platens of tube bundles. The boiler bank and economizer were not included in the model to simplify the simulation. Only a small slice of the boiler needed to be modeled because of existing symmetrical planes. Due to the high aspect ratios and complexity of the geometry, an unstructured mesh was applied to the geometry. The mesh has 98,311 tetrahedral and hexahedral cells. Figure 4.6b shows the mesh generated for the boiler geometry.

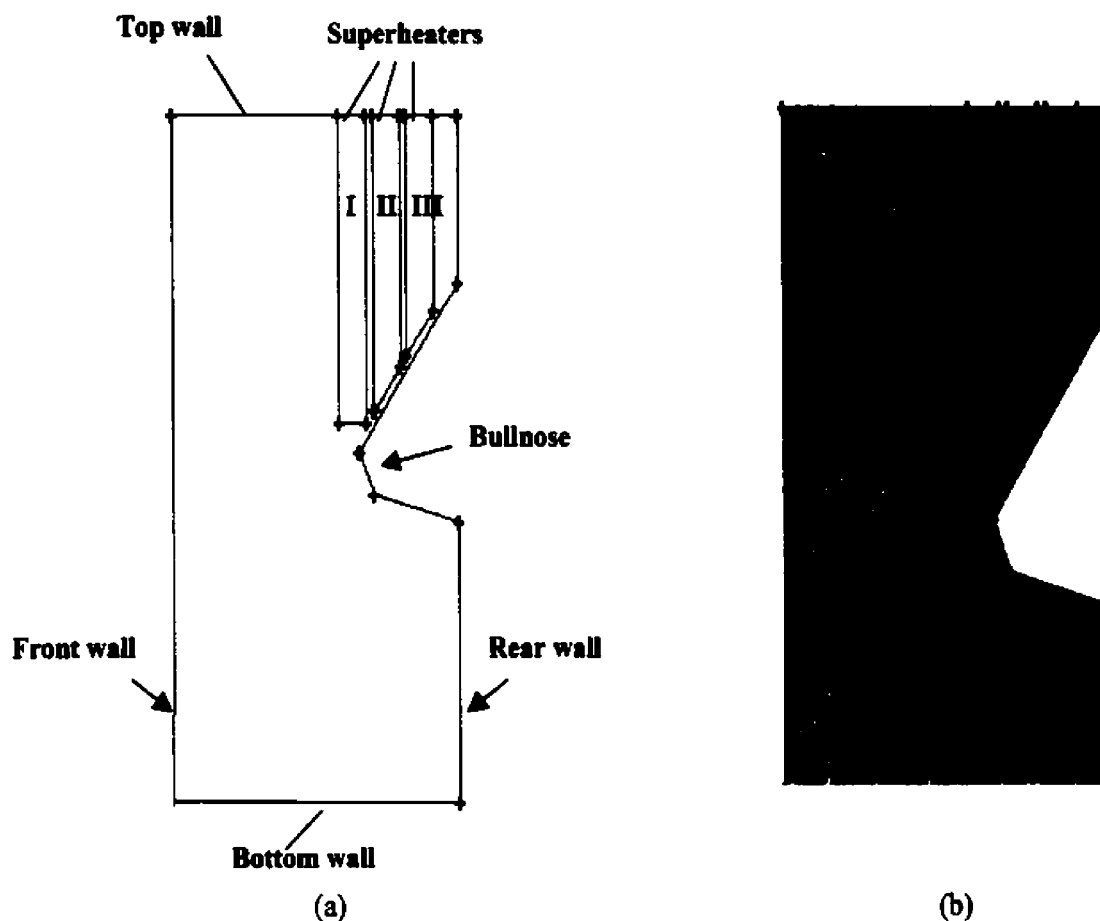


Figure 4.6 (a) The recovery boiler geometry, (b) computational grid generated for the boiler geometry

In this model, vapor of volatile substances and liquid and solid particles are assumed to have no effect on the gas flow. Also, this model does not include the black liquor combustion.

The flow in the boiler is highly turbulent thus a standard κ - ϵ model was used to simulate the turbulent flow. The κ - ϵ model is a semi-empirical model with two transport equations of turbulent kinetic energy and dissipation rate. In this model, the constants of the turbulent model was set to the following values:

$$C_{\epsilon} = 1.44, \quad C_{2\epsilon} = 1.92, \quad C_{\mu} = 0.09, \quad \sigma_k = 1, \quad \sigma_{\epsilon} = 1.3$$

Since a no-slip boundary condition was used at wall surfaces, the velocity gradients near the walls are very large. Therefore, a fine mesh is required near the walls to resolve the boundary layer. To avoid the computationally expensive mesh, a standard wall function was used to bridge the viscosity-affected region between the wall and the fully-turbulent region. Since thermal radiation plays a significant role in boiler heat transfer, a discrete ordinates method (DO) was used to account for radiation heat transfer in this model. In the discrete ordinates model, the spectral absorption and emission characteristics of the medium are divided into a discrete number of wavebands [16,15].

Boundary conditions were applied for turbulent flow and convective and radiative heat transfer on the surfaces and boiler inlet and outlet. The velocity and temperature of the gas entering the boiler were set to 3 m/s and 900°C. The turbulent intensity and turbulent length scale were defined as 10% and 0.02 *m* at the inlet of the flow. The temperature of the walls and tubes were defined considering two cases; i) clean recovery boiler, and ii) fouled recovery boiler. In both cases the temperature of the walls were set to 750°C. For clean boiler, the temperature of I, II, and III superheater tubes were respectively set to 500°C, 450°C, and 423°C. In the second case, deposits form on all heat transfer surfaces and therefore the surface temperature increases. As the deposit on the first platen grows thicker, the surface temperature increases and may reach the radical deformation temperature. At this point the deposit slags and stops growing [47]. At the radical deformation temperature, the liquid content of the deposit is 70%. Assuming that deposit has 10% mole Cl/(Na+K), and using the lever rule we can calculate the surface

temperature of the deposit to be 760°C. The surface temperatures of the deposits on the second and third platens are estimated from an energy balance at the deposit surface:

$$T_s = \frac{h_g T_g + \frac{T_{tube}}{\sum \frac{L}{k_D}}}{h_g + \frac{1}{\sum \frac{L}{k_D}}} \quad [4-26]$$

where h_g , T_g , L , and k_D are respectively the heat transfer coefficient of the gas, temperature of the gas, thickness of the deposit, and thermal conductivity of the deposit. Assuming that the deposit thickness is 5 cm, the surface temperature for second and third platens are respectively calculated to be 590°C and 561°C.

Zero pressure, velocity, and temperature gradients in the streamwise direction were assumed at the flow outlet. Also, the no-slip boundary condition was used for all the walls in the model. The surface absorptivity and emissivity on the furnace walls were based on results from the model developed by Wessel, Dension, and Samretvanich [53]. Figure 4.7 shows the CFD boundary conditions applied to the present recovery boiler model.

The flue gas properties were assumed to be the same as those of air.

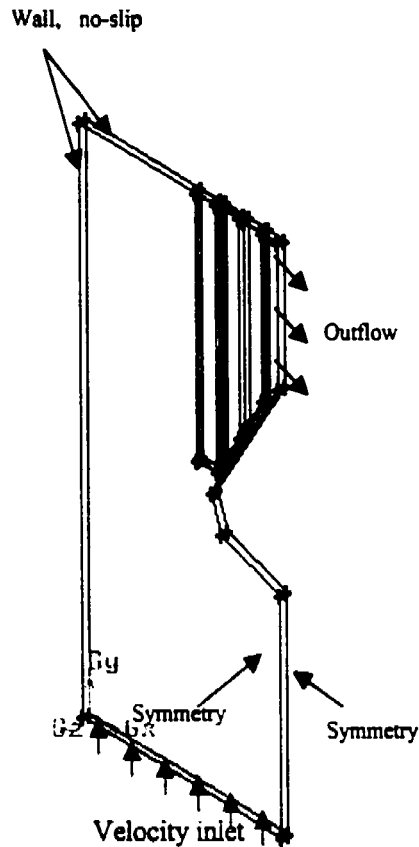


Figure 4.7 CFD velocity boundary conditions for the boiler model

The governing Navier-Stokes, energy, radiation, turbulence kinetic energy and dissipation transport equations were solved using a segregated implicit steady solver in FluentTM 5.3. The SIMPLE algorithm was used for pressure-velocity coupling. The 2nd order accurate implicit scheme was used for the convection term of the momentum equations. Convergence was obtained after 8,500 iterations and for residual convergence, criteria of 10^{-6} for the momentum equations and 10^{-8} for the energy equation. All the simulations were run on a Windows NT workstation, a Pentium II with 450 MHz processor and 512 Mb RAM.

4.4.2 Particle Trajectory and Temperature Estimations in the Upper Furnace

Once the flow and temperature fields of the gas in the upper furnace are solved, particles with different sizes of 90, 150, 260, 430, and 590 μm and composition of $\text{NaCl-Na}_2\text{SO}_4$ were introduced to the model. The initial conditions provided for the discrete phase calculation are particle starting position, velocity, temperature, and diameter. The initial velocity of all the particles were assumed to be the same, regardless of size. The assumptions made in the present study are as follows:

- Particle -particle interactions are negligible.
- The mean flow is a steady turbulent and incompressible flow.
- The effect of the molecular diffusion and the Brownian motion are negligible compare to turbulent dispersion.
- Particles have no impact on the flue gas. Therefore, an uncoupled approach was used, as described in section 4.2.1.

Solid particles are introduced to the model at an initial temperature of 27°C . Particles reach the gas temperature and are completely molten when they enter the superheater section. In this model, the distance from the entrance of the flow to the upper part of the boiler is long enough for particles to be completely molten when they enter the superheater section. The algorithms used to predict particle trajectories, temperature, and liquid content were described previously in chapter in section 4.2.1 and 4.2.2, respectively.

5. Results and Discussion

In this chapter, the results of the EFR and boiler upper furnace model are presented and discussed. Section 5.1 presents the results for the EFR temperature and velocity profiles and particle velocity and temperature results. In section 5.2, the results for the recovery boiler model and particle temperature and liquid content simulations in the superheater section of the boiler are presented.

5.1 Validation of the Entrained Flow Reactor Model

The gas flow field inside the reactor and in the non-heated section was validated before introducing the particles to the model. The sensitivity of the results to numerical parameters such as density of the grid and the residual level of variables was tested to minimize numerical errors. Also, predicted results at representative test positions were compared with experimental data to ensure the developed model is consistent with experimental results.

5.1.1 Sensitivity of the Results to Numerical Parameters

To minimize the discretization and iterative errors, a grid independence test and a convergence test were performed. Grid independence means that the converged solution is independent of the grid density. The influence of mesh refinement was examined using three unstructured grids with 309,000 (MS1), 390,000 (MS2), and 600,000 (MS3)

tetrahedral and hexahedral cells. Figure 5.1 shows a comparison of the gas velocities along the EFR centreline. Grid independence is indicated when further mesh refinement yields only small and insignificant changes in the numerical solution. The comparison between MS2 and MS3 indicates that there is a negligible difference between the results although the refined mesh (MS3) is almost twice as large as the coarse mesh (MS2). Since the finest mesh, MS3, requires higher memory and more time to converge, the 390,000 cell mesh, MS2, was used for all simulations.

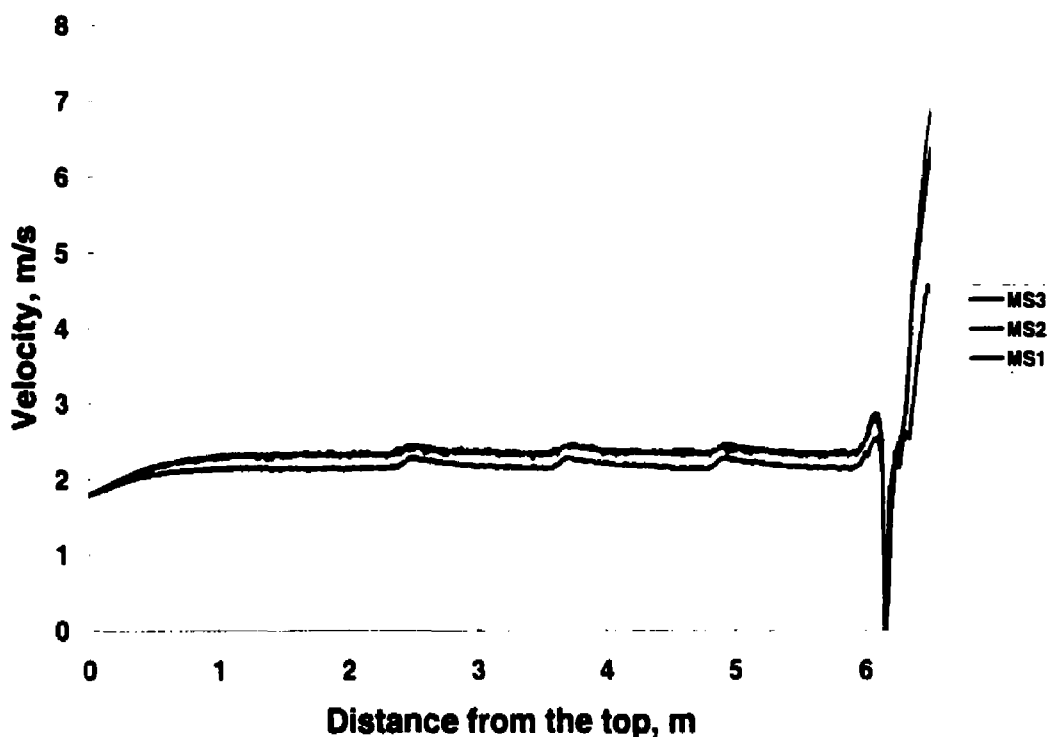


Figure 5.1 Comparison of the influence of mesh density on gas velocity along the centre of the EFR, MS1-309,000, MS2-390,000, and MS3-600,000 cells

To test for convergence, the residual level of each variable was monitored. At the end of each solver iteration, the residual sum for each of the conserved variables is computed and stored. The solution is normally considered converged when residuals for all

variables fall below 10^{-3} . However, in some problems this value is not sufficient for full convergence and thus one method to judge convergence is to drop the residuals by three orders of magnitude. In the present work, the convergence criterion was reduced to 10^{-6} .

5.1.2 Flue Gas Velocity and Temperature

The gas flow field was estimated in the reactor and in the non-heated section assuming a uniform gas inlet velocity and an average inlet temperature of 1.8 m/s and 800°C, respectively. The flue gas entered the EFR at a uniform velocity and the flow started to develop as it moved down the reactor. However, as discussed before, the misalignments between the furnaces disrupts the boundary layers. The gas velocity profile remained almost uniform throughout the reactor with a velocity close to 2 m/s. In the non-heated section, air was entrained into the exhaust section from the surroundings due to the suction of the fan located at the end of this section. Figure 5.2 shows the entrained air in the non-heated section. A closer examination of the velocity profile shows that although the cross-sectional area of the non-heated section chamber and the exhaust section are larger than the EFR, the flow starts to accelerate as it enters these sections. The large amount of air that is entrained into these sections decreases the cross-sectional area of the core flow causing the flow to accelerate at the entrance of both sections.



Figure 5.2 Entrained air and gas velocity vectors (m/s) in the non-heated section

An accurate simulation of the gas velocity in the non-heated section and close to the probe is of great importance since small particles follow the flue gas streamlines and their velocity is the same as the gas velocity. Figure 5.3 shows the gas velocity vectors in the non-heated section of the EFR and over the probe. The length of the vectors are proportional to gas velocity magnitude. As shown in Figure 5.3, the flue gas flow is brought to rest at the stagnation point and underneath the probe, separation and recirculation of the flow occur. The position of the separation point is strongly influenced by the Reynolds number. For laminar flows separation occurs at $\theta \approx 80^\circ$ (θ is the angle between two radii of the tube, one connected to stagnation point and one connected to separation point).

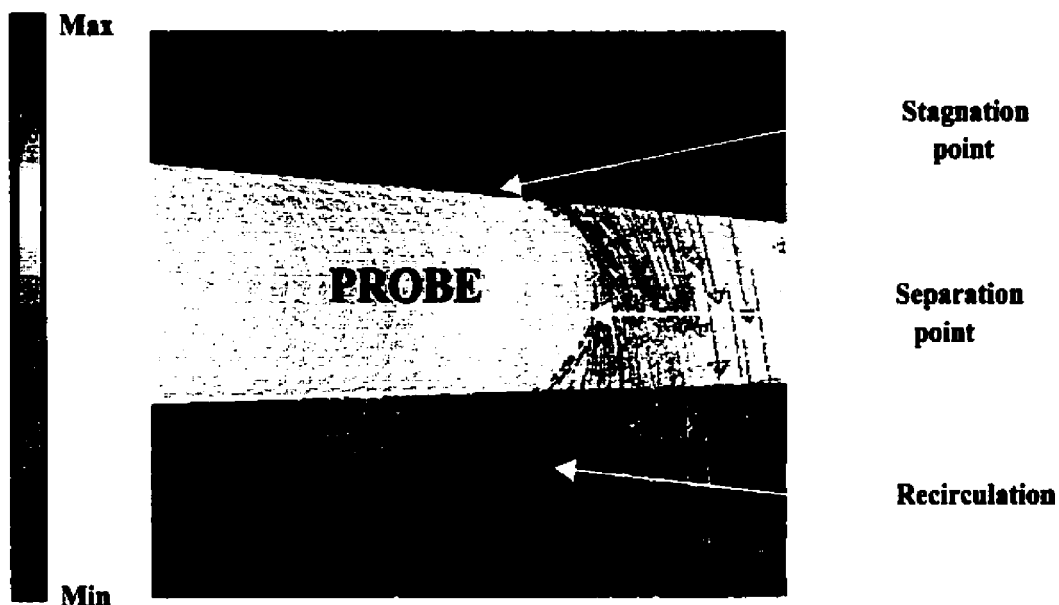


Figure 5.3 Gas velocity vectors (m/s) over the probe

The velocity profile at the exit of the reactor was determined experimentally by Naseri [32]. Small particles with a median size of 120 μm were fed to the reactor and their velocity was measured 2 *cm* above the probe. Figure 5.4 shows a comparison of the measured and calculated gas velocity 2 *cm* above the probe. Particles of this size have a very low Stokes number and therefore their velocity is within $\pm 5\%$ of the gas velocity [32]. The results show that the model predicts a flat central velocity profile similar to the experimental results but at a moderately higher velocity (10%). The EFR is not well rounded and other misalignments in the reactor that were not considered in the model may account for the overprediction of the central velocity.

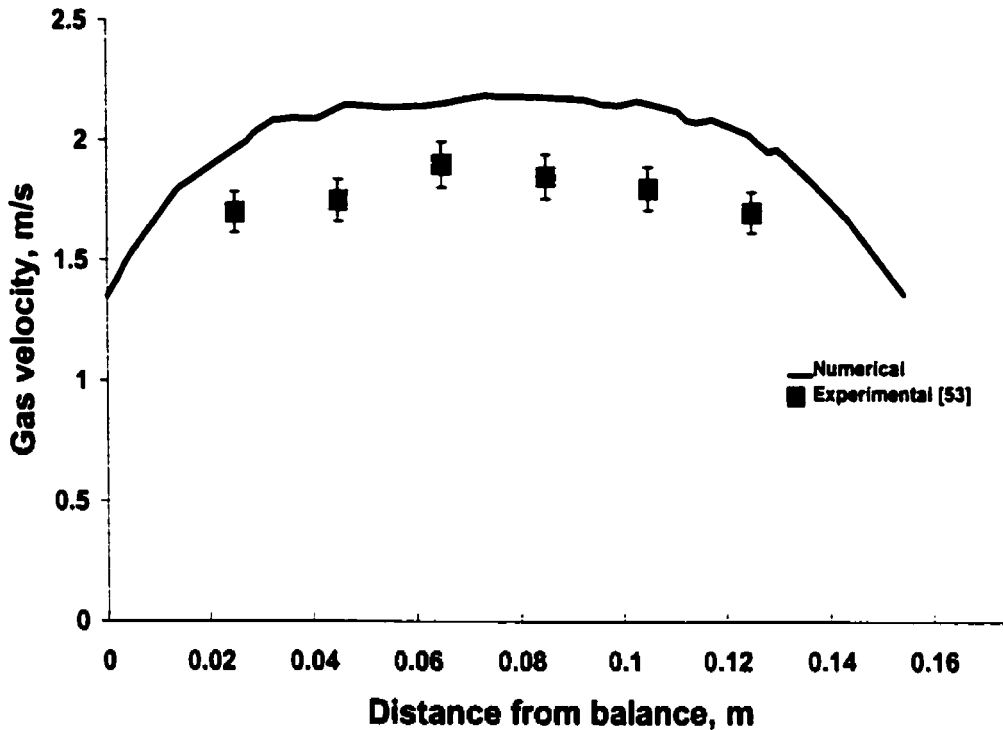


Figure 5.4 Predicted and measured velocity profiles 2 cm above the probe

The contours of the temperature magnitude along the centre plane are shown in Figures 5.5 and 5.6. The gas temperature through the EFR is at the inlet gas and EFR wall temperature of 800°C. However, as the gas enters the non-heated section the entrained air from the surroundings and radiation heat transfer to the surroundings greatly cools down the gas temperature. The entrained air enters the non-heated chamber from gaps between the exit of the reactor and the chamber. Although the temperature of the surrounding air was set to 27°C, its effect on decreasing the gas temperature was small compare to the radiation effect. As shown in Figure 5.5, the air entrained into the chamber did not mix with the flow at the centre and moved down along the sidewalls.

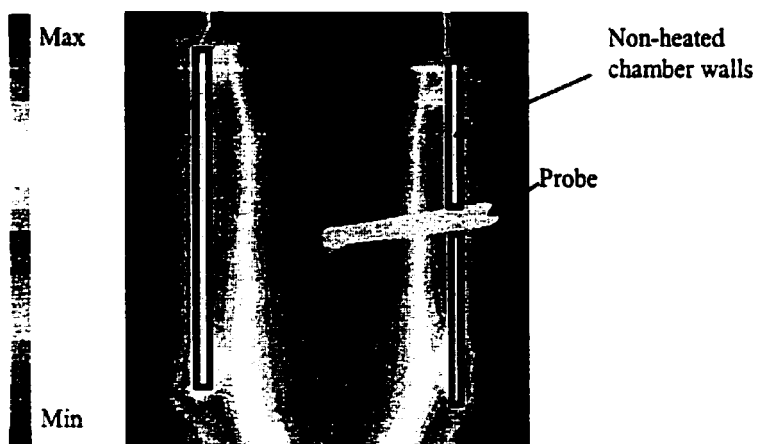


Figure 5.5 Gas temperature contours in the non-heated section without considering radiation

To obtain a more realistic temperature field in the non-heated section, a P-1 radiation model was used. Including radiation heat transfer in the model decreased the gas temperature dramatically as is shown in Figure 5.6.

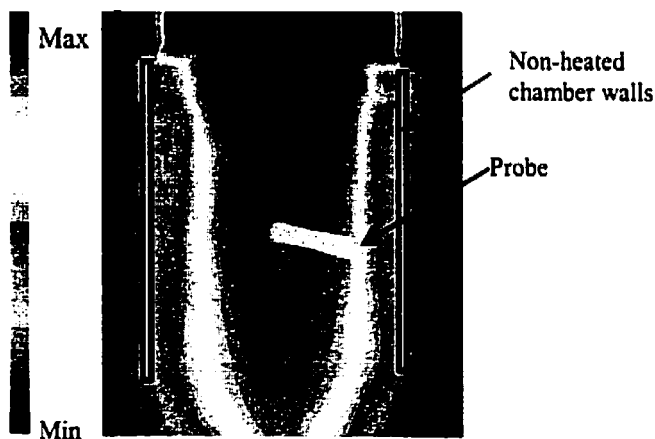


Figure 5.6 Gas temperature contours in the non-heated section considering a P-1 radiation model

A comparison between the calculated and measured temperature at the exit of the reactor is shown in Figure 5.7. The gas temperature was measured using a pyrometer at the exit of the reactor and in the non-heated section. It is observed that the exit temperature is overpredicted (less than 1%). A higher temperature is consistent with an overprediction of the core velocity. The predicted gas temperature at the exit of the EFR is lower than 800 °C because of radiative heat transfer with the non-heated section.

As discussed earlier, to properly predict the temperature of the chamber in the non-heated section, a conjugate heat transfer model was used to account for the conduction of heat through the chamber wall coupled with the convective and radiative heat transfer to the gas. The chamber temperature was calculated to be about 650°C which is in agreement with experimental measurements.

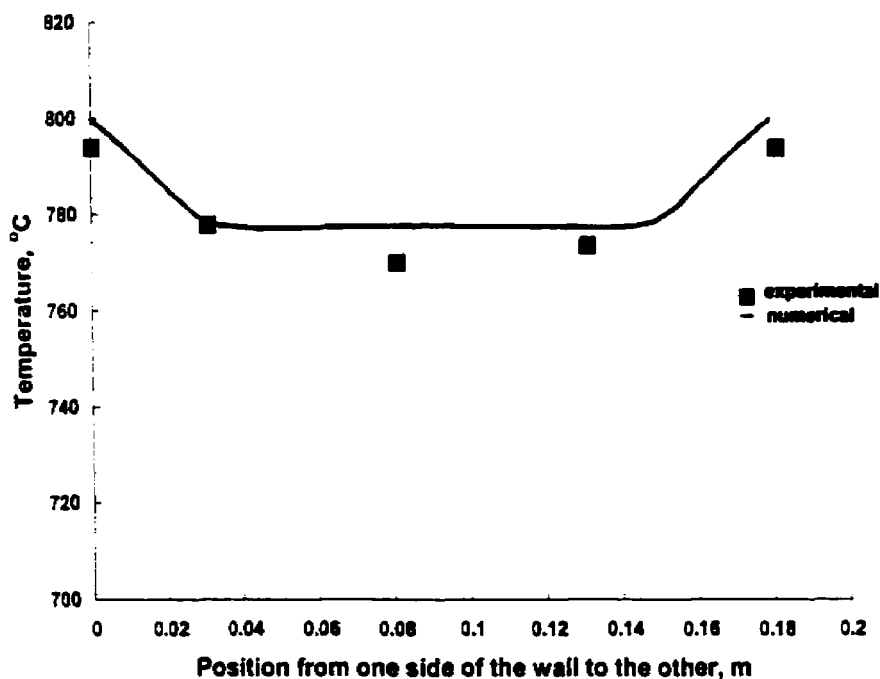


Figure 5.7 Predicted (P-1 model) and experimented gas temperature profiles at the exit of the reactor

The predicted results are in good agreement with the experimental data. The well-substantiated EFR gas velocity and temperature profiles provide a basis for the development of a particle velocity, temperature, and liquid content prediction algorithm.

5.1.3 Particle Impact Velocity

Particle trajectories were estimated as the particles traveled down the reactor and through the non-heated section until their impact on the probe. Figure 5.8 shows the particle impact velocity on the probe as a function of particle size. Since particles fall by gravity in the EFR, an increase in particle size results in an increase in particle impact velocity. When a particle reaches its terminal velocity, the drag force which is proportional to the square of particle diameter is balanced by gravity which is proportional to the diameter cubed. Since most particles reach their terminal velocity in the EFR, there is a linear correlation between particle velocity and particle size as shown in Figure 5.8. The predicted results are in good agreement with the experimental data of Naseri [32].

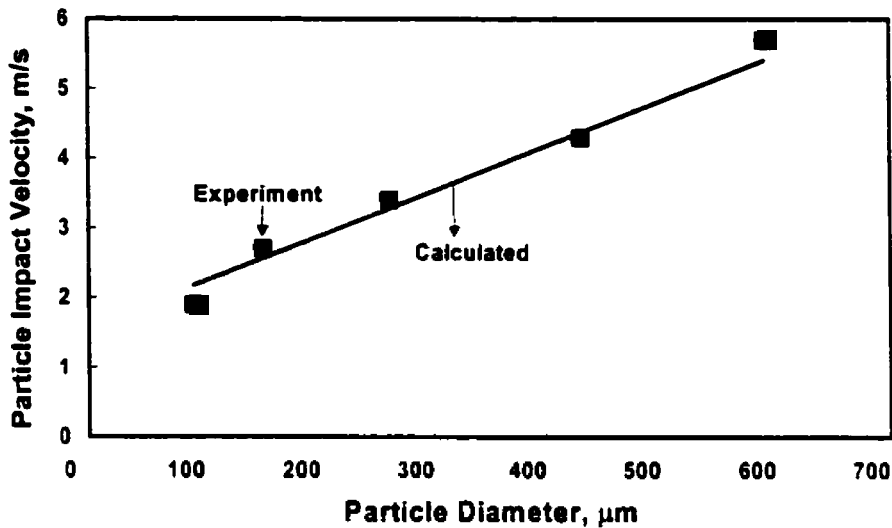


Figure 5.8 Predicted particle impact velocity on EFR probe versus experimental data of Naseri [32], 10 mole% Cl/(Na+K) and 0 mole% K/(Na+K), shape factor=1.0

Previous studies [32] have shown that particle composition, especially chloride content, has an effect on the particle velocity. In previous particle velocity estimations, it was assumed that a particle's outer layer is completely molten and therefore the particle has a spherical shape. As a result the calculated drag force was based on spherical particles. In the EFR, this assumption is true for small particles containing 5 to 10 mole% Cl/(Na+K) since they contain enough liquid phase to form a spherical shape particle. However, particles with lower chloride content remain solid and retain their irregular shape longer resulting in a higher drag force thus lower velocity. Particle temperature and liquid content estimation, discussed in the next section, shows that particles larger than 260 μm that contain low chloride contents retain their irregular shape and do not reach the

complete melting temperature in the reactor. This is not unexpected since as the chloride content decreases the complete melting temperature increases. For example reducing the chloride content from 10 to 2 mole% $Cl/(Na+K)$ increases the complete melting temperature from 800 to 855°C and particles can not reach this temperature since the maximum temperature in the EFR is 800°C. To account for the irregular shape of the particles, an assumed shape factor of 0.8 was applied to particles larger than 260 μm containing 2 mole% $Cl/(Na+K)$ and 0 mole% $K/(Na+K)$ [20]. The resulting particle impact velocity predictions are in excellent agreement with the experimental data of Naseri [32] as shown in Figure 5.9.

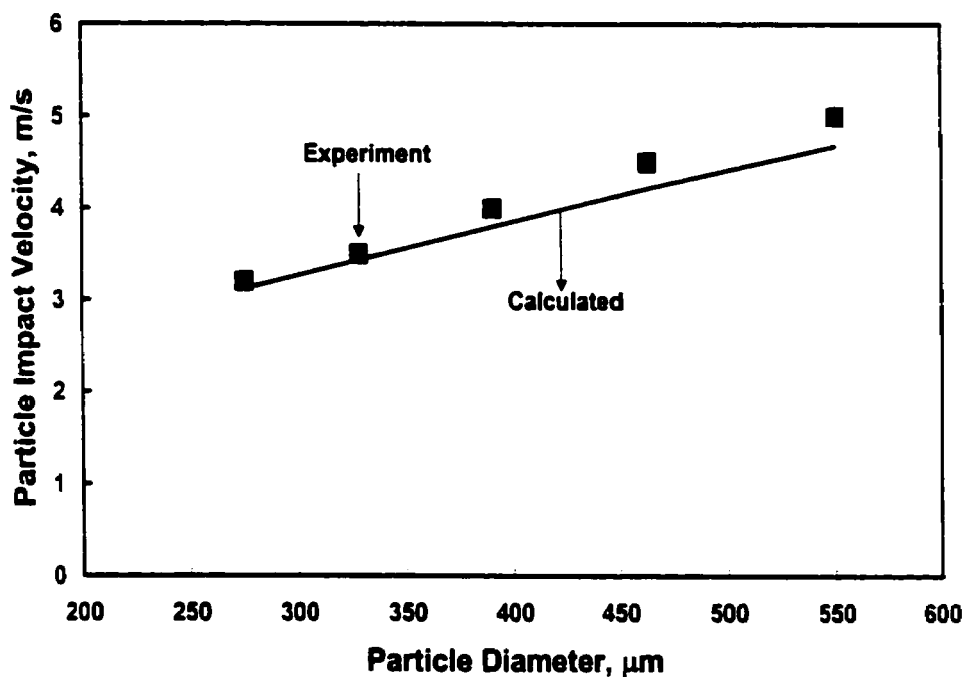


Figure 5.9 Predicted particle impact velocity on EFR probe versus experimental data of Naseri [32], 2 mole% $Cl/(Na+K)$ and 0 mole% $K/(Na+K)$, shape factor=0.8

5.1.4 Particle Temperature and Liquid Content

The temperature and liquid content of the particles with different sizes were estimated as they traveled down the reactor using the algorithm developed in Chapter 4. Figures 5.10 and 5.11 show the estimated temperature and liquid content of the particles containing 10 mole% Cl/(Na+K) and 0 mole% K/(Na+K) based on the lever rule as they travel through the reactor and non-heated section.

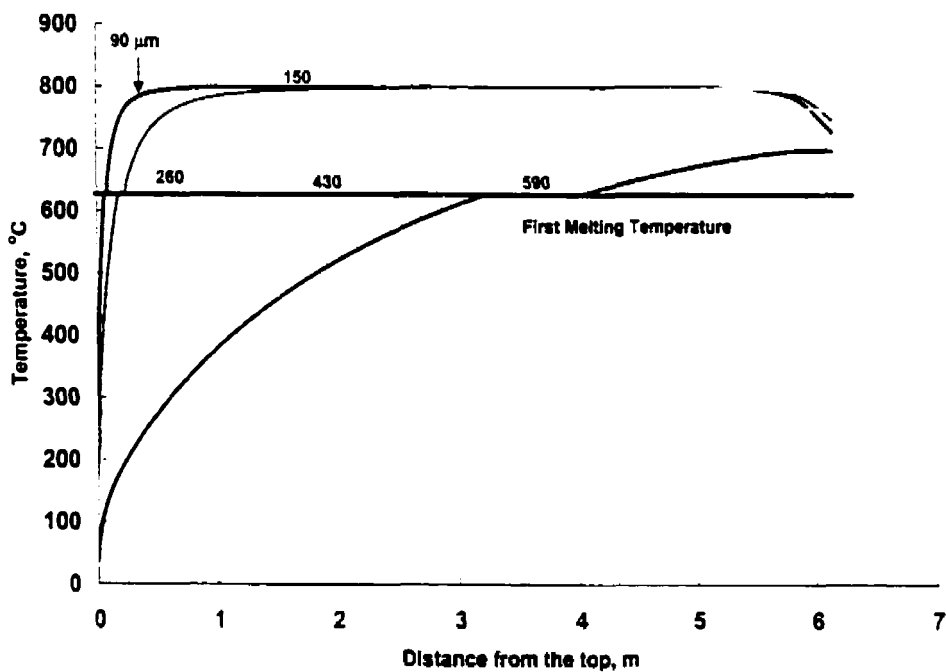


Figure 5.10 Estimated temperature for particles containing 10 mole% Cl/(Na+K) and 0 mole% K/(Na+K)

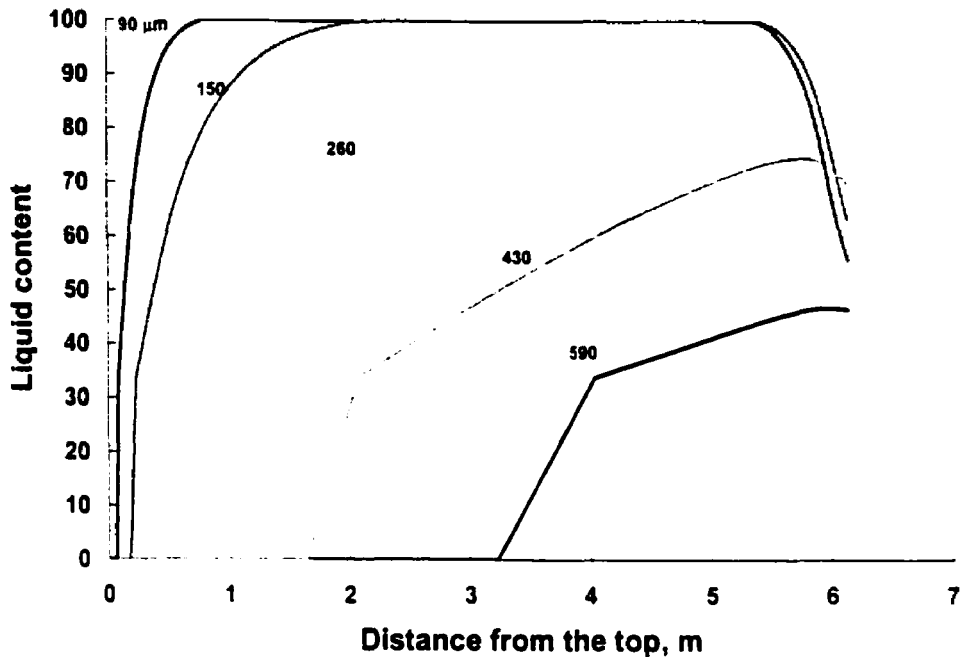


Figure 5.11 Estimated liquid content for particles containing 10 mole% $\text{Cl}/(\text{Na}+\text{K})$ and 0 mole% $\text{K}/(\text{Na}+\text{K})$

The smallest particles quickly reach the first melting temperature (FMT), complete melting temperature (CMT) and the temperature of the carrier gas as they travel down the EFR. However, the largest particles (430 and 590 μm) do not reach the CMT prior to exit from the EFR due to their higher mass. As the particles exit the EFR into the non-heated section, they begin to cool. The smaller particles cool more rapidly than larger particles, resulting in the 90 and 150 μm particles having lower temperatures and liquid contents than 260 and 430 μm particles upon impact on the probe. These results are consistent with experimental data of Shenassa [41] where it was observed that adhesion efficiency increased with increasing particle size. Smaller particles cool faster than larger

ones in the non-heated section and thus they do not have sufficient liquid content to stick to the probe.

As discussed in Chapter 4, two methods were introduced to estimate the particle liquid content, the lever rule and thermodynamic data. In the present study, the thermodynamic data were used to estimate the temperature and liquid content of the particles with the composition of $\text{Na}_2\text{SO}_4\text{-NaCl-K}_2\text{SO}_4$. To ensure the results obtained from the thermodynamic data are reliable, the temperature of particles containing 10 mole% $\text{Cl}/(\text{Na}+\text{K})$ and 0 mole% $\text{K}/(\text{Na}+\text{K})$ were also predicted using the lever rule. The comparison between the two methods, shown in Figure 5.12, indicates that both methods can be used in the model to calculate the particle liquid content. Further comparisons at different compositions and particle sizes confirm this conclusion.

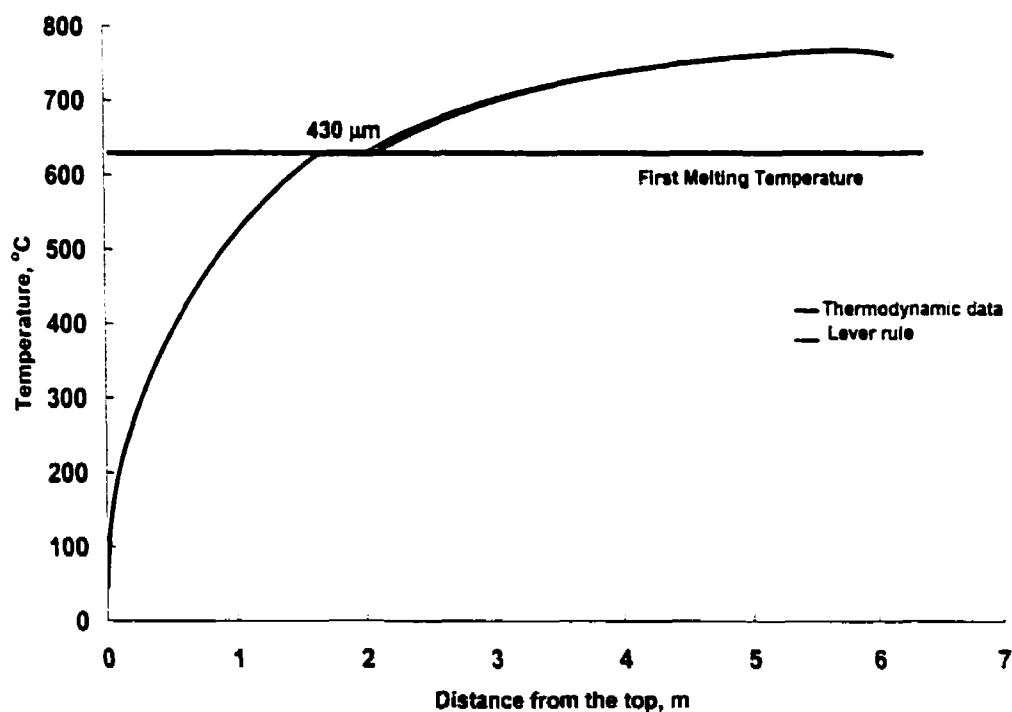


Figure 5.12 Estimated particle temperature using the lever rule and thermodynamic data, 10 mole% $\text{Cl}/(\text{Na}+\text{K})$ and 0 mole% $\text{K}/(\text{Na}+\text{K})$, $430\ \mu\text{m}$

Particle composition, particularly chloride content, has a significant effect on the particle temperature and liquid content. Figures 5.13 and 5.14 show the predicted temperature and liquid content of 260 μm particles at different chloride contents as they travel down the reactor. Particles may pass through four temperature stages as they descend through the EFR. In the first stage, particles of the same size but different chloride content increase in temperature and reach the FMT at almost the same position since FMT is only weakly dependent on the chloride content. In the second stage, energy absorbed by particles is used to melt and increase the temperature of the particles. The proportion of energy used to melt particles increases with chloride content and consequently lower chloride content particles increase in temperature more rapidly. In the third temperature stage, the particle reaches the CMT and then increases more rapidly in temperature until it approaches the EFR wall temperature. For the case of the 260 μm particles, the CMT was reached for only the 20 mole% Cl/(Na+K) and 0 mole% K/(Na+K) case; at all lower chloride content cases their CMT was higher than the EFR temperature. Once the particle temperature reaches the EFR temperature the fourth stage is reached and the temperature remains constant.

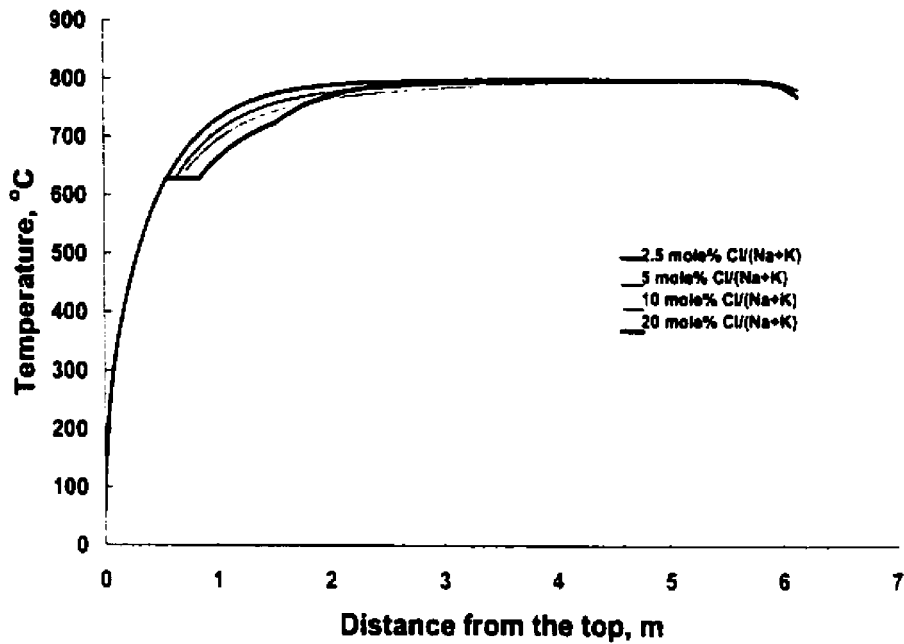


Figure 5.13 Estimated temperature for particles containing different chloride contents, 260 μm particle size

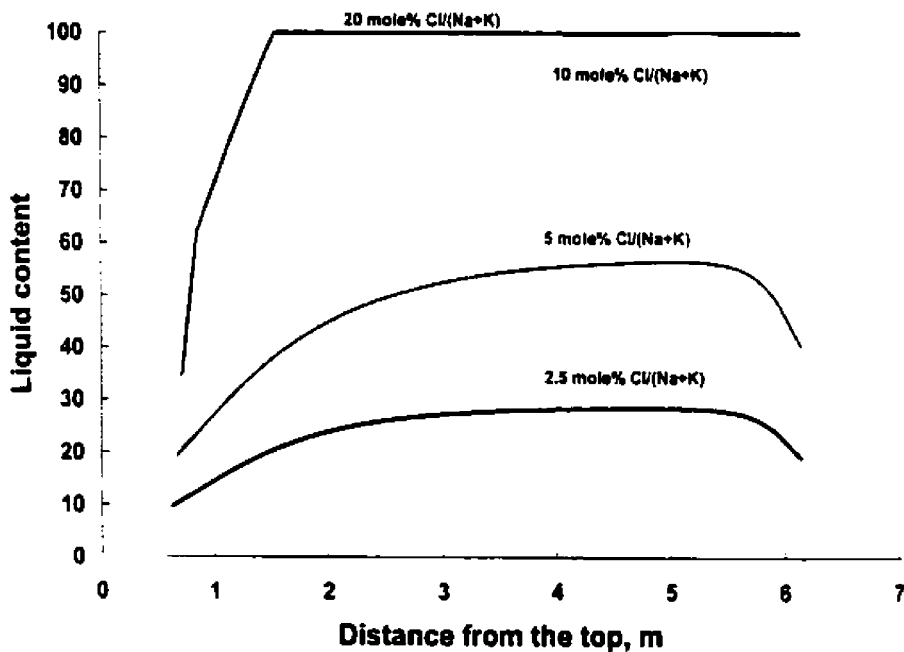


Figure 5.14 Estimated liquid content for particles containing different chloride contents, 260 μm particle size

Figure 5.15 shows the predicted temperature and liquid content of 590 μm particles for different chloride contents. These particles are too large to reach the CMT in the reactor and they are all partially molten at the probe. Therefore as discussed previously, particles with higher chloride content have lower temperature and higher liquid content at the same position in the EFR.

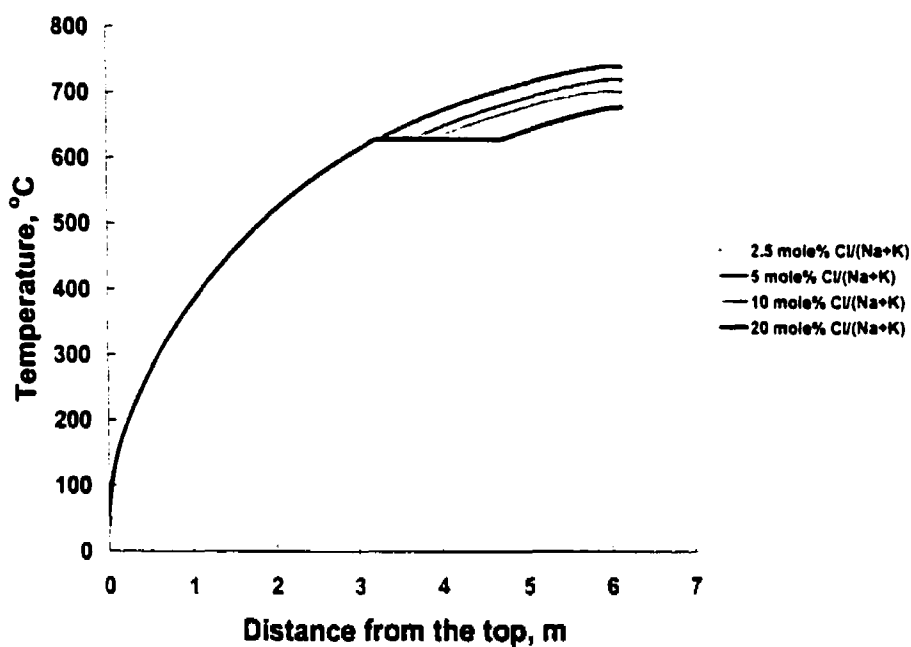


Figure 5.15 Estimated temperature for particles containing different chloride contents, 590 μm particle size

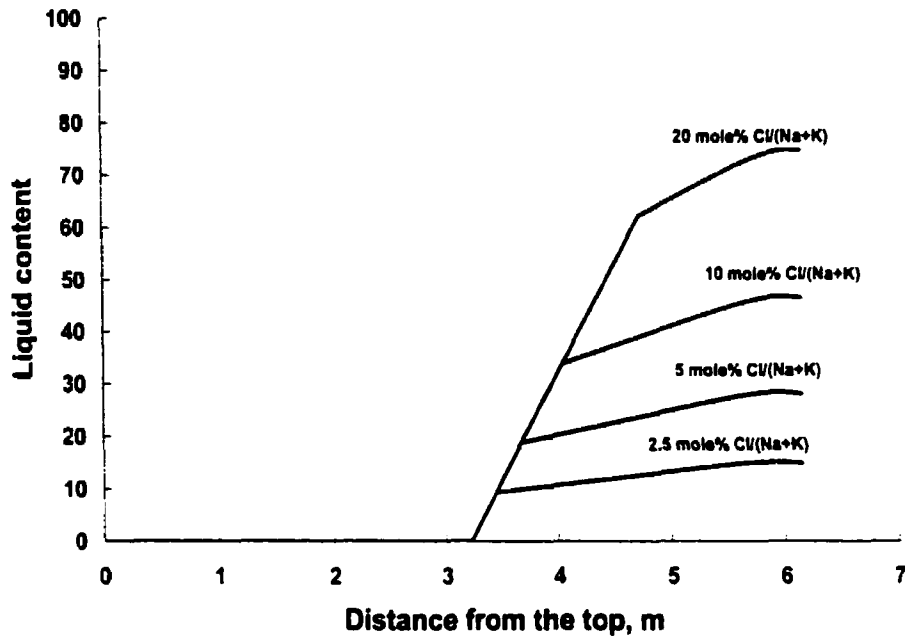


Figure 5.16 Estimated liquid content for particles containing different chloride contents, 590 μm particle size

Figures 5.14 and 5.16 show that particles containing 2.5 mole% Cl/(Na+K) and 0 mole% K/(Na+K) have the minimum liquid content, i.e. 15%, required to deposit on a surface. By increasing the chloride content, the liquid content of the particle is increased. For particles with more than 10 mole% Cl/(Na+K) and 0 mole% K/(Na+K) the calculated liquid content is higher than 70% indicating that the deposit formed by these particles will likely run off vertical heat transfer surfaces. This is consistent with the experimental data of Shenassa [42] where it was observed that deposition of the particles on the probe in the EFR begins at a critical chloride level of 2.5 mole% Cl/(Na+K) and 0 mole% K/(Na+K) and increases with increasing the chloride content up to 10 mole% Cl/(Na+K). The deposition rate remained constant at chloride concentrations above 10 mole% Cl/(Na+K).

Potassium is known to decrease the FMT of the particles thus affecting the particle temperature and liquid content. Figures 5.17 and 5.18 show the predicted particle temperature and liquid content variations through the EFR for a particle containing 10 mole% Cl/(Na+K) and 5 mole % K/(Na+K).

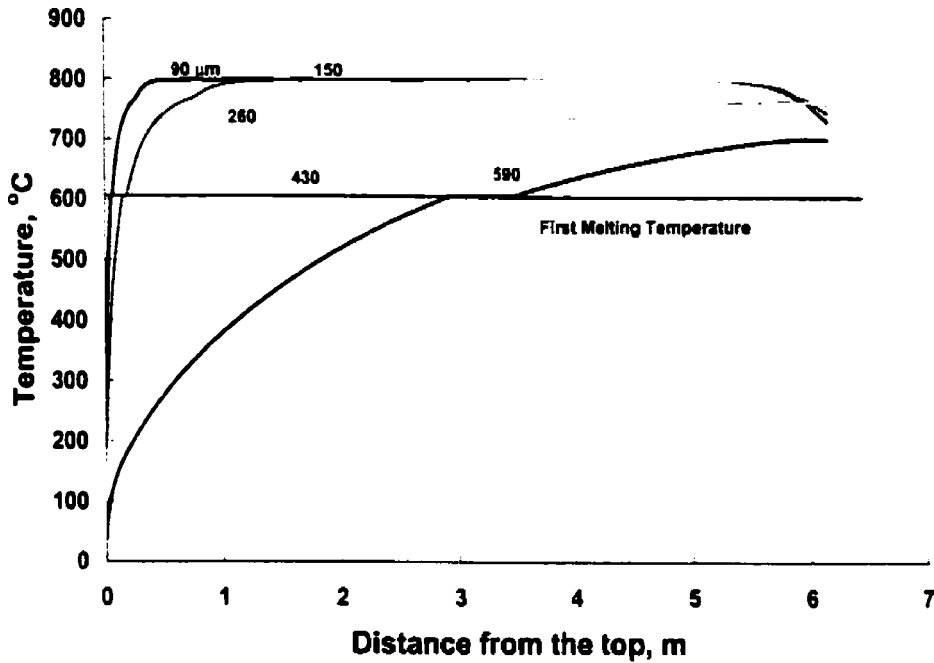


Figure 5.17 Estimated temperature for particles containing 10 mole% Cl/(Na+K) and 5 mole% K/(Na+K)

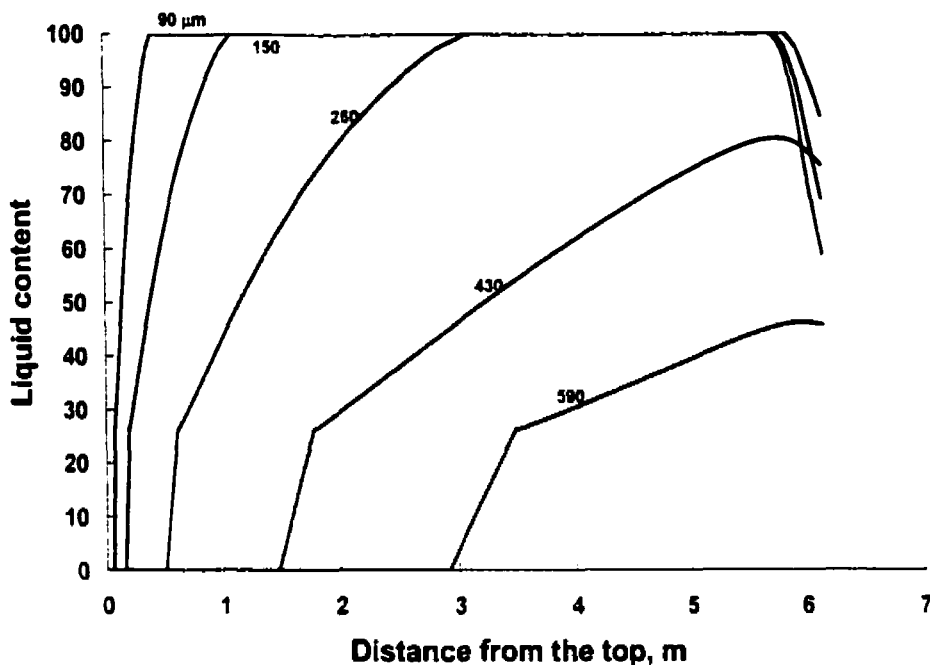


Figure 5.18 Estimated liquid content for particles containing 10 mole% Cl/(Na+K) and 5 mole% K/(Na+K)

A comparison of Figures 5.10 and 5.17 indicates that as potassium content is increased from 0 to 5 mole% K/(Na+K) the first melting temperature of the particles decreases from 628°C to 600°C. Although particles containing potassium reached their FMT faster than particles with no potassium, there is only a small difference between the particle temperatures and liquid contents throughout the EFR non-heated section. A comparison of the liquid content results, Figures 5.11 and 5.18, similarly shows a close agreement. This is consistent with the experimental results of Rezvani [37] suggesting that at a chloride content higher than 5 mole% Cl/(Na+K), potassium has only a small effect on the deposition rate.

5.1.5 Summary

The liquid content of a particle plays a significant role in determining the rate of deposition. A particle tracking algorithm was developed and substantiated with experimental data to estimate synthetic carryover velocity, temperature, and liquid content as the particles travel down the reactor. The algorithm was extended to potassium containing particles and particle deposition was investigated as a function of liquid content, size, and velocity. The good agreement between the predicted results and experimental data indicates that the methodology can be extended to predicting the particles, thermal conditions in a simplified model of a recovery boiler upper furnace.

5.2 Validation of the Recovery Boiler Upper Furnace Model

The turbulence model of the simplified upper furnace was evaluated before introducing the particles into the simulated flow. The sensitivity of the results to the grid density was studied to ensure that the results are grid independent.

5.2.1 Sensitivity of the Results to Numerical Parameters

Three unstructured grids with 71,517 (MS1), 98,311 (MS2), and 114,334 (MS3) cells were used to examine the influence of mesh refinement on the results. Figure 5.19 shows a comparison of the gas velocity along the furnace centreline computed on three grids using a standard $\kappa - \epsilon$ model. For comparison purposes the bottom of the upper furnace is defined as the bottom of the upper furnace model shown in Figure 4.6a.

The comparison shows that refinement of the mesh had a negligible effect on the predicted gas velocity and that the results show grid independence. Other comparison regions also showed similar agreement. Therefore, for all the simulations the 98,311 cell mesh (MS2) was used.

To test for full convergence the residuals of all variables were monitored. In this case, the residual level was lowered to 10^{-6} for the momentum equations and 10^{-7} for the energy equation.

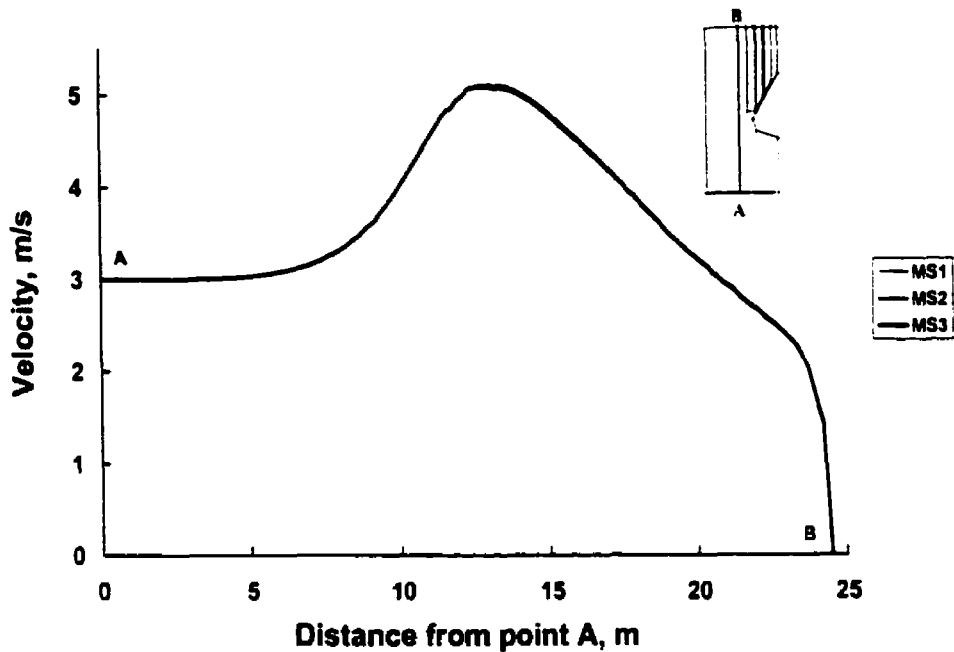


Figure 5.19 Influence of the mesh density on the gas velocity at the centre of the upper furnace MS1-71,517, MS2-98,311, and MS3-114,334

5.2.2 Flue Gas Velocity and Temperature

The flue gas enters the upper furnace with a uniform velocity and average temperature of 3 m/s and 900 °C. The turbulent intensity and length scale were set to 10% and 0.02 m at the inlet of the flow. The gas velocity vectors on the central vertical plane are shown in Figure 5.20; the length of the arrows indicates velocity magnitude. The gas flows upwards accelerating past the bullnose, separates after the bullnose and then begins to turn towards the exit of the upper furnace. Recirculation zones form above the bullnose due to flow separation and at the corners of the boiler. The predicted flow pattern is similar to the results presented in literature [53,54,40].

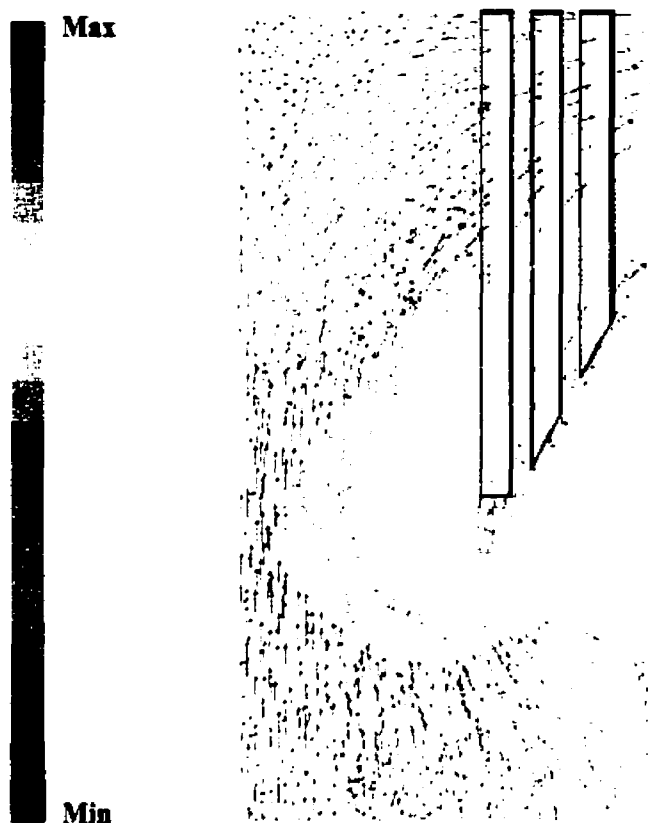


Figure 5.20 Gas velocity vectors on the central vertical plane (m/s)

Figure 5.21 shows the gas temperature contours on the central vertical plane. The gas temperature distribution is significantly influenced by the gas velocity. The high gas velocity on the left side of the bullnose resulted in a locally high temperature region. Also, the temperature of the gas in the recirculation zone is decreased since it is a relatively low velocity region close to a concentration of heat transfer surfaces, i.e. the superheater tubes. As gas enters the superheater section, its temperature decreases significantly due to convective and radiative heat transfer.

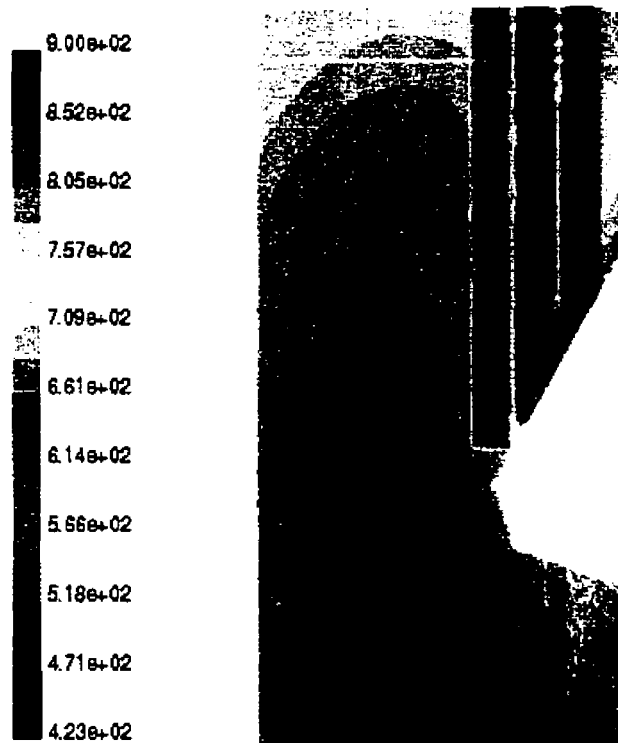


Figure 5.21 Gas temperature contours on the central plane (°C)

The predicted average temperature of the gas at a horizontal plane above the bullnose was compared with measured values in literature [53]. The predicted value is approximately 850 °C which is within normal operating range. The difference between the predicted and measured temperature values are small and may be due to the following modeling assumptions:

- The effect of radiative heat transfer from char bed is neglected;
- Black liquor combustion model was not considered in this model resulting in a lower gas temperature [54];
- The effect of carryover and fume deposits on radiative heat transfer are neglected.

The predicted flow and temperature fields in the upper furnace of the boiler are similar to those reported in literature. Therefore, the simplified upper furnace model can be used to predict particle temperature and liquid content trends in convection section.

5.2.3 Particle Temperature and Liquid Content

A stochastic particle dispersion model was used to account for the effect of turbulence on the motion of the particles. Particles were introduced to the model at positions located at the inlet plane along a line centred between the front wall and the rear wall. At each point 500 particles were tracked to account for the random effects of turbulence on the particle dispersion, see Figure 5.22. Figure 5.23 provides an expanded view of the trajectory of 150 and 590 μm particles fed to the reactor from two positions, close to the front wall and close to the rear wall. Only 20 representative particle trajectories are plotted of the 500 that were calculated for each particle. As expected, the 150 μm particles on average follow the mean flow path but disperse about this mean path. Small particles disperse more than the large particles since they follow more closely the instantaneous motion of the flue gas. Therefore, the particles distribute uniformly over the full length of the superheater tubes except for the recirculation zone. Some deposition is expected in the recirculation region but at a much lower rate. The 590 μm particles deviate from the flue gas motion due to inertia and they dominantly move toward the top wall and upper portion of superheater platens with some particles entering the recirculation zone at the corner of the boiler. These results suggest that small particles will deposit on the superheater uniformly across the height of the superheater except in

the recirculation region and large particles will preferentially deposit on the upper half of the tubes.

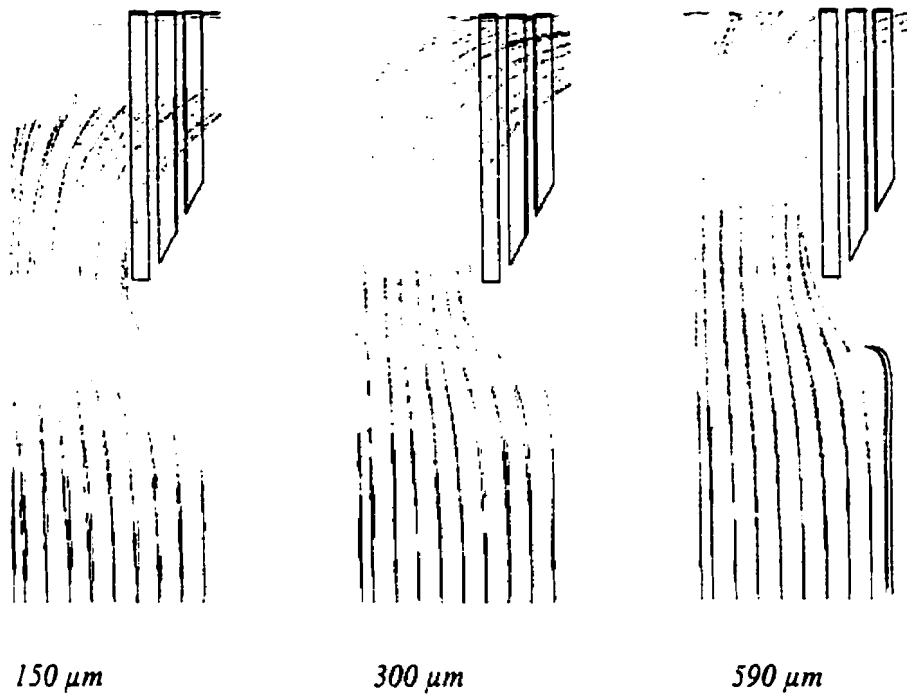


Figure 5.22 Particle trajectories in the upper furnace

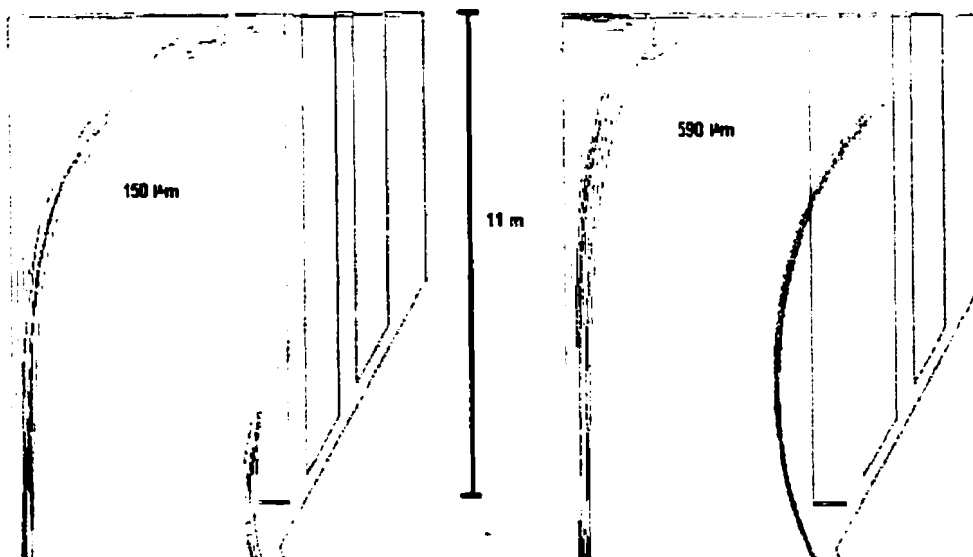


Figure 5.23 Particle trajectories for different sizes of 150 and 590 μm

The distribution of 150, 300, and 590 μm particles on the first platen is shown in Figure 5.24. As discussed earlier the small particles are more evenly distributed on the tubes while larger particles are more concentrated on the upper part of the tubes. When gas begins to turn horizontally towards the exit of the upper furnace after passing the bullnose, larger particles move upward toward the middle part of the tubes. That is true for all of the particles passing close to the bullnose thus all these particles hit the tube at approximately the same region. Therefore the 300 and 590 μm particles are more concentrated at 6.5 and 4 m below the top wall on the tubes, respectively. Smaller particles turn toward the exit of the upper furnace with the flue gas and thus they are distributed uniformly on the tubes. It should be noted that the above discussion might not be true for recovery boilers with smaller superheater section.

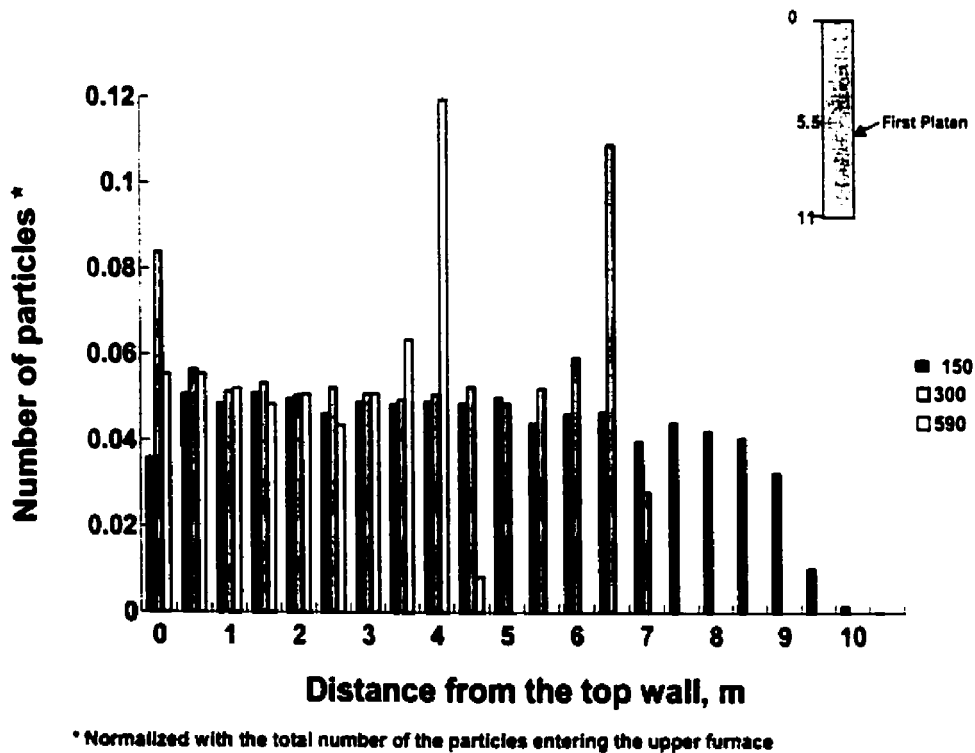


Figure 5.24 Distribution of 150, 300, and 590 μm particles on the first platen

The temperature and liquid content of particles that impact the three platens are predicted under two boiler conditions, clean and fouled. At each point 500 particles were introduced to the model. Figures 5.25-5.27 show the particle temperature distribution at the first platen for the clean boiler case and 150, 300, and 590 μm particles. The temperature of the particles is shown as a mean value with the bars indicating the highest and the lowest predicted values. All the particles are above CMT before entering the convection section. In the convection section, the temperature of the gas cools rapidly and the particle temperatures begin to decrease. Smaller particles cool faster than the large particles thus they have lower temperature when they pass the first platen. Particles passing the upper part of the tubes, close to the top wall, cool the most since these particles have sufficient time to respond to the heat transfer in the convection section. The region close to the top wall is a low temperature region and also has a high temperature gradient due to the proximity of the top wall and superheater tubes. The increased variability in temperature of the larger particles in the top region is due to the high temperature gradients. Also, particles from the same source may take different paths in the upper furnace resulting in different temperatures.

The composition of the carryover found in boilers is more complicated than the simplified particles considered in this study and thermal behavior of carryover and simplified particles might be different.

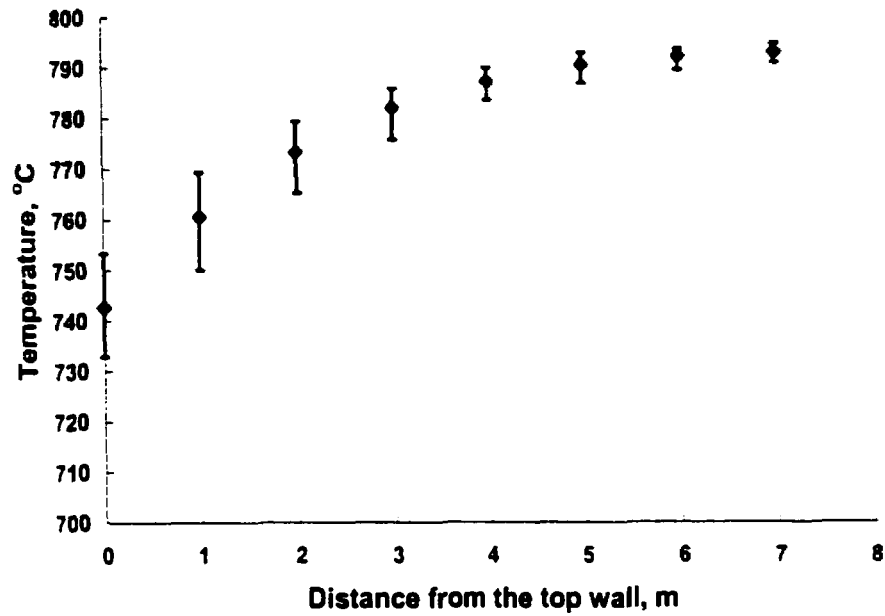


Figure 5.25 Particle temperature at the first platen, clean boiler case
 10 mole% Cl/(Na+K) and 0 mole% K/(Na+K) and 150 μm particle size

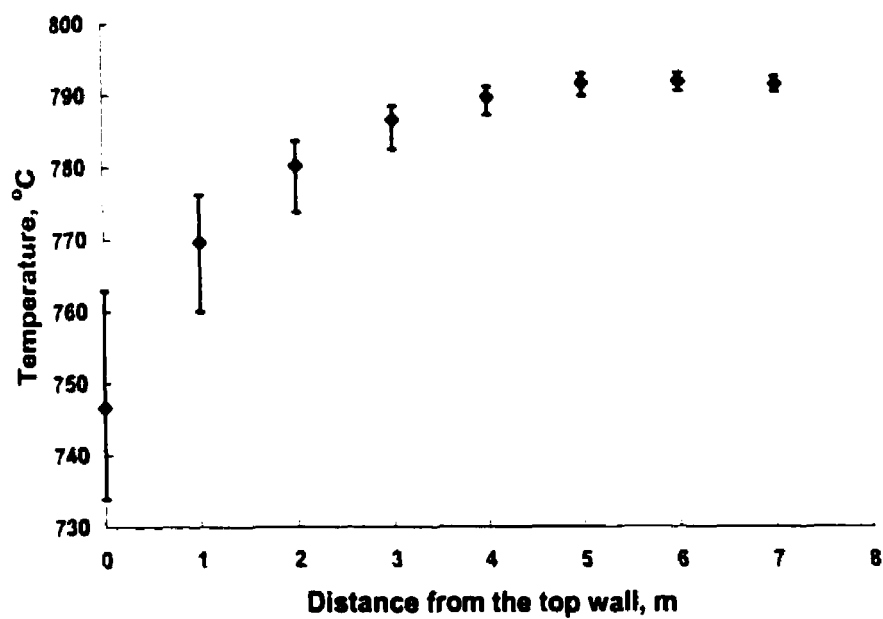


Figure 5.26 Particle temperature at the first platen, clean boiler case
 10 mole% Cl/(Na+K) and 0 mole% K/(Na+K) and 300 μm particle size

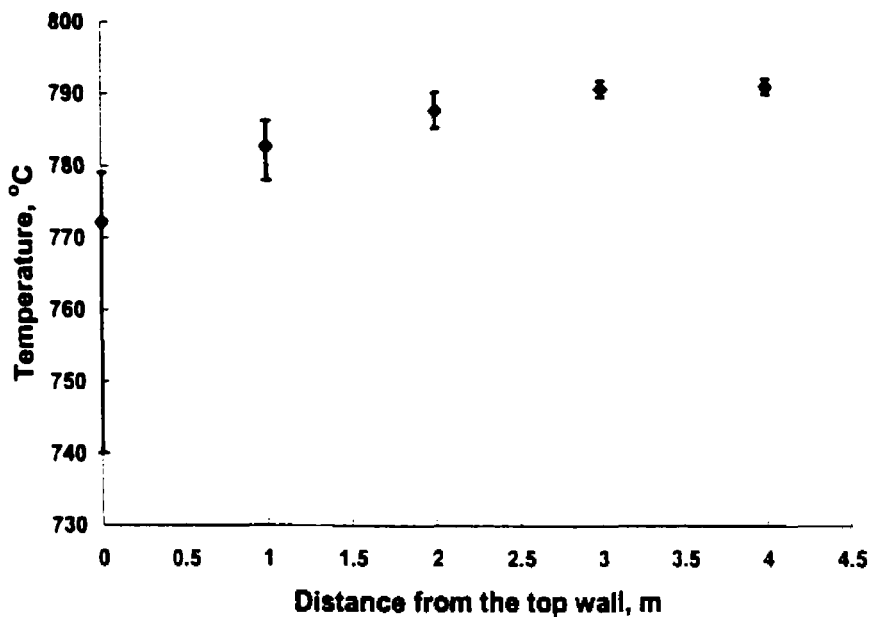


Figure 5.27 Particle temperature at the first platen, clean boiler case

10 mole% Cl/(Na+K) and 0 mole% K/(Na+K) and 590 μ m particle size

Figures 5.28-5.30 show the liquid content of 150, 300, and 590 μ m particles at the first platen. The liquid content results are consistent with the temperature results. These results show that the particles are partially or completely molten when they pass the first platen indicating that if they hit the tubes they will deposit on them since the surface temperature of the tubes are lower than the radical deformation temperature.

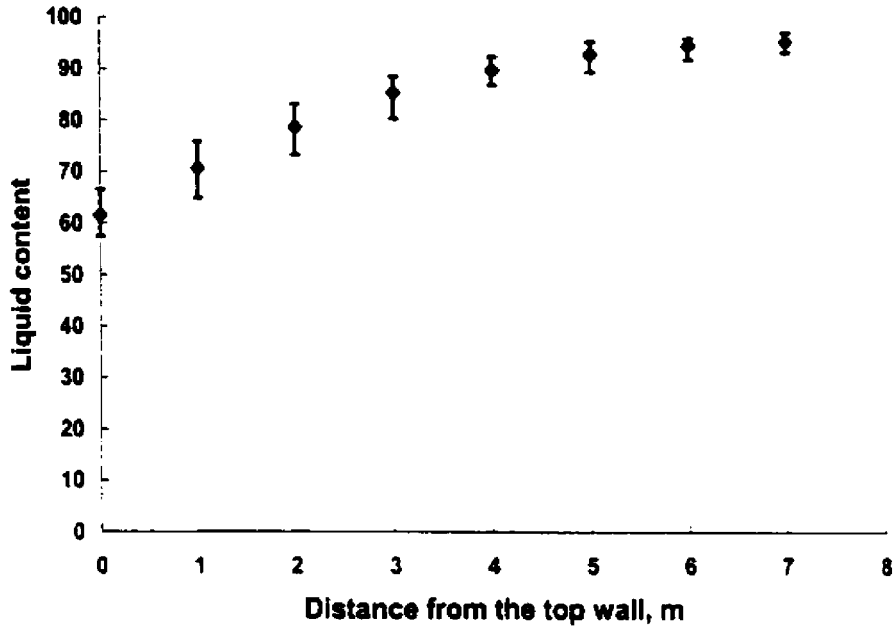


Figure 5.28 Particle liquid content at the first platen, clean boiler case
 10 mole% $Cl/(Na+K)$ and 0 mole% $K/(Na+K)$ and 150 μm particle size

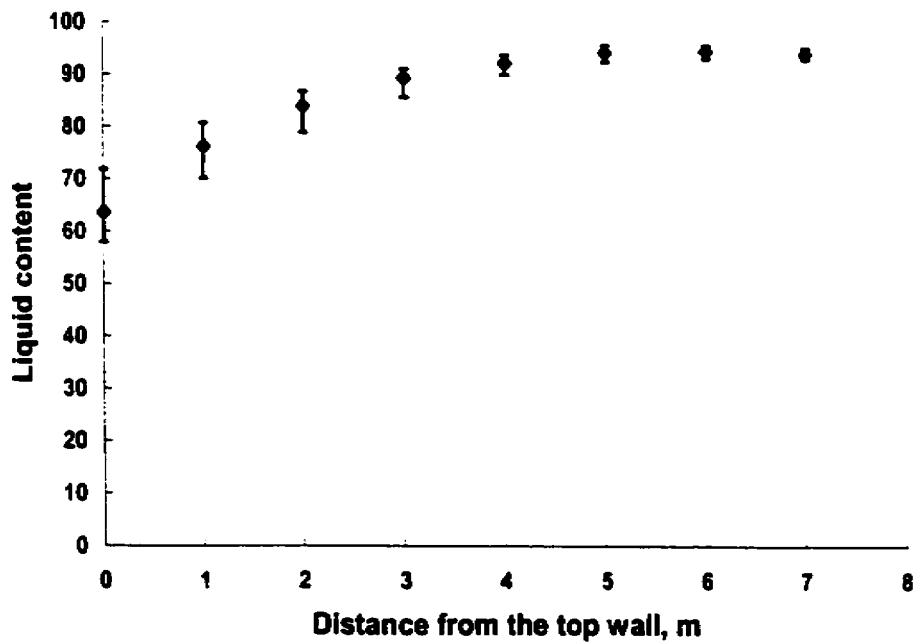


Figure 5.29 Particle liquid content at the first platen, clean boiler case
 10 mole% $Cl/(Na+K)$ and 0 mole% $K/(Na+K)$ and 300 μm particle size

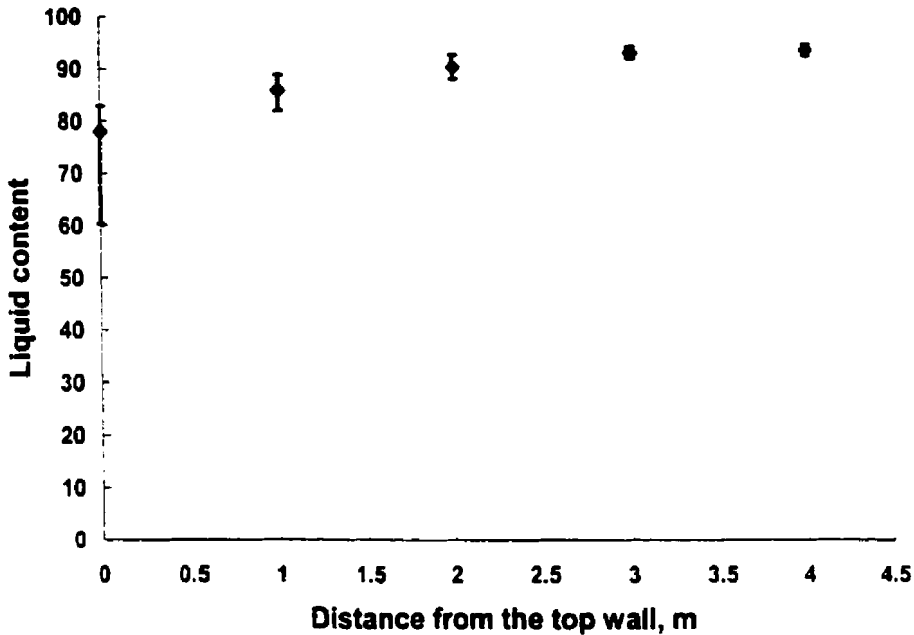


Figure 5.30 Particle liquid content at the first platen, clean boiler case

10 mole% Cl/(Na+K) and 0 mole% K/(Na+K) and 590 μm particle size

Figures 5.31-5.33 show the particle temperature for different sizes of 150, 300, and 590 μm particles at the second platen. As discussed before, smaller particles have lower temperature since they cool faster than larger particles. Particles that are not captured by impaction on the first platen are transported to the second platen. The temperature of the particles passing the second platen decreases, but it is still higher than the sticky temperature. These particles would deposit on the tubes if they hit the surface of the tubes. The gas temperature continues to decrease after the second platen to below the sticky temperature and therefore particles would solidify and not deposit on the third platen. Therefore, carryover deposition is confined to the first and second platens where particles are partially or completely molten. This is consistent with other numerical studies [52].

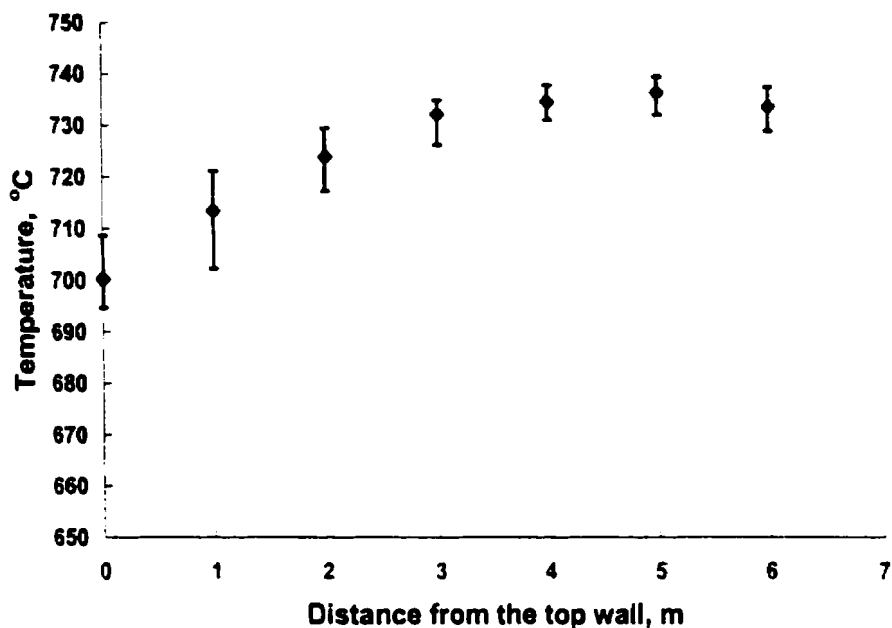


Figure 5.31 Particle temperature at the second platen, clean boiler case

10 mole% $Cl/(Na+K)$ and 0 mole% $K/(Na+K)$ and 150 μm particle size

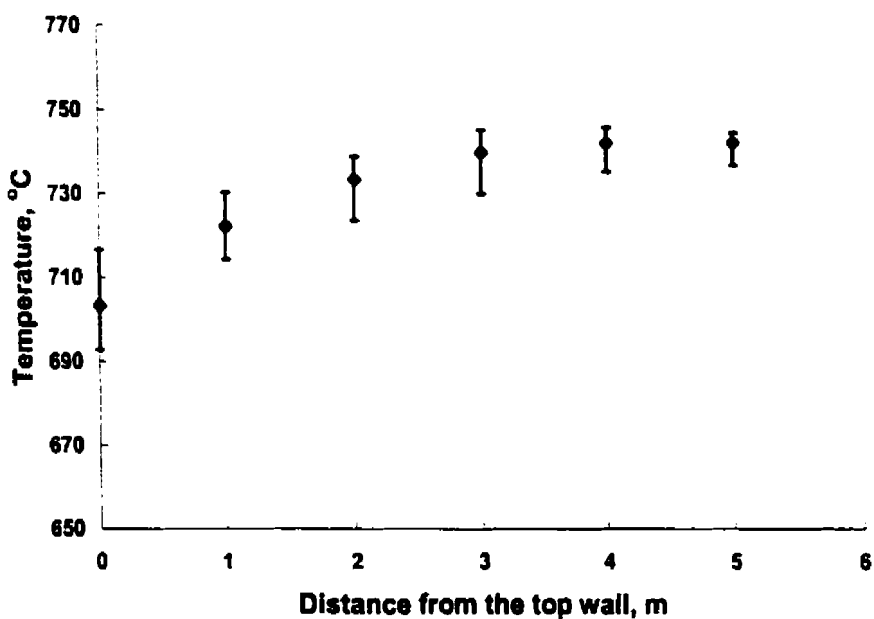


Figure 5.32 Particle temperature at the second platen, clean boiler case

10 mole% $Cl/(Na+K)$ and 0 mole% $K/(Na+K)$ and 300 μm particle size

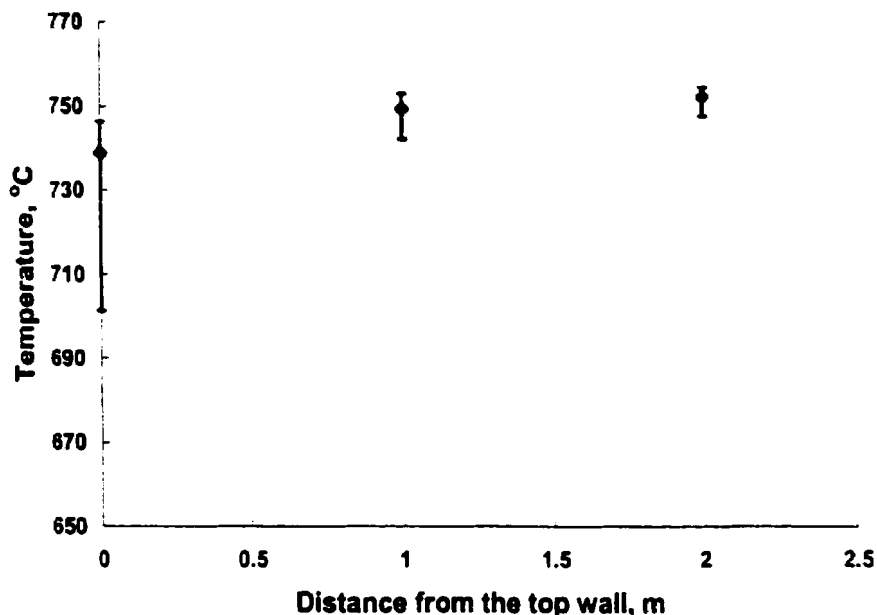


Figure 5.33 Particle temperature at the second platen, clean boiler case

10 mole% Cl/(Na+K) and 0 mole% K/(Na+K) and 590 μm particle size

In a fouled boiler case, deposits that accumulate on the tubes increase the temperature of the tube and deposit surface resulting in a higher gas and particle temperature through the convection section. Figure 5.34 shows the temperature contours in the upper furnace for a fouled boiler case. Figures 5.35 and 5.36 show the temperature variation of 150 and 300 μm particles at the first platen for the case of a fouled boiler. Higher gas temperatures in the upper furnace result in particles with higher temperature compared to a clean boiler case. In a fouled boiler, the surface temperature of the platen is higher than the radical deformation temperature meaning that if the particles hit the tubes they will run off the surface and the deposit stops growing. This is consistent with literature [47]. Also, particles passing the second platen have higher temperature resulting in a higher deposition compare to the clean boiler case.

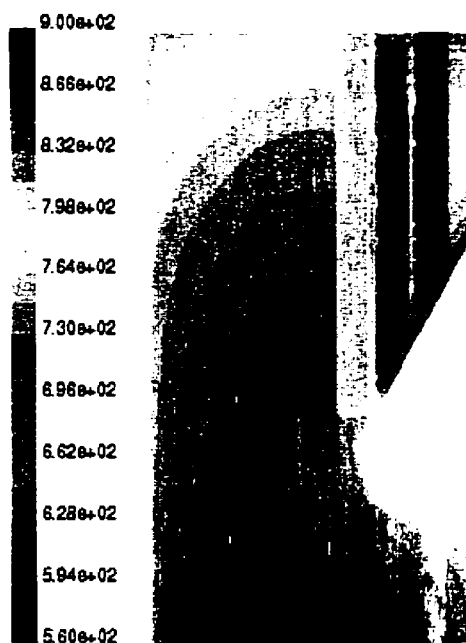


Figure 5.34 Gas temperature contours on central plane in a fouled boiler case ($^{\circ}\text{C}$)

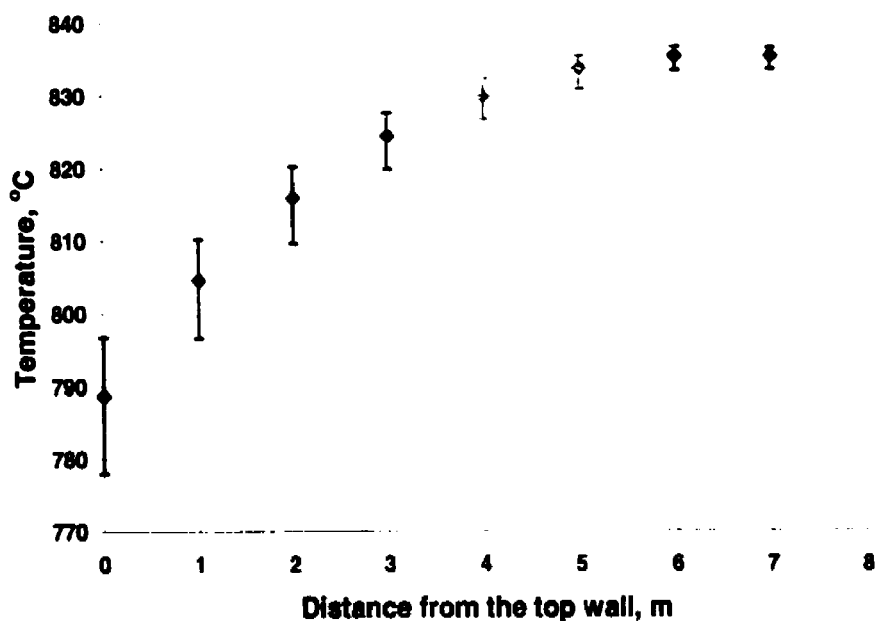


Figure 5.35 Particle temperature at the first platen, fouled boiler case

10 mole% $\text{Cl}/(\text{Na}+\text{K})$ and 0 mole% $\text{K}/(\text{Na}+\text{K})$ and $150\ \mu\text{m}$ particle size

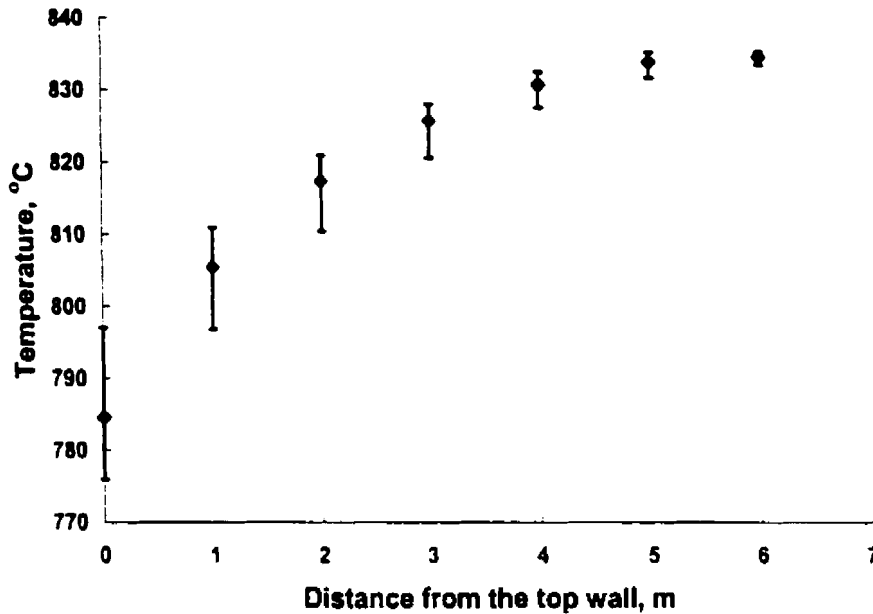


Figure 5.36 Particle temperature at the first platen, fouled boiler case
 10 mole% Cl/(Na+K) and 0 mole% K/(Na+K) and 300 μm particle size

5.2.4 Summary

A simplified upper furnace model was developed for predicting carryover temperature and liquid content in the convection section of a boiler. Carryover deposition on tube surfaces was estimated based on carryover temperature and liquid content. In a clean boiler, $\text{Na}_2\text{SO}_4\text{-NaCl}$ particles have enough liquid content to deposit on the surface of the first platen. Passing the second platen, the temperatures of particles are still in the sticky zone and they deposit on the tubes. Particles reaching the third platen have been cooled below the sticky temperature and thus they do not have sufficient liquid content to stick to tubes. In a fouled boiler, the gas is not cooled effectively due to the presence of the deposits on the tubes and the surface temperature of the tubes is higher than the radical deformation temperature. Therefore, particles cool less rapidly and as a result particles

contain a large amount of liquid content at the first platen and tend to slag off the surface if they hit the tubes. The particles have sufficient time to cool prior to the second platen and solidify enough to form deposit on the second platen. These results are in agreement with literature and other numerical studies [47,54,52].

6. Implications

The major implication of this study is that a particle-tracking algorithm to describe the velocity, temperature, and liquid content history of particles is available for deposit growth studies in kraft recovery boilers.

The present study predicts that there is a uniform distribution of small particles across the height of the superheater tubes and a higher concentration of larger particles on the upper part of the tubes and the top wall. Since smaller particles cool more quickly than larger particles they contain a lower liquid phase and the lack of liquid phase makes the particles retain their spherical shape on the tubes. The deposit formed by small particles on the tubes is porous due to their solid state resulting in a void between them, consequently, it is easier to remove the deposit by sootblower [46]. On the other hand, larger particles contain higher liquid phase even at low chloride content since they cool more slowly and therefore, the deposit they form on the tubes is not easy to remove. This suggests that control of large particle entrainment would reduce problematic fouling.

In a clean boiler, particles with low chloride content might not have sufficient liquid content to deposit on the tubes. However in a fouled boiler, the gas is not cooled effectively and its temperature is higher, therefore, even the low chloride containing particles or small particles have sufficient liquid phase to deposit on the tubes. As the

superheater continues to foul the gas temperatures downstream further increases. If the gas temperature at the boiler bank inlet is elevated above the sticky temperature the particles will remain molten resulting in rapid fouling and boiler pluggage.

At locations in the boiler where the gas temperature is higher than the radical deformation temperature, particles with high chloride content form a thinner deposit on the first platen. That is because the outer surface of the tubes reaches the particle radical deformation temperature more quickly. Particles with very low chloride content do not have sufficient liquid content to deposit on the tubes. Therefore there is less deposit formed on the tubes at very high or very low chloride contents.

It should be noted that these results might not be directly applicable to the recovery boiler although they bring some insights into the dynamics of carryover deposition.

The implications are mostly applicable to the specific recovery boiler geometry considered in this model. For example, for boilers with larger bullnose the gas flow field and the trajectory of particles would be different resulting in high concentration of large particles on the lower part of the tubes.

7. Conclusions

An algorithm for tracking the velocity, temperature, and liquid content of synthetic carryover particles ($\text{Na}_2\text{SO}_4\text{-NaCl-K}_2\text{SO}_4$) was integrated within a commercially available computational fluid dynamics (CFD) package. The particle-tracking algorithm can accurately predict the temperature and liquid content of $\text{Na}_2\text{SO}_4\text{-NaCl-K}_2\text{SO}_4$ containing particles. The algorithm can be easily modified to consider other particle compositions with the availability of appropriate thermodynamic data.

Small particles are completely molten when they exit the entrained flow reactor (EFR) but they may not have sufficient liquid content to adhere to the probe since they cool quickly in the non-heated section. Conversely, the larger particles (430 and 590 μm) do not reach the complete melting temperature prior to the exit of the EFR but have a high enough liquid content to adhere to the probe since they cool slowly in the non-heated section.

For $\text{Na}_2\text{SO}_4\text{-NaCl}$ particles above the FMT and below the CMT, the proportion of energy absorbed to melt particles increases with chloride content and consequently lower chloride containing particles increase in temperature more rapidly. For the case of 260 μm particles, the CMT was reached for only the 20 mole% $\text{Cl}/(\text{Na}+\text{K})$ case and thus they have a higher temperature compare to lower chloride containing particle.

Although particles containing potassium reached their FMT faster than the particles with no potassium, there is no significant difference between the particle temperatures and liquid contents.

Radiative heat transfer is the dominant mode of heat transfer in the non-heated section of the EFR.

The particle-tracking algorithm was successfully implemented in a three-dimensional simplified model of a kraft recovery boiler upper furnace. Small particles (150 μm) were predicted to distribute uniformly across the height of the superheater tubes, whereas larger particles (590 μm) would deposit preferentially on the upper wall and upper half of the tubes.

In the clean boiler simulation, particles are partially or completely molten when they reach the first platen and they stick to the tubes upon impact since the surface temperature of the tubes is low. As the particles pass through the first platen and cool, their temperature is still higher than the sticky temperature and they deposit on the second platen. Particles that reach the third platen are below the sticky temperature and would not deposit.

In the fouled boiler simulation, the gas is not cooled effectively due to the presence of the deposits on the tubes. The deposit insulates the outer surface from the cooling effect of

the tube so the surface temperature increases with thickness. At this point, If particles hit the tubes they would slag off the surface and the deposits would stop growing. The deposit continues to grow on the second platen since its surface temperature is lower than the radical deformation temperature.

8. Recommendations

Based on the results obtained from the present study, the following recommendations can be made for further investigations:

Extending the particle-tracking algorithm to more complicated compositions to predict more realistic carryover deposition characteristics.

In the EFR model, change the flue gas temperature and velocity, and the surface temperature of the deposit-collecting probe to investigate their effects on particle temperature and liquid content. These results could then be used to further interpret the extensive experimental data.

Apply the particle-tracking algorithm to a more complicated and realistic model of the upper furnace.

References

1. Adams, T. N., Black Liquor Combustion, Chapter 20, *Tappi Press* (1992).
2. Adams, T. N., Frederick, W. J., Kraft Recovery Boiler Physical and Chemical Processes, *American Paper Institute* (1988).
3. Adam, T. N., Kraft Recovery Boilers-Chapter 1: General Characteristics of Kraft Black Liquor Recovery Boilers, Edited by Adams, T. N., *Tappi Press* (1997).
4. Adeniji-Fashola, A., Chen, C. P., "Modeling of Confined Turbulent Fluid-Particle Flows Using Eulerian and Lagrangian Schemes", *Int. Journal of Heat and Mass Transfer*, Vol. 33, No. 4, pp. 691-701 (1990).
5. Avila, R., Cervantes, J., "Analysis of the Heat Transfer Coefficient in a Turbulent Particle Pipe Flow", *Int. Journal of Heat and Mass Transfer*, Vol. 38, No. 11, pp. 1923-1932 (1995).
6. Barth, T. J., Jespersen, D., "The Design and Application of Upwind Schemes on Unstructured Meshes", Technical Report AIAA-89-0366, *AIAA 27th Aerospace Sciences Meeting*, Reno, Nevada (1989).
7. Baxter, L. L., "Turbulent Transport of Particles", *Ph.D. Thesis*, Brigham Young University (1989).
8. Baxter, L. L., Smith, P. J., "Turbulent Dispersion of Particles: The STP Model", *Energy & Fuels*, Vol. 7, No. 6 (1993).

9. Boulet, P., Oesterle, B., Taniere, A., "Numerical Simulation of Heat Transfer in a Gas-Solid Pipe Flow", *ASME Fluids Engineering Division Summer Meeting*, (1997).
10. Cheng, P., "Two-Dimensional Radiating Gas Flow by a Moment Method", *AIAA Journal*, Vol. 2, pp. 1662-1664 (1964).
11. Cook, L. P., McMurdie, H. F., Phase Diagrams for Ceramists, Volume I, *The American Ceramic Society* (1989).
12. Crowe, C. T., "REVIEW-Numerical Models for Dilute Gas-Particle Flows", *Transactions of ASME, Journal of Fluids Engineering*, Vol. 104, No. 3 (1982).
13. DeWitt, D. P., Incropera, F. P., Fundamentals of Heat and Mass Transfer, *John Wiley & Sons* (1990).
14. Ferziger, J. H., Peric', M., Computational Methods for Fluid Dynamics, Second Edition, *Springer* (1999).
15. Fiveland, W. A., Jamaluddin, A. S., "Three-Dimensional Spectral Radiative Heat Transfer Solutions by the Discrete-Ordinates Method, *Journal of Thermophysics*, Vol. 5, No. 3, pp. 335-339 (July-Sept., 1991).
16. Fluent, Inc, Manual.
17. Frederick, W. J., Hupa, M., "Kraft Recovery Boilers-Chapter 5: Black Liquor Droplet Burning Processes", Edited by Adams, T. N., *Tappi Press* (1997).
18. Grace, T. M., Overview of Kraft Recovery, Chapter 18, Co-edited by Green, R. P., and Hugh, G., Third Edition, *TAPPI Press* (1992).

19. Grace, T., Walsh, A., Jones, A., Sumnicht, D., Farrington, "A Three-Dimensional Mathematical Model of the Kraft Recovery Furnace", *The Institute of Paper Chemistry Appleton, Wisconsin*.
20. Haider, A., Levenspiel, O., "Drag Coefficient and Terminal Velocity of Spherical and Non-spherical Particles", *Powder Technology*, Vol. 58, pp. 63-70 (1989).
21. Han, K. S., Sung, H. J., Chung, M. K., "Analysis of Heat Transfer in Pipe Carrying Two-Phase Gas-Particle Suspension", *Int. Journal of Heat and Mass Transfer*, Vol. 34, pp. 69-78 (1991).
22. Heisler, M. P., "Temperature Charts for Induction and Constant-Temperature Heating", *Transactions of the ASME*, pp. 227-236, April (1947).
23. Hesketh, H. E., *Fine Particles in Gaseous Media*, Second Edition, *Lewis Publishers, Inc.* (1986).
24. Hinds, W. C., *Aerosol Technology –Properties, Behavior, and Measurement of Airborne Particles*, *John Wiley & Sons*, Fourth Edition (1996).
25. Isaak, P., Tran, H. N., Barham, D., Reeve, D. W. "Stickiness of Fireside Deposits in Kraft Recovery Units", *Journal of Pulp and Paper Science*, 12(3): j84-88 (1986).
26. Isaak, P., Tran, H. N., Barham, D., Reeve, D. W. "Stickiness of Fireside Deposits in Kraft Recovery Units-Part 2: The Effects of Potassium and Surface Treatment", *Journal of Pulp and Paper Science*, 13(5): j154-158 (1987).
27. Israel, R., Rosner, D. E., "Use of a Generalized Stokes Number to Determine the Aerodynamic Capture Efficiency of Non-Stokesian Particles from a Compressible Gas Flow", *Aerosol Science and Technology*, 2:45-51 (1983).

28. Jang, D. S., Acharya, S., "Calculation of Particle Dispersion Due to Turbulence in Elliptic Flows", *AIChE Journal*, Vol. 34, No. 3, pp. 514-518, March (1988).
29. Litchford, R. J., Jeng, S. M., "Efficient Statistical Transport Model for Turbulent Particle Dispersion in Sprays", *AIAA Journal*, 29:1443 (1991).
30. Michaelides, E. E., "Heat Transfer in Particulate Flows", *Int. Journal of Heat and Mass Transfer*, Vol. 29, No. 2, pp. 265-273 (1985).
31. Morsi, S. A., Alexander, A. J., "An Investigation of Particle Trajectories in Two-Phase Flow Systems", *Journal of Fluid Mechanics*, Vol. 55, Part 2, pp. 193-208 (1972).
32. Naseri, M., "Effect of Particle Impact Velocity on Carryover Deposition", *M.A.Sc. Thesis*, University of Toronto (2000).
33. Patankar, S. V., *Numerical Heat Transfer and Fluid Flow*, Hemisphere (1980).
34. Patankar, S. V., Spalding, D. B., "A Calculation Procedure for Heat, Mass, and Momentum Transfer in Three-Dimensional Parabolic Flows", *Int. Journal of Heat and Mass Transfer*, Vol. 15, pp. 1787-1806 (1972).
35. Plikas, A., "Numerical Modeling of Fibre Suspensions in Grid-Generated Turbulent Flow", *M.A.Sc. Thesis*, University of Toronto (2000).
36. Ranz, W. E., Marshall, W. R., Jr. "Evaporation from Drops, Part I.", *Chem. Eng. Prog.*, Vol. 48(3) pp.141-146 (1952).
37. Rezvani, K., "Effect of Potassium and Carbonate on the Deposition of Synthetic Recovery Boiler Carryover Particles", *M.A.Sc. Thesis*, University of Toronto (2000).

38. Rosner, D. E., Tandon, P., "Rational Prediction of Inertially Induced Particle Deposition Rates for a Cylindrical Target in a Dust-Laden Stream", *Chemical Engineering Science*, Vol. 50, No. 21, pp. 3409-3431 (1995).
39. Rudinger, G., *Fundamentals of Gas-Particle Flow*, Vol. 2, *Elsevier Publication*.
40. Shen, X. H., Kuhn, D. C. S., Tran, H. N., Mostaghimi, J., Dees, C., "Simulation of Flue Gas Flow in the Upper Furnace of a Recovery Boiler", *Pulp and Paper Canada*, 96:5 (1995).
41. Shenassa, R., "Dynamic Carryover Deposition in an Entrained Flow Reactor", *Ph.D. Thesis*, University of Toronto (2000).
42. Shenassa, R., Kuhn, D. C. S., Tran, H. N., "The Role of Liquid Content in Carryover Deposition in Kraft Recovery Boilers- A Fundamental Study", *International Chemical Recovery Conference* (2001).
43. Siegel, R., Howell, J. R., *Thermal Radiation Heat Transfer*, *Hemisphere Publishing Corporation* (1992).
44. Tran, H. N., "How Does a Kraft Recovery Boiler Become Plugged?", *Tappi Journal*, 69(11):102-106 (1986).
45. Tran, H. N., "Recovery Boiler Fireside Deposits and Plugging Prevention", *Tappi Kraft Recovery Short Course*, p.5.9 (2000).
46. Tran, H. N., "Research Consortium on Improving Recovery Boiler Performance, Emissions and Safety", November (2000).
47. Tran, H. N., "Kraft Recovery Boilers-Chapter 9: Upper Furnace Deposition and Plugging", Edited by Adams, T. N., *Tappi Press* (1997).

48. Tran, H. N., Gonsko, M., Mao, X., "Effect of Composition on the First Melting Temperature of Fireside Deposits in Recovery Boilers", *Tappi Journal*, 82(9): 93-100 (1999).
49. Tsuji, Y., Morikawa, Y., Shiomi, H., "LDV Measurements of an Air-Solid Two-Phase Flow in a Vertical pipe", *Journal of Fluid Mechanics*, Vol. 139, pp. 417-434 (1989).
50. Verrill, C. L., Wessel, R., "Sodium Loss During Black Liquor Drying and Devolatilization-Application of Modeling Results to Understanding Laboratory Data", *Proceedings of 1995 International Chemical Recovery Conference*, pp. B89, April 24 (1995).
51. Wang, H. C., "Theoretical Adhesion Efficiency for Particles Impacting a Cylinder at High Reynolds Number", *Journal of Aerosol Science*, Vol. 17, No. 5, pp. 827-837 (1986).
52. Wessel, R. A., Baxter, L., "Comprehensive Model of Alkali Salt Deposition in Recovery Boilers", *International Chemical Recovery Conference*, pp. 103-108 June (2001).
53. Wessel, R. A., Denison, M. K., Samretvanich, A., "The Effect of Fume on Radiative Heat Transfer in Kraft Recovery Boilers", *TAPPI proceedings International Chemical Recovery Conference*, Vol. 2, June (1998).
54. Wessel, R. A., Parker, K. L., Verrill, C. L., "Three-Dimensional Kraft Recovery Furnace Model: Implementation and Results of Improved Black Liquor Combustion Models", *TAPPI Journal*, 80(10): 207-220 (1997).

55. Wessel, R. A., Righi, J., "Generalized Correlation for Inertial Impaction of Particles on a Circular Cylinder", *Aerosol Science and Technology*, 9:29-60 (1988).
56. Wessel, R. A., Samretvanich, A., "The Effect of Fume on Radiative Heat Transfer in Kraft Recovery Boilers, *McDermott Technology Inc.*, (1999).

Appendix

Particle tracking algorithm developed to predict particle temperature and liquid content was implemented as a user-defined function (UDF) in Fluent™. The code was written in C programming language. To define a particle heat transfer equation, the following variable defined in Fluent™ is used to call the functions:

```
#define DEFINE_DPM_LAW(inert_heating, p, ci)
```

To track the particle properties the following designations are used:

P_DIAM(p)	particle diameter
P_T(p)	particle temperature
P_MASS(p)	particle mass
P_DT(p)	particle time step

The flue gas properties at each cell that is visited by the particle can be tracked by the following variables:

c->sHeat	specific heat
c->G	radiation intensity
c->mu	viscosity
c->tCond	thermal conductivity
c->temp	gas temperature

All the user-defined functions are executed in Fluent™ as compiled UDF's. The user-defined functions are given in the following pages.

Case 1: Particle temperature in the EFR with composition of 10 mole% Cl/(Na+K)

```
#include "udf.h"
#include "dpm.h"
static FILE *fp;

DEFINE_DPM_LAW(inert_heating,p,ci)
{
float D,M,TI ,H,Pr,Nu,TI4,area,N,w,Q1;
static float Q,L;

cphase_state_t *c = &(p->cphase);      /* particles interaction with the fluid phase*/
if(p->state.pos[2]<1.e-12)
    Q=0;

D=P_DIAM(p);
TI=P_T(p);
M=P_MASS(p);
TI4=pow(TI,4);
area=3.14*D*D;

w=.9*5.67e-8*area*(c->G/(4*5.67e-8)-TI4);      /*radiation heat transfer*/
Pr=c->sHeat*c->mu/c->tCond;                    /*Prandtl number*/
Nu=2+.6*sqrt(p->Re)*pow(Pr,1/3);              /*Nusselt number*/
H=Nu*c->tCond/D;                              /*heat transfer coefficient*/
Q1=H*area*(c->temp-TI)+w; /*radiation and convection heat transfer to the particle*/
N=Q1*P_DT(p)/M;
Q=Q+N;
L=18*4.8214/(1157-TI);                       /*particle liquid content for 10% Cl/(Na+K)*/
if(Q<817961)                                  /* 817961 J/Kg = enthalpy to change particle phase */
    {
    P_T(p)=TI+Q1*P_DT(p)/(M*1361);
    L=0;
    }
else if(Q>817961 && Q<893551)                 /*893551J/Kg=latent heat +817961*/
    {
    P_T(p)=901;                               /*first melting temperature*/
    L=L+Q1*P_DT(p)/(M*222978);
    }
else if( Q>893551 && L<1 && L>0)             /*complete melting temperature*/
    {
    P_T(p)=TI+Q1*P_DT(p)/(M*(222978*L/(1157-TI)+1361));
    }
```

```

    L=18*4.8214/(1157-TI);
}
else
    /*liquid phase*/
    {
        P_T(p)=TI+Q1*P_DT(p)/(M*1354);
        L=1;
    }
fp=fopen("Qoutput.txt","a");
fprintf(fp, "%f %f %f \n",p->state.pos[2],P_T(p)-273.15,L);
fclose(fp);}

```

Case 2: Particle temperature close to the first platen in the upper furnace with composition of 10 mole% Cl/(Na+K)

```

include "udf.h"
#include "dpm.h"
#define PI 3.14
static FILE *fp;

DEFINE_DPM_LAW(inert_heating,p,ci)
{
    float D,M,TI,A,B,V,H,Pr,Nu,TI4,area,N;
    float w,Q1,L;
    static float Q;
    static int flag;

    cphase_state_t *c = &(p->cphase);

    if(p->state.pos[1]<1.e-12)
    {
        Q=0;
        flag=1;
    }

    D=P_DIAM(p);
    TI=P_T(p);
    M=P_MASS(p);
    TI4=pow(TI,4);
    area=PI*D*D;

    w=9*5.67e-8*area*(c->G/(4*5.67e-8)-TI4); /*radiation*/
    Pr=c->sHeat*c->mu/c->tCond;
    Nu=2+.6*sqrt(p->Re)*pow(Pr,1/3);
    H=Nu*c->tCond/D;
    Q1=H*area*(c->temp-TI)+w; /*radiation and convection heat transfer*/

```

```

N=Q1*P_DT(p)/M;
Q=Q+N;
L=18*4.8214/(1157-TI);          /*particle liquid content for 10% Cl/(Na+K)*/
if(Q<817961)                    /* 817961 J/Kg = enthalpy to change particle phase */
{
    P_T(p)=TI+Q1*P_DT(p)/(M*1361);
    L=0;
}
else if(Q>817961 && Q<893551)    /*893551J/Kg=latent heat +817961*/
{
    P_T(p)=901;                  /*first melting temperature*/
    L=L+Q1*P_DT(p)/(M*222978);
}
else if( Q>893551 && L<1 && L>0) /*complete melting temperature*/
{
    P_T(p)=TI+Q1*P_DT(p)/(M*(222978*L/(1157-TI)+1361));
    L=18*4.8214/(1157-TI);
}
else                             /*liquid phase*/
{
    P_T(p)=TI+Q1*P_DT(p)/(M*1354);
    L=1;
}

if(p->state.pos[1]>13 )
{
    if (p->state.pos[0]>5.999 && flag)
    {
        fp=fopen("Qoutput.txt","a");
        fprintf(fp, " %f %f %f %f %d\n",p->state.pos[0],p->state.pos[1],
P_T(p)-273.15, L);
        fclose(fp);
    }
    flag=0;
}
}
}

```

Case 3: Particle temperature in the EFR with composition of 10 mole% Cl/(Na+K) and 5 mole% K/(K+Na)

```

#include "udf.h"
#include "dpm.h"
#define PI 3.14
#define size 38
static FILE *fp;
static FILE *cfp;

```

```

DEFINE_DPM_LAW(inert_heating,p,ci)
{

float D,M,TL,H,Pr,Nu,TI4,area,N, Z,L1,T,Y,X1,X2;
float F13,F14,w,Q1, s[size],L[size];
int i;
static float Q;
static int j;

cphase_state_t *c = &(p->cphase); /* particles interaction with the fluid phase*/

if(p->state.pos[2]<1.e-12)
{
    Q=0;
    Z=0;
    i=0;
    j=0;
}

D=P_DIAM(p);
TI=P_T(p);
M=P_MASS(p);
TI4=pow(TI,4);
area=PI*D*D;

w=.9*5.67e-8*area*(c->G/(4*5.67e-8)-TI4); /*radiation*/
Pr=c->sHeat*c->mu/c->tCond;
Nu=2+.6*sqrt(p->Re)*pow(Pr,1/3);
H=Nu*c->tCond/D;
Q1=H*area*(c->temp-TI)+w; /*radiation and convection heat transfer*/
N=Q1*P_DT(p)/M;
Q=Q+N;

cfp=fopen("Tra0061.txt","r");
while(!feof(cfp)){
    for(i=0;i<=(size-1);i++)
    {
        fscanff(cfp,"%G %G",&T,&L1);

        s[i]=T+273.15;
        L[i]=L1/100;}
    }
fclose(cfp);
}

```

```

        X1=1361*(s[0]-300);
        X2=X1+(222979.351*L[0]);

    if(Q<X1) /* 817961 J/Kg =enthalpy to change particles phase[ Q1=Cp*(fmt-300) ]*/
        P_T(p)=TI+Q1*P_DT(p)/(M*1361);

    else if(Q>X1 && Q<X2) /*893551 J/Kg=latent heat +817961 [Q=Q1+latent*L]*/
        P_T(p)=s[0]+1.e-4; /*first melting temperature*/

    else if(Q>X2 && P_T(p)<(s[34])) /*complete melting temperature*/
        {
        start:
            if (P_T(p)>(s[j]) && P_T(p)<(s[j+1]))
                {
                Z=((L[j+1]-L[j])/(s[j+1]-s[j]));

                P_T(p)=TI+Q1*P_DT(p)/(M*(222979.351*Z+1361));
                    goto end;
                }

            }

        else
            {
                if ( P_T(p)>s[j+1] )
                    j=j+1;

                else
                    j=j-1;
            }

        goto start;

    }

    else /*liquid phase*/

        P_T(p)=TI+Q1*P_DT(p)/(M*1354);

    end:
        fp=fopen("Qoutput.txt","a");
        fprintf(fp, " %f %f %f %f\n" ,p->state.pos[2],(P_T(p)-273.15),j, L[j]);
        fclose(fp);

}

```

One example of the thermodynamic data for particles containing 10 mole% Cl/(Na+K) and 5 mole% K/(K+Na) is shown below:

File name: Tra006

Temperature	liquid content
6.05E+02	9.37E+00
6.06E+02	2.62E+01
6.10E+02	2.65E+01
6.15E+02	2.72E+01
6.20E+02	2.79E+01
6.25E+02	2.87E+01
6.30E+02	2.95E+01
6.35E+02	3.04E+01
6.40E+02	3.12E+01
6.45E+02	3.22E+01
6.50E+02	3.31E+01
6.55E+02	3.42E+01
6.60E+02	3.52E+01
6.65E+02	3.64E+01
6.70E+02	3.75E+01
6.75E+02	3.88E+01
6.80E+02	4.01E+01
6.85E+02	4.15E+01
6.90E+02	4.30E+01
6.95E+02	4.45E+01
7.00E+02	4.62E+01
7.05E+02	4.79E+01
7.10E+02	4.98E+01
7.15E+02	5.17E+01
7.20E+02	5.38E+01
7.25E+02	5.61E+01
7.30E+02	5.85E+01
7.35E+02	6.11E+01
7.40E+02	6.39E+01
7.45E+02	6.69E+01
7.50E+02	7.02E+01
7.55E+02	7.37E+01
7.60E+02	7.75E+01
7.65E+02	8.17E+01
7.70E+02	8.63E+01
7.75E+02	9.14E+01
7.80E+02	9.70E+01
7.85E+02	10.0E+01